BASE ISOLATION USING STABLE UNBONDED FIBRE REINFORCED ELASTOMERIC ISOLATORS (SU-FREI)

BASE ISOLATION USING STABLE UNBONDED FIBRE REINFORCED ELASTOMERIC ISOLATORS (SU-FREI)

By

Barry A.D. Foster, B.Eng.

A Thesis

Submitted to the School of Graduate Studies

In Partial Fulfillment of Requirements

for the Degree of

Master of Applied Science

McMaster University

Master of Applied Science (2011)
(Civil Engineering)

McMaster University
Hamilton, Ontario

TITLE: BASE ISOLATION USING STABLE UNBONDED FIBRE REINFORCED ELASTOMERIC ISOLATORS (SU-FREI)

AUTHOR: Barry A.D. Foster

SUPERVISOR: Dr. Michael J. Tait

NUMBER OF PAGES: 221 Pages (i-xviii, 1-203)

Abstract

Seismic isolation is a seismic design philosophy that aims to reduce the demand on structures as opposed to increasing their capacity to endure forces. Seismic isolation can be achieved by placing isolating bearings with relatively low stiffness compared to the structure itself beneath the superstructure. This low stiffness layer increases the structural period, shifting the structure into a period range of low seismic energy content.

The objectives of this research were to investigate the dynamic properties, durability and limitations of stable unbonded fibre reinforced elastomeric isolator (SU-FREI) bearings. Vertical compression testing indicated the bearings possessed adequate vertical stiffness. Due to lack of bonding at the bearing interface surfaces rollover deformation was observed to occur during lateral cyclic testing. This response behaviour was found to result in advantageous effective lateral stiffness and damping properties. The bearings maintained stability during rollout testing while serviceability and fatigue testing both conformed to code specified test specimen adequacy limitations. Experimental shake table testing showed that the isolated structure behaved essentially as a rigid body during testing. Test results showed that a SU-FREI isolation system significantly reduced the seismic demand on the structure.

Modelling of the bearings dynamic properties was completed using a bilinear model and a backbone curve model. Both models showed adequate results in predicting experimental peak responses. A simplified design spectrum

analysis was presented and used to model the structure in four Canadian cities. This design spectrum analysis approach showed adequate capabilities in predicting peak response values, such that the method could be used in preliminary analysis and design of isolated structures.

Acknowledgements

First and foremost I would like to express my deepest appreciation and sincere gratitude to my graduate supervisor Dr. Michael Tait for his support, guidance and encouragement throughout this research.

I would like to express a great amount of gratitude to Dr. Hamid Toopchi-Nezhad whose advice and assistance have been invaluable and greatly appreciated.

I would like to thank all of the technical staff working at the Applied Dynamics Laboratory (ADL) and JHE labs for all their advice and assistance during the experimental phases of this research. In particular, Mr. Peter Koudys, Mr. Dave Perrett and Mr. Kent Wheeler.

I would like to thank my friends and colleagues for their support, helpful discussions and encouragement, in particular Mr. Niel Van Engelen and Mr. Shayne Love.

Finally, I would like to thank my closest friends and family for their support, understanding and encouragement throughout the entire duration of my M.A.Sc. study.

Table of Contents

List of Tables

List of Figures

Chapter 1. Introduction

1.1 Introduction

It can be postulated that earthquakes have been occurring on earth since the solidification of its crust, which suggests that strong ground motions have threatened humanity's structures throughout history. To deal with the damaging effects that earthquakes can have on manmade structures, engineers typically design structures using the 'Capacity Design' philosophy. In essence, this design philosophy increases the resistance of a structure by ensuring certain structural components yield before others, through a hierarchy of strengths of materials. The yielded components dissipate energy through hysteresis, allowing the global damage to be minimized. This philosophy assures some level of damage to a structure (Paulay and Priestley 1992). There are two key components to design: the demand that a structure will incur, and a structure's capacity to resist such demand. Rather than attempt to increase capacity, base isolation decreases the demand. With less demand on a structure, the material costs of increasing capacity can be avoided, should an economical form of base isolation be provided.

1.2 Theory of Base Isolation

Base isolation is a design methodology that serves to decouple a structure from the strong ground motions caused by earthquakes. This decoupling of the structure typically occurs at the ground level, between the super-structure and the foundation. Earthquakes, particularly in eastern Canada, have high frequency energy content, which translates to a short period (Gemme 2009). This short period, high-energy correlation can also be seen in the sample earthquake design response spectrum provided in Figure 1.1. When a structure with a short period is driven by a short period excitation, resonance occurs. As many low-rise structures are stiff with short periods, they are particularly vulnerable to short period strong ground motion events associated with earthquakes. The way in which an isolation system works is by lengthening the fundamental period of the structure, which reduces the acceleration response, but increases the displacements as shown in Figure 1.2. As the displacements of the structural system are concentrated in the isolation layer, the isolating bearings must be designed accordingly. Isolation systems need three principal features to be effective. The first is that the system needs to have sufficient lateral flexibility (low lateral stiffness) to lengthen the structure's period to adequately reduce the seismic demand. Secondly, the displacements of the system need to be within a practical limit, which is achieved by energy dissipation in the isolator itself or by supplemental (external) dampers. The last requirement is sufficiently high initial lateral stiffness to assure the

structure is not adversely affected by service loads, such as wind or minor earthquakes (Chen and Scawthorn, 2003).

1.3 History and Application of Base Isolation

Primitive base isolation systems have been around for hundreds of years, utilizing techniques such as rollers and sand or a low friction material to allow the structure to slide in the event of an earthquake (Kelly 1997). One of the first known patent applications for a base isolation system dates back to 1909 by J.A. Calantarients. His method involved the use of a “free joint” and fine sand products to allow the structures to slip under loading; this form of isolation system is referred to as a sliding isolator (Naiem and Kelly 1999). The first case of a structure being isolated using elastomeric bearings was a three-story school built in the former Yugoslavia in 1969. The bearings were solid unreinforced natural rubber blocks (Taylor and Igusa 2004). The lack of reinforcement resulted in vertical stiffness and lateral stiffness of the same order of magnitude, making the structure susceptible to a rocking type response. Present day elastomeric bearings are constructed with some form of reinforcement placed between layers of the elastomer, in order to increase the vertical stiffness. It is only within the last two to three decades that base isolation has become a feasible and practical solution for seismic mitigation through the development of suitable isolation devices, including steel reinforced elastomeric isolator bearings (Naiem and Kelly 1999). Base isolation is now an accepted seismic design solution in many seismically

active areas of the world, including Japan and the United States (Naiem and Kelly 1999). Barriers to the adoption of base isolation in the field of seismic engineering are currently related to material, design, and labour costs primarily due to conservative building code requirements. In the United States, base isolation is acknowledged by buildings codes such as the International Building Code (ICC 2009) and standards such as ASCE 7 (2005). In Canada, the National Building Code of Canada (NBCC) states that design of structures with seismic "isolation is not a standard technique and requires a peer-reviewed special study or investigation tailored to the particularities of each building" (NBCC 2005). Despite these barriers, there are examples of structures that have been retrofitted and designed with base isolation systems, such as a residential house located in Montreal, Quebec (Symans et al. 2002). The cost factor of isolation systems is partially related to the fact that steel is used as the reinforcement in the bearings. The steel makes for a laborious task as it needs to be prepared for vulcanization bonding to the rubber by cutting, sandblasting and cleaning (Kelly and Takhirov 2002). The steel in the isolator also adds substantial weight, which adds to the manufacturing, transportation and installation costs. Despite these costs, designers are seeing the value in the increased level of safety to both occupants and structures, which is why base isolation initiatives including one by Iran's Ministry of Housing and Urban Development, are being implemented. This particular project calls for the base isolation of entire city blocks in the towns of Parand and Hashtgerd near the country's capital of Tehran (Naderzadeh 2009).

The use of different fibre reinforcing materials has been investigated by Kelly (2002), Moon et al. (2002) and Mordini and Strauss (2008) and was found to be a suitable replacement, with carbon fibre showing the most promise. Additional research on the topic has shown that fibre reinforced elastomeric isolator (FREI) bearings can have performance comparable with steel reinforced elastomeric isolator (SREI) bearings (Kelly 1999) and complementary experimental testing has confirmed such theoretical work (Koh and Kelly 1988, Moon et al. 2002, Toopchi-Nezhad et al. 2007b, Toopchi-Nezhad et al. 2008a).

1.4 Base Isolation Systems

Elastomeric, sliding and hybrid systems are the most widely used seismic isolation devices. Elastomeric bearings work by deforming in shear and dissipate energy either through the rubber alone or in conjunction with a lead core. The elastomeric bearing is an attractive device for isolation as the elastomeric material provides a restoring force and leaves no residual displacements of the isolated structure after an earthquake. Sliding isolation systems work by placing a low friction material beneath the superstructure, thus allowing the entire structure to move at the base level as a rigid body under seismic loading. In the past, this had been achieved simply by placing materials such as sand or talc beneath the structure. A hybrid system simply uses both elastomeric and sliding bearings to achieve the desired performance.

1.4.1 Sliding Bearings

Early sliding systems had the undesirable characteristic of permanent displacement of the structure due to the lack of a restoring force needed to re-align the isolation system to its pre-earthquake position. This is a significant problem, particularly for utility connections that enter the structure below ground level. The Friction Pendulum System was developed to overcome this problem. The friction pendulum system has a concave sliding surface, which introduces a gravity related restoring force to re-centreing the bearings.

1.4.1.1 Friction Pendulum System

A friction pendulum system is an attractive form of sliding isolation for several reasons. First, due to the concave geometry of the bearing, the lateral ground motion lifts the structure introducing a restoring force that returns the structure to its original position (Myslimaj et al. 2002). Another advantageous property of a friction pendulum system is that the design is rather simple and analogous to a pendulum in that the period of the isolated structure is dependent only upon the radius of curvature of the bearing. The period of the system can be calculated using Equation 1.1,

$$T = 2\pi\sqrt{\frac{R}{g}} \qquad 1.1$$

where R is the radius of curvature of the bearing and g, the acceleration due to gravity (Symans et al. 2002).

A schematic of a friction pendulum system can be seen in Figure 1.3, where a slider supports the weight of the superstructure resting on the concave surface. Other systems have been designed where both top and bottom plates have curved surfaces (Myslimaj et al. 2002).

The amount of force that can be transferred to the superstructure is related to the stiffness of the friction pendulum system, which is controlled by the curvature and the coefficient of friction, μ, as indicated in Equation 1.2 (Chen and Scawthorn 2003).

$$K_{eff} = \frac{W}{R} + \frac{\mu W}{D} \qquad 1.2$$

W is the vertical load carried by each bearing, R, is the radius of curvature, and D is the design displacement of the system.

The material most often used in such systems is polytetrafluoroethylene (PTFE) or more commonly known as Teflon. The damping in the system is provided from the frictional effects but it should be noted that these effects are dependent on temperature, velocity, cleanliness and wear of the surface (Naiem and Kelly 1999).

1.4.2 Multi-Layer Elastomeric Base Isolator Bearings

The first installation of an elastomeric base isolation system dates back to the aforementioned three-story school located in the former Yugoslavia in 1969 (Taylor and Igusa 2004). The adverse effect of rocking that arose from the use of

unreinforced blocks of rubber were realized by engineers and the elastomeric bearing evolved into a laminated elastomeric bearing with reinforcement being placed between the layers of the elastomer, as shown in Figure 1.4. Typically, the reinforcement material is thin sheets of steel often referred to as shims. Recent research has shown that fibre materials can be used as an alternative reinforcement (Moon et al. 2002).

1.4.2.1 Steel Reinforced Elastomeric Isolator (SREI) Bearings

SREI bearings have been around for several decades and are the most common type of device used for base isolation. The reason for the steel in the elastomer bearing is to provide high stiffness in the vertical direction. This stiffness is required to prevent the bearing from bulging under the pressures induced by the weight of the structure and to decouple the lateral and vertical motions to prevent rocking from occurring (Naiem and Kelly 1999). There are two main types of SREI bearings. The first is layered elastomer and steel, while the second is a lead rubber bearing (LRB). Invented in 1975 in New Zealand, the LRB uses lead core(s) to provide an initial stiffness to satisfy serviceability loads, such as wind, and at design loads the lead core(s) yield(s), providing hysteric damping to the system. A LRB, which can have one or more cores, is shown in Figure 1.5 along with a regular SREI (Naiem and Kelly 1999).

1.4.2.2 Fibre Reinforced Elastomeric Isolators (FREI)

FREI bearings are relatively new to the field of base isolation. They provide isolation using the same principal of having a low lateral stiffness as

SREI bearings; however, the fibres have the advantage of decreased weight and cost, which could potentially broaden the uses of base isolation. Studies have been completed to compare different fibre fabric reinforcement to steel, such as glass fibre (Mordini and Strauss 2008), Kevlar (Kelly and Takhirov 2002) and carbon fibre. In a study by Kelly (1999) a high damping rubber was used to construct a fibre reinforced elastomeric bearing. The rubber had the properties of approximately 8% equivalent viscous damping at 100% shear strain, but when the bearing was tested, the damping at the same shear strain level was approximately 15% implying that the composite structure of the bearing dissipates more energy than the rubber alone. The extra energy dissipation has yet to be fully understood but it has been postulated that it is related to the friction between individual fibres (Kelly 1997). Due to the increased damping provided by the fibre strands, additional means to add damping to the system are not needed, nor are devices such as lead cores required. Kang et al (2003) performed an analytical and experimental study in which a lead core FREI was tested and compared to both a FREI and SREI bearing. Results show that the lead plug has negligible effects on the damping and effective stiffness of the FREI.

1.4.2.2.1 Stable Unbonded Fibre Reinforced Elastomeric Isolator (SU-FREI) Bearings

SU-FREI bearings are FREI bearings that are neither bonded to the super-structure or substructure such as the case for SREI. As a result, they do not require thick steel end plates. Table 1-1 shows examples of different connection types for

bearings. This lack of connection between the bearing and the structure and negligible bending rigidity of the reinforcement means that the deformation characteristics of the bearing differ from those of a steel reinforced bearing. Since the fibres have no flexural rigidity, the bearing exhibits unique rollover deformation behaviour as shown in Figure 1.6. As a result, the design process for this type of fibre bearing is more complicated. However, a positive feature of this rollover deformation is that the stiffness of the isolator decreases until the originally vertical faces, perpendicular to the excitation, contact the upper and lower surfaces, thus increasing the lateral stiffness (Toopchi-Nezhad et al. 2008b). This behaviour is shown in Figure 1.7 and is beneficial as the lowered stiffness increases the efficiency of the system while the stiffening acts to limit maximum lateral displacements of the isolators.

1.5 Properties of SU-FREI Bearings

Key concepts, properties and previous experimental testing of SU-FREI bearings are described in this section.

1.5.1 Scragging

Scragging is a phenomenon that occurs in elastomeric materials, which is described as softening or a decrease in the stiffness of an elastomer from its virgin state due to cyclic loading. It should be noted that a portion of the stiffness is recovered over time. The effects of the reduction in stiffness are greatest in the first cycle and become negligible after two to three cycles as can be seen in Figure

1.8 (Dorfmann and Ogden 2004). The term is also known as the Mullins Effect and the mirco-mechanical structural behaviour that is responsible for the loss of stiffness is the breaking of weak crosslinks that are found in elastomers (Dorfmann and Ogden 2004). It is important to note that the material is only scragged up to the largest amplitude to which it has been subjected. If a specimen is tested at a larger amplitude the specimen would exhibit scragging effects at this amplitude, as shown in Figure 1.8. Scragging was observed in SU-FREI bearings by (Toopchi-Nezhad 2008) with the effects becoming negligible after the first cycle.

1.5.2 Serviceability

Base isolation systems must not only mitigate the effects of strong ground motions but must also perform adequately under service loads to prevent discomfort to occupants. Having a flexible layer at the base of the structure can significantly increase wind induced motions. As a result, isolation systems must have a sufficient level of initial stiffness. With the addition of a lead core and with advances in rubber compounds, adequate levels of initial stiffness can be achieved. However, in the past, such as in the first use of elastomeric bearings, glass restraints were used as “fuses” to provide high stiffness until they broke and the stiffness of the system was then solely attributed to the bearings (Kelly 1997). Research carried out by de Raaf (2009) has shown that SU-FREI’s can satisfy serviceability related code provisions (ASCE 2005).

1.5.3 Fatigue

Fatigue testing was completed by de Raaf (2009) on SU-FREI bearings in accordance with testing protocols specified in ASCE 7 (2005). The procedural basis for testing was to subject the bearings to a constant design vertical pressure and laterally cycle at the total design lateral displacement D_{TD}. The total design displacement is based on the isolated structure; therefore, a model structure was assumed in order to calculate the design total displacement. The total design displacement calculated by de Raaf (2009) was 102mm (full scale) or $1.33t_r$, which was increased to $1.5t_r$ and the number of cycles required was calculated to be 12. A total of four bearing specimens were tested. ASCE 7 (2005) requires that the bearings maintain positive incremental force resisting capacity throughout each cycle, and both effective stiffness and effective damping remain within 20% of the initial cycle. All bearings showed positive incremental force resisting capacity and the average reduction of stiffness between the first and twelfth cycles was 18%, satisfying code requirements. The largest portion of the reduction of lateral stiffness occurred during the first 2-3 cycles. For effective damping, there was an average decrease of 30% within the first cycle alone, but when considering only scragged values, the damping remained within 3% of the mean. The bearings showed acceptable behaviour during fatigue testing under scragged conditions at the displacement amplitude of $1.5t_r$.

1.5.4 Stability

Stability of SU-FREI bearings was investigated by Toopchi-Nezhad (2008) as well as de Raaf (2009). Toopchi-Nezhad showed that stable rollover deformation can be advantageous to the bearing and that stable rollover is affected largely by the geometry of the bearing, while de Raaf studied the two stability concerns of rollout and dynamic buckling.

1.5.4.1 Stable Rollover Behaviour

As lateral load is applied to a SU-FREI bearing, the bearing begins to roll over. This deformation occurs due to the unbonded boundary conditions and lack of flexural rigidity of the fibre fabric reinforcement. As the bearing begins to roll over, the lateral stiffness decreases resulting in an increased period, making the bearing more efficient at mitigating the seismic response of a structure. The reduction in stiffness is considered acceptable as long as the tangential lateral stiffness remains positive. In the case of large lateral displacements of the SU-FREI bearing, the originally vertical surfaces make contact with the upper and lower supports. As contact is made, a hardening (stiffening) effect is observed. The hardening effect acts to limit extreme displacements of the bearing as well as ensure stability (Toopchi-Nezhad 2008).

1.5.4.2 Influence of Geometry on Stable Rollover

Toopchi-Nezhad (2008) found that stable rollover was affected by the geometry of a bearing, particularly the shape factor, S, (defined as the ratio of

loaded area to load-free area of an elastomer layer) and aspect ratio, R (defined as the ratio of bearing width to total height). Two bearings with shape factors of 10.6 and aspect ratios of 1.9 were laterally cyclically tested (B1 and B2). The two bearings were deemed unacceptable as both experienced negative lateral tangential stiffness resulting in instability. Due to the results of the tests, two new bearings were constructed from the existing bearings to create NB1 and NB2, respectively with increased aspect ratios of 2.5 and 2.9, respectively. Lateral cyclic testing of the two new bearings showed stable rollover was achieved for both bearings in both a parallel (90°) and diagonal (45°) orientation. In conclusion, it was found that the aspect ratio of the bearings plays a large role in stability.

1.5.4.3 Rollout

The rollout testing performed by de Raaf (2009) consisted of subjecting a SU-FREI bearing to its design pressure of 1.6MPa, while displacing the bearing laterally at a constant rate until the bearing delaminated or buckled, where buckling is defined as the state at which a elastomer isolator loses its stability (positive load carrying capacity) under compressive shear testing as defined by ISO standards (ISO 2005). The objective of the test was to determine δ_{max}, the displacement value at which the bearing could reach before instability occurred under design vertical load. Due to the unbonded contact surfaces of the bearing and lack of flexural rigidity the isolators exhibited rollover behaviour. Rollover should not be confused with rollout, as all properly designed SU-FREI bearings

undergo stable rollover (Toopchi-Nezhad et al. 2008a). de Raaf tested two bearing specimens for rollout instability. The first bearing was subjected to a lateral displacement of 2.75t_r (≈52mm) and the second to 3.00t_r (≈57mm). Figure 1.9 shows the lateral tangential stiffness versus displacement. Rollout instability was not observed to occur during either test (de Raaf 2009).

1.5.4.4 Dynamic Buckling

Dynamic buckling is the loss of positive incremental load resisting capacity during lateral cyclic testing. de Raaf (2009) investigated the dynamic buckling capacity of SU-FREI bearings. A total of five SU-FREI bearings were tested, undergoing two complete sinusoidal lateral cycles at the selected lateral excitation amplitude, while under constant vertical load. After each test, the bearings were removed from the test setup and inspected for damage (particularly delamination between layers). The tests continued on the bearing with increasing vertical (axial) load until instability occurred at a particular lateral amplitude. Once this was achieved, the bearing was put back under the lower axial load; the excitation amplitude increased and the test procedure repeated. This process was repeated for four amplitudes (0.5tr, 1.0tr, 1.5tr, and 2.0tr). Test results provided insight into the critical buckling load, P_{cr}, of the bearing at different displacement amplitudes and showed the effects of vertical load on the dynamic properties. Three of the five bearings experienced delamination during the testing process but maintained stability, however, a decrease in lateral stiffness was observed. It was concluded that the bearings investigated were not susceptible to buckling under

dynamic excitation, as the critical buckling load, P_{cr}, at the design basis earthquake (DBE) and maximum considered earthquake (MCE) displacements were 10.6 and 8.2 times greater, respectively, than the specified vertical design loading.

1.5.4.4.1 Effects of Axial Loads on Dynamic Properties

de Raaf (2009) investigated the effect of axial load on the dynamic properties of SU-FREI bearings, the two most important properties being the effective lateral stiffness and damping. Results confirmed observations by others for bonded bearings (Kelly and Takhirov 2002, Tsai and Kelly 2004), that with higher vertical pressure the lateral stiffness of the bearing decreases and the damping increases.

1.6 Research Objectives

The main objectives of this research study are as follows:

- Construct and experimentally test quarter-scale SU-FREI bearings under dynamic loading to determine bearing properties including vertical stiffness, effective lateral stiffness, effective damping, stability, and durability at low and high amplitude displacements.
- Select and calibrate two analytical models based on experimental hysteresis data that can adequately simulate the dynamics response of the bearing.

- Conduct shake table experiments on a quarter-scale structure isolated with SU-FREI bearings to investigate the feasibility of the bearings as a base isolation system.
- Evaluate the performance of the two selected bearing models by comparing results from shake table tests to response predictions of the modeled isolated structure obtained by time history analysis
- Perform a case study using design spectrum analysis of the base isolated and fixed based structure situated in four Canadian cities. The results of the spectrum analysis are also compared with results of a time history analysis.

1.7 Structure of Thesis

The structure of this thesis study is organized into eight chapters.

Chapter 1 is a literature review and provides background information on the base isolation with particular focus on stable unbounded fibre reinforced elastomeric isolator bearings.

Chapter 2 describes the bearing testing program including the construction process, the objectives of the tests, and the testing equipment and procedures used in this study.

Chapter 3 investigates the dynamic properties of the SU-FREI bearings. This includes effective stiffness, damping and stability, which were obtained from

various tests, including vertical compression testing, lateral cyclic testing, rollout, serviceability and fatigue.

Chapter 4 presents two methods to model the lateral dynamic properties of SU-FREI bearings based on experimental results. The models are subsequently used to simulate hysteresis loops for evaluation purposes. The models selected are a bilinear model as well as a backbone curve model based on a 5th order polynomial.

Chapter 5 explores the performance of a quarter-scale SU-FREI base isolated structure subjected to unidirectional excitation. Three earthquakes scaled to five amplitudes of peak ground acceleration, were employed in order to cover a large spectrum of possible earthquake scenarios. The results are subsequently compared to results from time history analysis of the fixed base structure.

Chapter 6 provides a time history analysis of the base isolated structure using the models introduced in Chapter 4. The base isolated structure is analyzed using the response acceleration recorded during the shake table testing in Chapter 5 permitting a direct comparison between results of the analysis and experiment for further validation of the models to be made.

Chapter 7 presents a simplified design spectrum approach to predict the response of the base isolated structure. A limited case study is presented highlighting the methods' ability to predict the response of the isolated structure situated in Vancouver, Victoria, Montreal and Ottawa, subjected to maximum and design level earthquakes. The results are compared to the predicted fixed base

structural response. In addition, time history analysis using design spectrum matched earthquake records are also computed and compared to base isolated design spectrum response values.

Chapter 8 provides a summary of the work as well as offering recommendations for future research on SU-FREI bearings.

Table 1-1 Classification of base isolation connection type (ISO 2005).

Type I	Isolator is bonded to connecting flanges which are in turn bolted to the mounting flanges	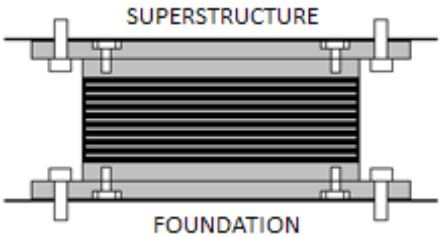
Type II	Isolator is bonded directly to the mounting flanges	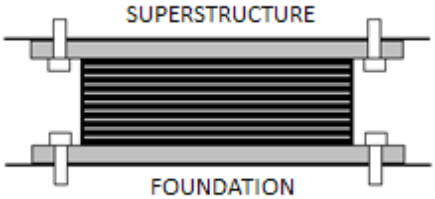
Type III	Isolator connected to the base with recessed rings	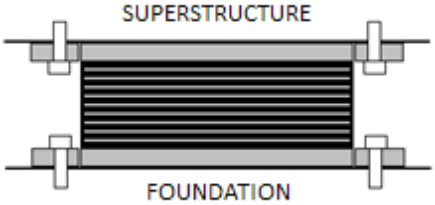
	Isolator connected to the base with dowelled pins	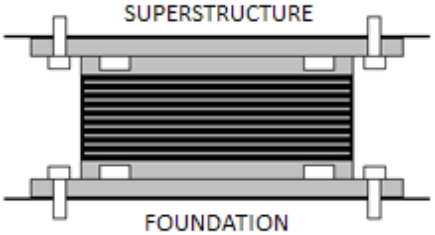
Type SU	Isolator is placed directly between superstructure and foundation with no bonding	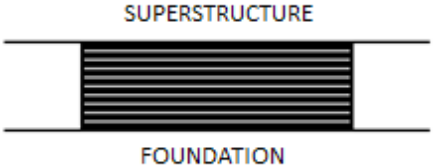

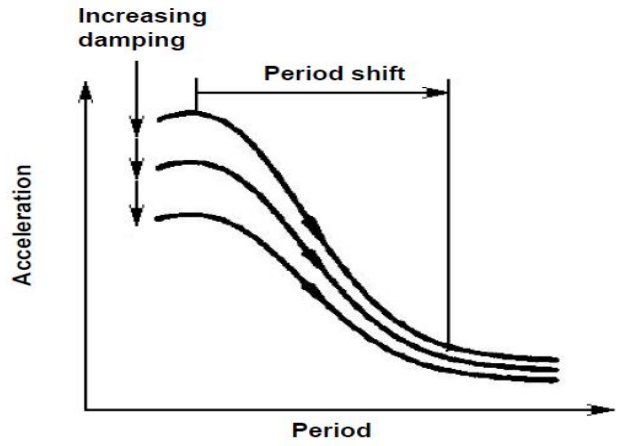

Figure 1.1 Example acceleration response spectrum (Skinner et al. 1993).

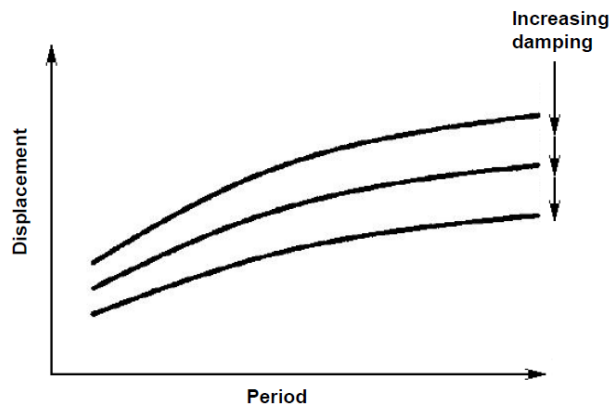

Figure 1.2 Example displacement response spectrum (Skinner et al. 1993)

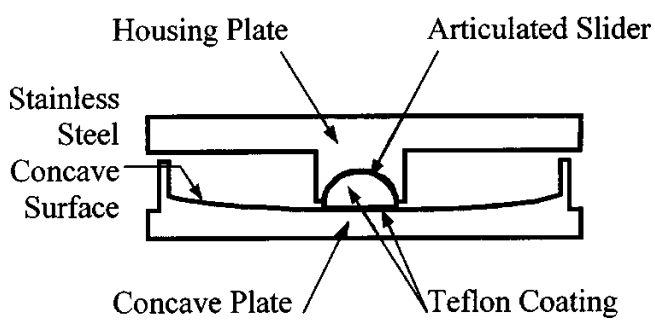

Figure 1.3 Schematic of a friction pendulum bearing (Symans et al. 2002).

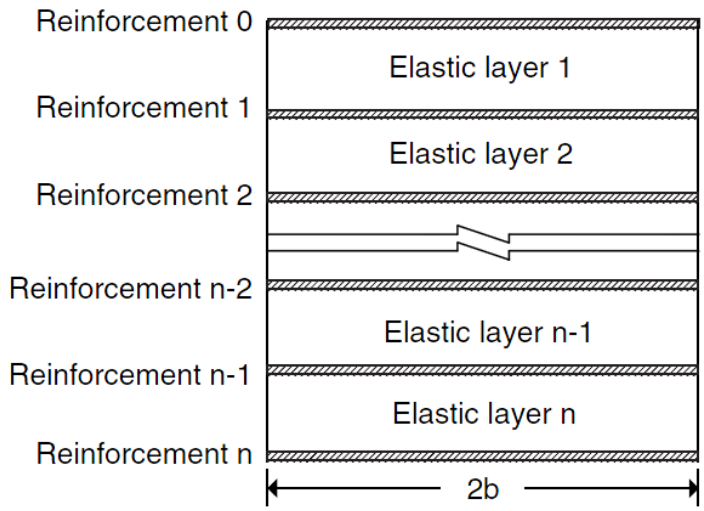

Figure 1.4 Cross section of an elastomeric bearing (Tsai 2004).

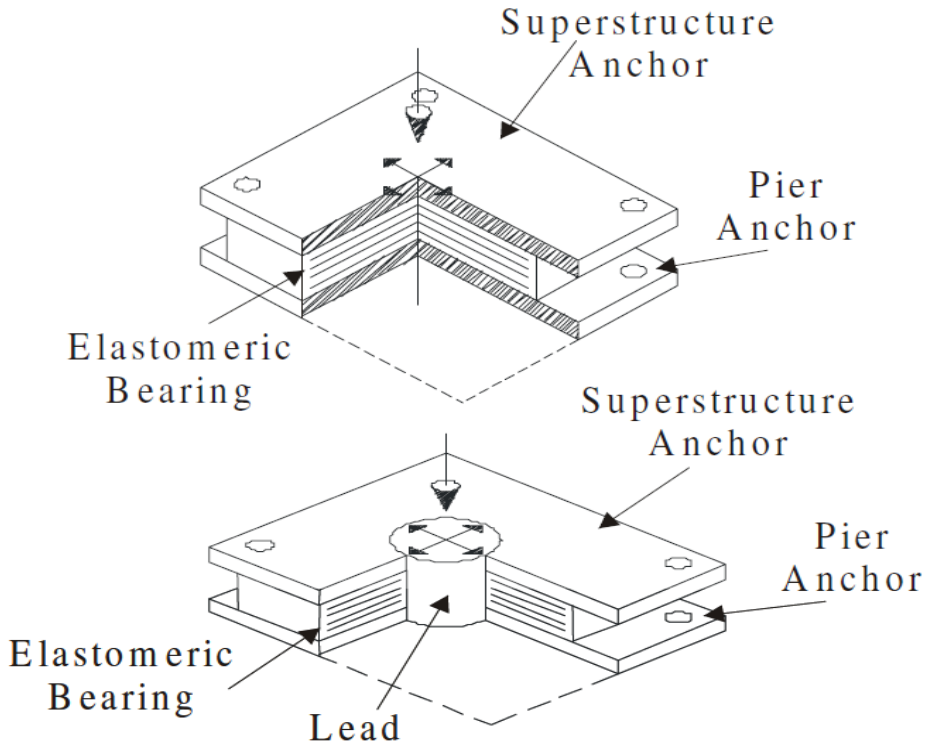

Figure 1.5 (Top) A typical SREI, (Bottom) a LRB (Mayes and Naeim 2001)

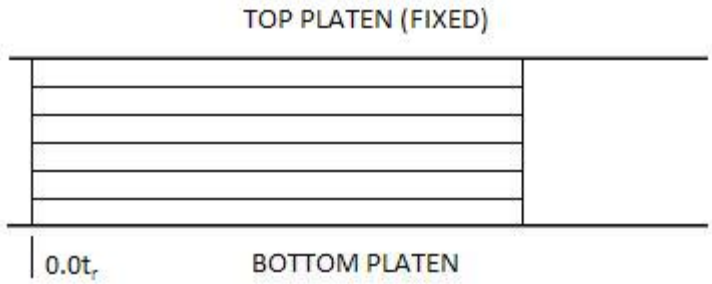

(a) $0.0t_r$

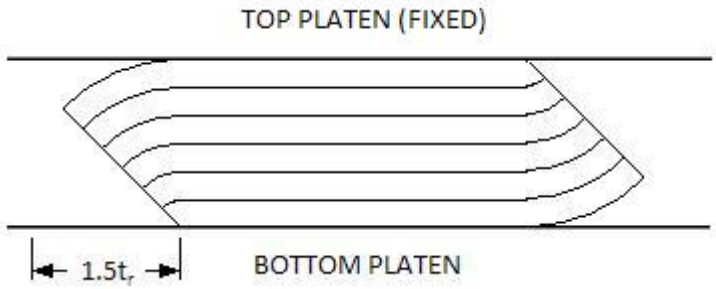

(b) $1.5t_r$

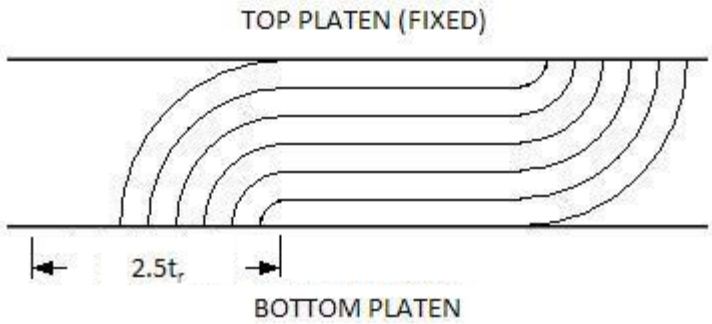

(c) $2.5t_r$

Figure 1.6 Rollover deformation of a SU-FREI at three stages (de Raaf 2009).

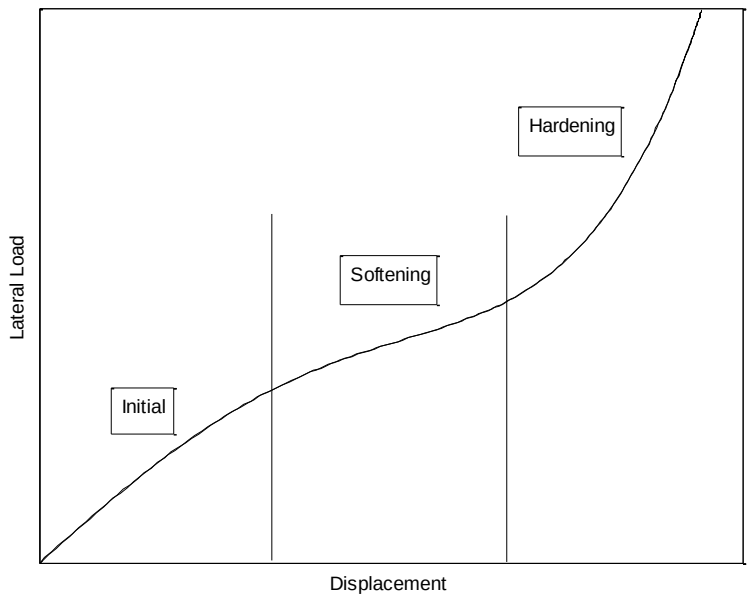

Figure 1.7 Graphical depiction displaying the softening and hardening trends due to rollover deformation of the SU-FREI bearing.

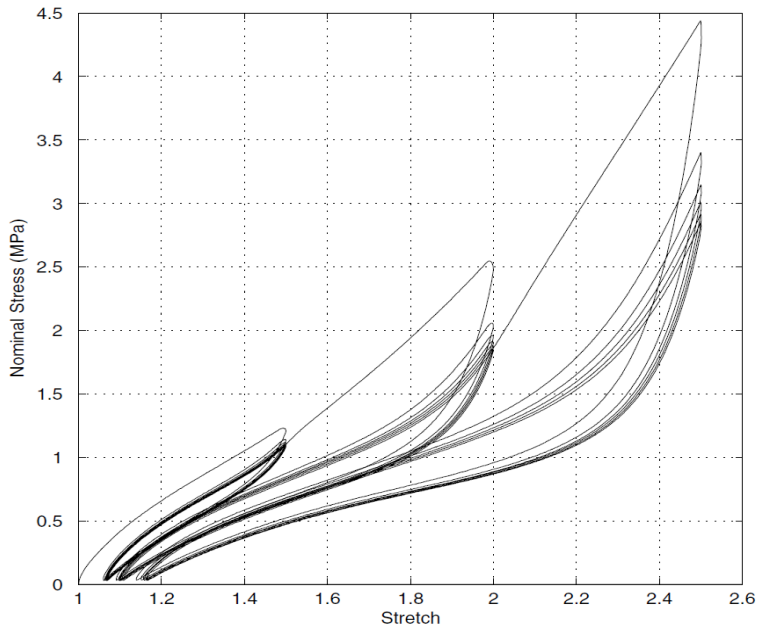

Figure 1.8 Example of loss of stiffness due to scragging of rubber during cyclic testing (Dorfmann and Ogden 2004).

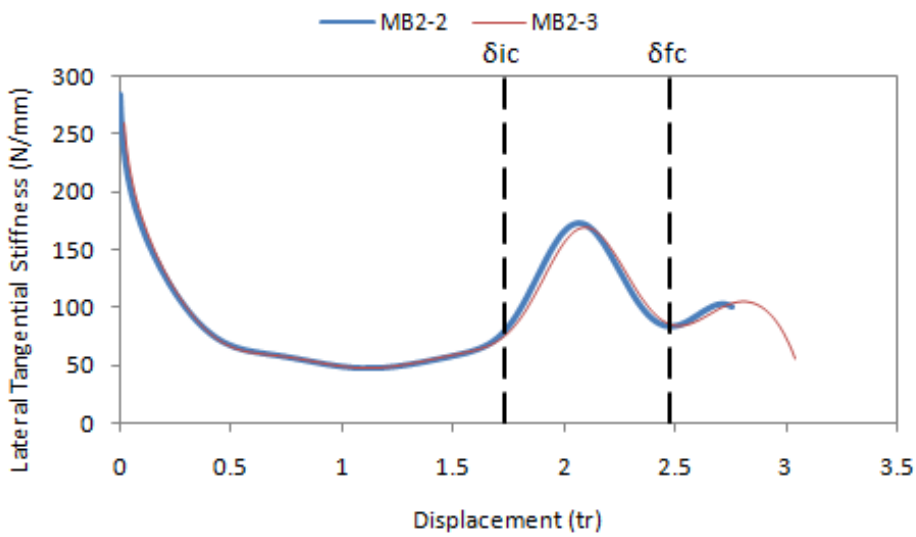

Figure 1.9 Lateral tangential stiffness versus displacement from rollout testing (de Raaf 2009).

Chapter 2. Fibre Reinforced Elastomeric Bearing Test Program

2.1 Introduction

This chapter describes the bearing test specimens and the test apparatus used to conduct the individual bearing tests to determine their properties and behaviour. In addition, a detailed description of the testing protocols and procedures used in this study to test the bearing specimens is provided.

2.2 Description of Test Specimen

The bearings tested in this study comprised of a total of thirteen layers of elastomer and fibre as shown in Figure 2.1. Seven of the thirteen layers were elastomer, the five interior elastomer layers were a thickness of 3.175mm and the two outer elastomer layers (located at the top and bottom of the bearing) were 1.5875mm thick. The elastomer material was a neoprene rubber having a manufacturer specified nominal tensile modulus of 1.0MPa at 100% elongation, a specified shear modulus of $G = 0.35$MPa and a specified damping ratio of approximately 5%. The remaining six layers were a bi-directional, plain weave carbon fibre fabric with a thickness of 0.55mm. The carbon fibre fabric was bonded to the elastomer using a rubber cement product.

A total of five thirteen layered sheets with a total height of 22.35mm were constructed. The specimens were subsequently cut to the final plan dimensions of

63mm x 63mm, before two coatings of rubber cement were applied to the edges of the bearings. The end of a bearing before and after the application of the rubber cement coatings is shown in Figure 2.2. A total of twenty-two bearing specimens were constructed in this study. The bearings were labeled with the prefix B1-B5 followed by a matrix notation to denote the row and column of the sheet. A photograph of sheet B1, indicating the bearing specimens, is shown in Figure 2.3.

2.3 Bearing Test Setup and Instrumentation

A schematic of the bearing testing apparatus, shown in Figure 2.4, was a modified version of the setup used by Toopchi-Nezhad (2008) and de Raaf (2009). Two modifications to the setup were completed, which included replacing the vertical actuator and a re-configuration of the vertical load cells for improved vertical load control capabilities. A photograph of the modified setup is shown in Figure 2.5.

The setup consists of two 100mm think steel plates. The lateral actuator displaces the bottom plate, which is mounted on four linear bearings, relative to the top plate and has a maximum displacement range of ± 150mm. The lateral actuator can be operated under either displacement or load control. While under displacement control, a feedback signal is provided by the linear variable displacement transducer (LVDT #1). A string potentiometer placed at the same location measures the relative displacement for acquisition purposes. Three vertical load cells, used to measure the vertical load, are utilized for both

acquisition and control purposes. A load cell was used to measure the lateral force induced on the bearing during cyclic testing, which was located just above the sample specimen as shown in Figure 2.4. Vertical displacements were measured using four laser displacement transducers (LDT) located at the edges of the upper and lower plates.

2.4 Testing Procedures

2.4.1 Vertical Compression Testing

The vertical test protocol corresponds to Method 2 of the loading procedures for vertical testing of bearings as specified in the ISO 22762-1 standard (ISO 2005). The vertical compression testing procedure commenced by monotonically loading the bearing up to a predetermined vertical load. Once the vertical load was attained, it was sustained for five seconds before being sinusoidally cycled ±20% of the applied vertical load value. The loading histories are shown in Figure 2.6 for four vertical loads, corresponding to 0.5, 1, 1.5 and 2 times the design load (pressure) of 8kN (2MPa). The objective of vertical testing was to determine the vertical stiffness to ensure that it was sufficiently larger than the lateral stiffness to prevent rocking. Testing at vertical loads above and below the vertical design load of 8kN was carried out to investigate the influence of vertical load (pressure) on bearing behaviour.

In addition, after lateral testing was completed, selected bearings were retested vertically at the design load of 8kN to determine if substantial change in the vertical stiffness occurred.

2.4.2 Lateral Cyclic Testing

The lateral loading history used for the lateral cyclic testing can be seen in Figure 2.7. The bearings were monotonically vertically loaded to the design load of the bearing (see Figure 2.7a). After five seconds of sustained vertical load the lateral actuator cycled the bearing at three fully reversed sinusoidal cycles of seven different constant amplitude displacements, 25%, 50%, 75%, 100%, 150%, 200% and 250%t_r with t_r being the total thickness of the rubber layers in the bearing (19.05mm), see Figure 2.7b. The velocity amplitude was 76.2mm/s, which corresponds to a frequency of 1Hz at 100%t_r. The resulting hysteresis data obtained from the tests allowed the dynamic properties of the bearings to be evaluated. These properties were subsequently used in two numerical models to simulate the hysteresis behaviour. Further testing of the bearings at vertical loads of 2, 4 and 12kN was completed to observe the effect of vertical load on the bearing properties. These bearings were only cycled up to 200%t_r at a rate of 76.2mm/s.

2.4.3 Rollout Testing

Rollout, not to be confused with rollover, is the instability of recessed or dowelled bearings under shear displacement (ISO 2005). For the case of fibre

reinforced bearings, rollout testing was done to determine displacements at which delamination would occur between the fibre and rubber layers as well as instability determined by the lateral tangential stiffness of the bearings. Rollout testing in this study followed the procedure described by de Raaf (2009). The loading sequence used for Rollout testing is shown in Figure 2.8. The vertical load was monotonically increased to the design load (8kN) and then held constant (see Figure 2.8a). Five seconds of constant vertical load was sustained before the lateral actuator was displaced at a constant rate of 76.2mm/s to the maximum displacement. The lateral actuator then immediately return to a zero displacement in the same manner, representing a single saw tooth line (see Figure 2.8b).

2.4.4 Serviceability Testing

Serviceability testing was carried out to ensure that the dynamic properties of the bearings remained stable after repeated cyclic loading and that a significant reduction in stiffness and damping did not occur. The testing method used wind loads calculated using the National Building Code of Canada (NBCC) (2005). Testing was carried out under load control and the bearings were cycled at the natural frequency corresponding to the displacement amplitude of the bearings. The bearings were monotonically vertically loaded to the 8kN design load and twenty fully reversed cycles of sinusoidal lateral loading were applied as specified in ASCE 7 (2005).

The wind forces were calculated based on the dynamic loading procedure given in the NBCC (2005). The base isolated structure used to calculate wind

forces was a modified version of the structure used by Toopchi-Nezhad et al. (2009a), which is discussed in further detail in Chapter 5. It was assumed that the structure was located in Montreal. The full-scale structure corresponded to a 5.6m by 6m plan dimension with a height of 6.716m and a total weight of 513.6kN. The design wind pressure, p_e, is given by Equation 2.1 taken from NBCC (2005),

$$p_e = I_w q C_e C_g C_p \qquad 2.1$$

where, I_w represents the importance factor (taken as 1), q represents the wind velocity pressure which is taken from code tables depending on the return period. C_e is an exposure factor (taken as 1) and C_p is the pressure coefficient (taken as 1.2). C_g, the final variable, is the gust factor and is determined through iteration as it is a function of the frequency of the isolated structure, which can be calculated using Equation 2.2,

$$f_n = \frac{1}{2\pi}\sqrt{\frac{K_{eff}}{M_T}} \qquad 2.2$$

where M_T is the total mass of the structure and K_{eff} is the effective lateral stiffness as defined by Equation 2.3.

$$K_{eff} = \frac{F_W}{\Delta_{max}} \qquad 2.3$$

Δ_{max} is the maximum displacement of the isolation system and F_W is defined by Equation 2.4, the force on the structure,

$$F_w = p_e bh \qquad 2.4$$

where b and h are, respectively, the longest plan dimension of the structure and the height, p_e is the wind pressure as calculated with Equation 2.1.

The three wind forces (service, design and maximum) calculated for an individual bearing at quarter scale were respectively 569N, 748N and 1169N with corresponding natural frequencies of 1.4Hz, 1.3Hz and 1.1Hz.

2.4.5 Fatigue Testing

Fatigue testing, as outlined by the ASCE 7 (2005), requires the testing of a bearing at its total design displacement, D_{TD}, for a high number of cycles to ensure that adequate bearing performance is maintained. D_{TD} is calculated using Equation 2.5.

$$D_{TD} = D_D[1 + y\left(\frac{12e}{b^2 + d^2}\right)] \qquad 2.5$$

Equation 2.5 variables are defined as: b, the shortest plan dimension, d, the longest plan dimension, e, the eccentricity of the centre of mass with respect to the isolation systems centre of rigidity and y is the distance between the centre of rigidity of the isolation system and the element of interest, measured perpendicular to the direction of seismic loading. D_D, is given by (Equation 2.6),

$$D_D = \frac{gS_{D1}T_D}{4\pi^2 B_D} \qquad 2.6$$

where variables are: S_{D1}, the 5% damped spectral acceleration at a period of one second, T_D, the effective design period of the structure and B_D, a coefficient for effective damping defined in ASCE 7 (2005).

To study the bearings at a displacement amplitude higher than serviceability levels, an amplitude of 150%t_r was chosen as D_{TD}. 150%t_r was also selected as it represents the displacement amplitude that is expected to correspond to minimal lateral stiffness, making it the desired target displacement of the system for optimal seismic mitigation efficiency. The bearings were loaded vertically to 8kN before undergoing ten sinusoidal cycles under displacement control.

2.5 Testing Sequence

A total of three bearings were used for vertical testing, as shown in Table 2-1. The bearings were B1-11, B1-13 and B1-23. Each bearing underwent the vertical testing procedure described in Section 2.4.1.

Lateral cyclically tested bearings were B1-11, B1-13, B1-23 and B3-12 as shown in Table 2-2. The bearings were subjected to an initial vertical compression test to determine their initial vertical stiffness before undergoing lateral cyclic testing. After lateral cyclic testing, a second round of vertical compression testing was completed on the bearing to quantify the vertical stiffness.

Further lateral cyclic testing was completed on bearings B3-12, B4-21 and B4-11 under various design vertical loads for the purpose of studying the effect of vertical load on the effective lateral stiffness and damping. The testing matrix of these bearings is shown in Table 2-3.

The testing matrix for the rollout experiments is shown in Table 2-4 consisting of bearings B1-11, B1-13 and B1-23. Bearing B1-11 was the first bearing tested under displacement amplitudes of 300, 350 and 400%t_r, while bearings B1-13 and B1-23 were subjected to 400%t_r displacement amplitudes.

Serviceability testing under the equivalent wind loading was completed on bearing B2-11. Fatigue testing was conducted bearing B2-21 and B4-21. The serviceability and fatigue testing matrices are shown in Table 2-5 and Table 2-6, respectively.

The remaining bearings were used in the experimental shake table tests for system performance and validation of bearing models. The testing matrix of the bearings is shown in Table 2-7.

Table 2-1 Bearing specimens subjected to full vertical testing procedure.

B1-11	B1-13	B1-23
Vertical Test p=4,8,12,16kN	Vertical Test p=4,8,12,16kN	Vertical Test p=4,8,12,16kN

Table 2-2 Bearing specimens subjected to 250%t_r lateral cyclic testing and vertical retesting.

B1-11	B1-13	B1-23	B3-21
Vertical Test p=4,8,12,16kN	Vertical Test p=4,8,12,16kN	Vertical Test p=4,8,12,16kN	Vertical Test p=8kN
Cyclic Test (0°) rate=76.2mm/s, p=8kN	Cyclic Test (0°) rate=76.2mm/s, p=8kN	Cyclic Test (0°) rate=76.2mm/s, p=8kN	Cyclic Test(0°) rate=76.2mm/s, p=8kN
Vertical Test p=8kN	Vertical Test p=8kN	Vertical Test p=8kN	Vertical Test p=8kN

Table 2-3 Bearing specimens subjected to lateral cyclic testing under different vertical loads.

B3-12	B4-21	B4-11
Vertical Test p=2kN	Vertical Test p=4kN	Vertical Test p=8kN
Cyclic Test(0°) rate=76.2mm/s, p=2kN	Cyclic Test(0°) rate=76.2mm/s, p=4kN	Cyclic Test(0°) rate=76.2mm/s, p=8kN
Vertical Test p=2kN	Vertical Test p=4kN	Vertical Test p=8kN
Vertical Test p=8kN	Vertical Test p=8kN	Vertical Test p=12kN
Cyclic Test(90°) rate=76.2mm/s, p=8kN	Cyclic Test(90°) rate=76.2mm/s, p=8kN	Cyclic Test(90°) rate=76.2mm/s, p=12kN
Vertical Test p=8kN	Vertical Test p=8kN	Vertical Test p=12kN

Table 2-4 Bearing specimens subjected to rollout testing.

B1-11	B1-13	B1-23
Rollout Test(90°) 300%t_r amplitude	Rollout Test(90°) 400%t_r amplitude	Rollout Test(90°) 400%t_r amplitude
Rollout Test(90°) 350%t_r amplitude		
Rollout Test(90°) 400%t_r amplitude		

Table 2-5 Bearing specimen subjected to serviceability testing.

B2-11
Serviceability Test(90°) q=0.31,0.4,0.6 rate= natural frequency

Table 2-6 Bearing specimens subjected to fatigue testing.

B2-21	B4-12
Fatigue test(0°) 150%t_r Rate = natural frequency	Fatigue test(90°) 150%t_r Rate = natural frequency

Table 2-7 Bearing specimens subjected to shake table testing.

B1-33	B2-12	B4-22	B5
Shake Table Test El Centro 0.1g - 0.5g	Shake Table Test El Centro 0.1g - 0.5g	Shake Table Test El Centro 0.1g - 0.5g	Shake Table Test El Centro 0.1g - 0.5g

B1-12	B1-21	B1-32	B2-22
Shake Table Test Loma Prieta 0.1g - 0.5g (90°)	Shake Table Test Loma Prieta 0.1g (90°)	Shake Table Test Loma Prieta 0.1g - 0.5g (90°)	Shake Table Test Loma Prieta 0.1g - 0.5g (90°)
Shake Table Test w/ Friction Loma Prieta 0.1g - 0.5g (0°)	Shake Table Test w/ Friction Loma Prieta 0.1g - 0.5g (0°)	Shake Table Test w/ Friction Loma Prieta 0.1g - 0.5g (0°)	Shake Table Test w/ Friction Loma Prieta 0.1g - 0.5g (0°)
Shake Table Test w/ Friction Loma Prieta 0.1g - 0.5g (45°)	Shake Table Test w/ Friction Loma Prieta 0.1g - 0.5g (45°)	Shake Table Test w/ Friction Loma Prieta 0.1g - 0.5g (45°)	Shake Table Test w/ Friction Loma Prieta 0.1g - 0.5g (45°)

B1-22	B1-31	B3-11	B3-22
Shake Table Test Chile 0.1g - 0.5g	Shake Table Test Chile 0.1g - 0.5g	Shake Table Test Chile 0.1g - 0.5g	Shake Table Test Chile 0.1g - 0.5g

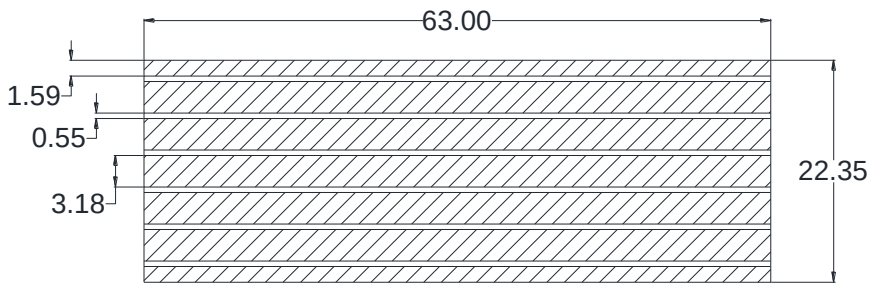

Figure 2.1 Schematic of the SU-FREI composition with theoretical dimensions in millimeters.

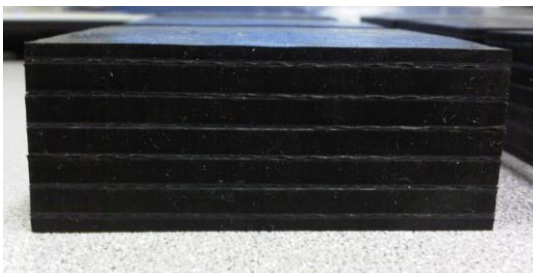

a) Uncoated bearing specimen.

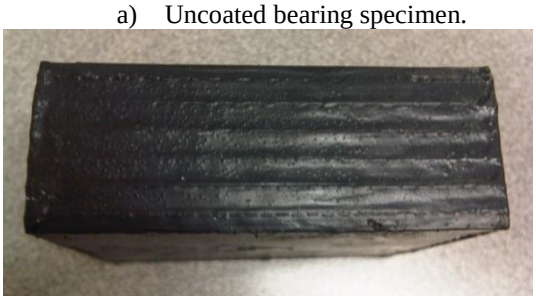

b) Coated bearing specimen.

Figure 2.2 Elevation view of an (a) uncoated (b) coated bearing.

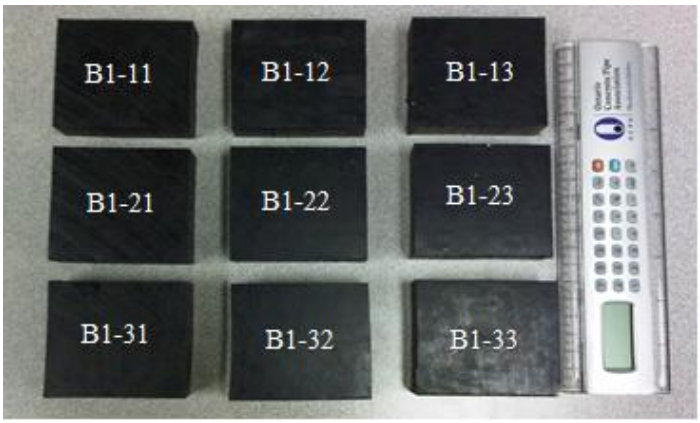

Figure 2.3 Photograph displaying the layout of the cut bearing specimens taken from sheet.

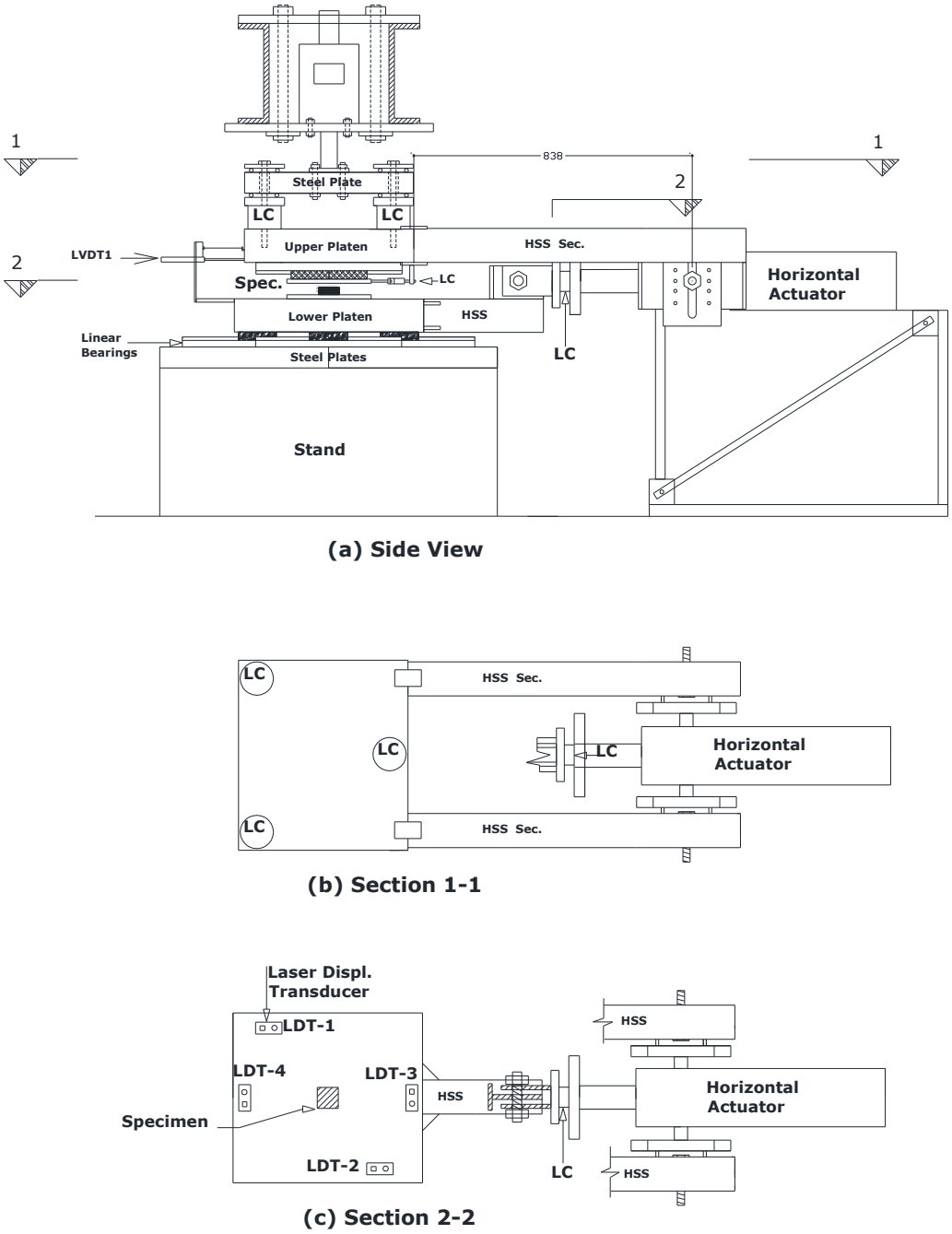

Figure 2.4 Schematic of the bearing testing apparatus with two cross section views.

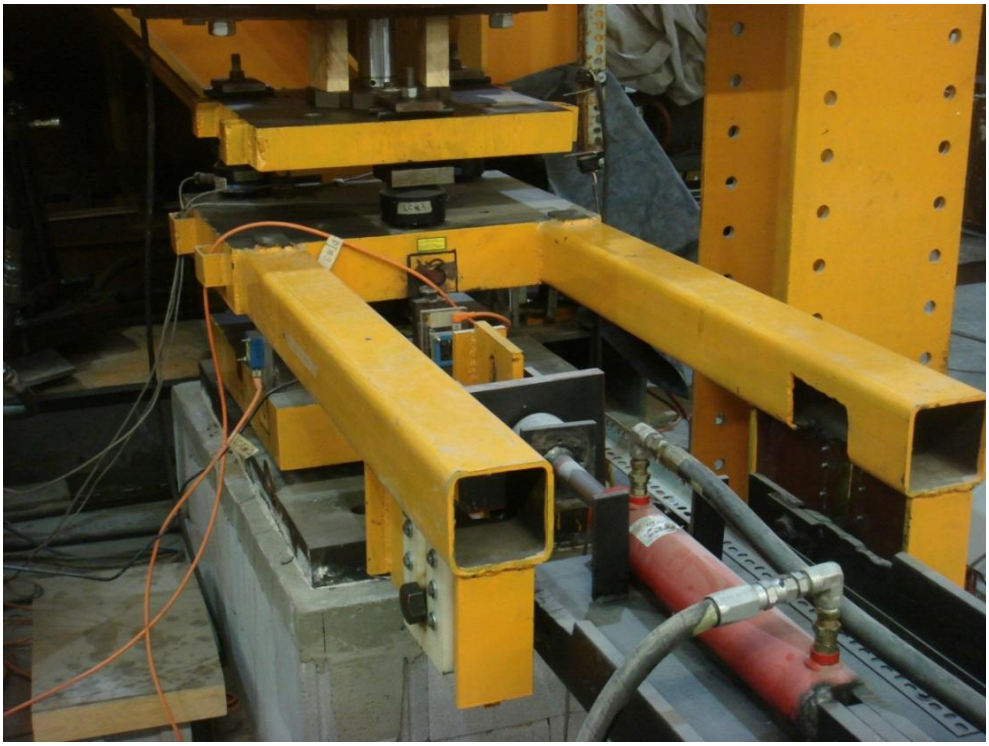

Figure 2.5 Test setup used for cyclic testing of bearing specimens.

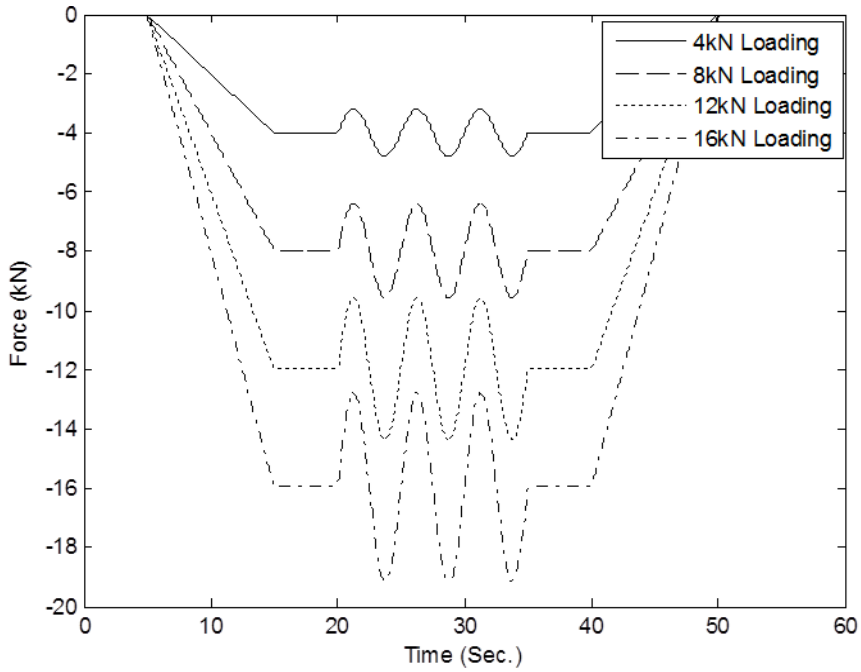

Figure 2.6 Vertical loading histories used for compression testing.

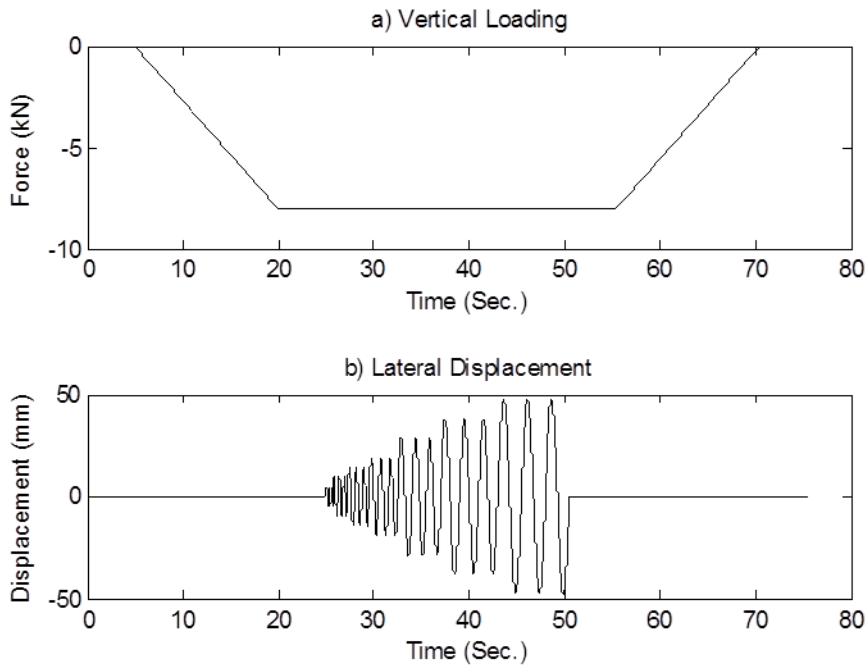

Figure 2.7 a) Vertical loading, b) lateral displacement applied during lateral cyclic testing.

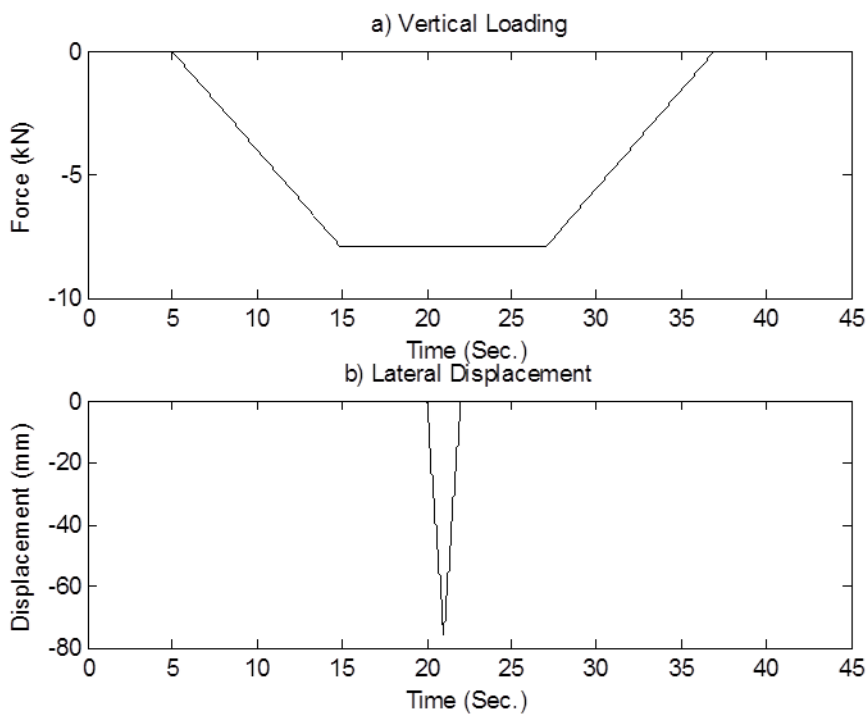

Figure 2.8 a) Vertical loading, b) lateral displacement applied during rollout testing.

Chapter 3. Stable Unbonded Fibre Reinforced Elastomeric Isolator (SU-FREI) Test Results

3.1 Introduction

Experimental testing procedures used to study the behaviour and evaluate the performance of elastomeric bearings were described in Chapter 2. The results of the tests are presented in this chapter and are used to determine the bearings effective vertical and lateral stiffness and damping properties as well as evaluate their behaviour at serviceability and ultimate lateral displacement amplitudes.

3.2 Vertical Compression Testing

Vertical compression tests were completed to determine the vertical stiffness and frequency of the bearings. These properties are important, as they need to be sufficiently greater than the effective lateral stiffness and frequency to avoid rocking motion.

Three bearings (B1-11, B1-23 and B1-13) were selected for vertical testing, which was carried out in accordance with the testing procedures outlined in Chapter 2. The experimental force displacement data obtained for bearing B1-11 are presented in Figure 3.1. The vertical displacements were measured using four laser displacement transducers (LDT), one placed at each side of the upper and lower steel plates (see Figure 2.4). The four individually measured vertical displacement values were averaged to evaluate the vertical displacement of the

bearing for a given vertical force. Figure 3.1 shows that the resultant force displacement curves exhibit a response behaviour known as run-in, which can be attributed to the initial straightening that occurs in the fibre fabric reinforcement under the action of applied vertical load (Kelly 1999). The nonlinear response behaviour is also partially attributed to the elastomer characteristics in compression (Robert 1988). To reduce the run-in effect, the fibre fabric reinforcement was pre-tensioned prior to laminating it to the elastomer layers during the construction of the bearings.

The vertical stiffness, K_v, was evaluated using Equation 3.1,

$$K_v = \frac{P_2 - P_1}{Y_2 - Y_1} \qquad 3.1$$

where P_2 and P_1 are the maximum and minimum vertical force values, respectively, for a given cycle and Y_2 and Y_1 are the corresponding maximum and minimum displacement values. Figure 3.2 shows a visual representation of the slope of K_v obtained using Equation 3.1.

Using the experimentally evaluated vertical stiffness, a direct relationship can be made to the elastic compression modulus using Equation 3.2

$$E_c = \frac{K_v t_r}{A} \qquad 3.2$$

where K_v is the vertical stiffness, t_r is the total thickness of rubber in the bearing and A is the area of the loaded surface.

The effective compression modulus of a fibre-reinforced bearing can be theoretically obtained by (Tsai and Kelly 2002)

$$E_c = \frac{24GS^2}{\pi^2(\alpha a)^2}\left(1+\frac{a}{b}\right)^2 \sum_{n=1}^{\alpha} \frac{1}{\left(n-\frac{1}{2}\right)^2}\left(\frac{tanh\,\gamma_n b}{\gamma_n b} - \frac{\tanh b_n b}{\beta_n b} + \frac{\tanh \bar{\gamma}_n a}{\bar{\gamma}_n a} - \frac{\tanh \bar{\beta}_n a}{\bar{\beta}_n a}\right) \quad 3.3$$

where a and b are half the length of the sides of the bearing. α, γ_n, β_n, $\bar{\gamma}_n$ and $\bar{\beta}_n$ and are defined by Equation 3.4 to 3.8.

$$\alpha = \sqrt{\frac{12G(1-v^2)}{E_f t_f t}} \quad 3.4$$

$$\gamma_n = \left(n-\frac{1}{2}\right)\frac{\pi}{\alpha} \quad 3.5$$

$$\beta_n = \sqrt{\gamma_n^2 + \alpha^2} \quad 3.6$$

$$\bar{\gamma}_n = \left(n-\frac{1}{2}\right)\frac{\pi}{b} \quad 3.7$$

$$\bar{\beta}_n = \sqrt{\bar{\gamma}_n^2 + \alpha^2} \quad 3.8$$

E_f, t_f, t and v are the elastic modulus, thickness of fibre, thickness of rubber and Poisson's ratio of the fibre reinforcement, respectively. The above equations are derived from a pressure solution described in detail by Tsai and

Kelly (2002). Since the bearing design in this study has two different elastomer thicknesses, an equivalent vertical compression modulus is calculated using Equation 3.9.

$$E_{c,eq} = \frac{t_r}{\frac{t_{r1}}{E_{c1}} + \frac{t_{r2}}{E_{c2}}} \qquad 3.9$$

The vertical stiffness can be obtained from the rearrangement of Equation 3.2. The theoretically obtained value of the vertical stiffness is found to be 13.8kN/mm.

The experimental vertical frequency, f_v, which is a function of K_v, is evaluated using Equation 3.10,

$$f_v = \frac{1}{2\pi}\sqrt{\frac{K_v g}{P}} \qquad 3.10$$

where g is the acceleration due to gravity and P, is the vertical load on the bearing.

The experimentally evaluated values of K_v, E_c, and f_v are shown in Table 3-1 for the three bearings tested. The results presented in the table show a reduction in vertical stiffness with each cycle, with the largest reduction occurring between the first and second cycles. This reduction in vertical stiffness in successive cycles was also observed by Toopchi-Nezhad et al. (2009c).

Inspection of the data reveals that the vertical stiffness increases with increased applied load, which is shown in Figure 3.3 along with the theoretically evaluated vertical stiffness. The predicted value of K_v is in good agreement with experimentally obtained values at low vertical load values. The deviation between the theoretical and experimentally obtained stiffness value increases as the vertical load is increased. The increase in vertical stiffness with higher vertical loading is partially attributed to the carbon fibre fabric reinforcement. As the vertical load is increased, the carbon fibre fabric experiences higher tension, thus straightening the fibre strands and increasing the effective fibre modulus (Kelly and Takhirov 2002).

The calculated vertical frequency values of the tested bearings ranged from approximately 16 to 32 Hz. This is approximately 17 times larger than the estimated base isolated structures lateral frequency range of 0.8 - 2Hz. Therefore, rocking induced motion is expected to be insignificant for the SU-FREI base isolated structure considered in this study.

Upon completion of each vertical test, the bearing was removed and inspected for any visible signs of damage. No damage was observed to have occurred in any of the tested bearings.

3.3 Lateral Cyclic Testing

Lateral cyclic testing was performed on the bearings to obtain hysteresis loops (lateral force displacement data) for the purpose of evaluating the effective

lateral stiffness and damping properties. These two properties are important, as they are needed for design to evaluate the structural period and displacement values of the isolated structure. A total of seven bearings (B1-11, B1-13, B1-23, B3-21, B3-12, B4-21 and B4-11) were tested using the lateral cyclic testing procedures described in Chapter 2. Bearing B3-12, B4-21 and B4-11 were tested up to a maximum normalized displacement amplitude of 200%t_r, where t_r is the total rubber thickness (19.05mm). Bearings B1-11, B1-13, B1-23 and B3-21 were tested up to a maximum normalized lateral displacement of 250%t_r to investigate the effective properties at lateral displacements larger than those considered in previous studies (Toopchi-Nezhad 2008).

Deformations of the bearings at the prescribed normalized lateral displacement amplitudes, defined in the testing protocol in Chapter 2, are shown in Figure 3.4. From this figure, it is seen that the initial deformation at 25%t_r is pure shear. As the displacement amplitude increases, the bearing experiences rollover deformation. The rollover deformation acts to decrease the lateral stiffness of the bearing until contact of the initially vertical surfaces is made with the upper and lower platens, at which point the lateral stiffness increases. The change in lateral stiffness with rollover deformation can be observed in the hysteresis loops of the tested bearings shown in Figure 3.5.

The method utilized to calculate the effective lateral stiffness, $K_{h,eff}$, is based on the peak lateral displacement and peak lateral load and is given by Equation 3.11 (ASCE 2005).

$$K_{h,eff} = \frac{F_{max} - F_{min}}{\Delta_{max} - \Delta_{min}} \qquad 3.11$$

The variables F_{max}, F_{min}, Δ_{max}, and Δ_{min} are the peak maximum and minimum values of the lateral load and displacement, respectively.

The effective damping, β_{eff}, calculated using Equation 3.12, is dependent on the total energy dissipated within each cycle, E_{loop}, which is determined from the area enclosed by the load-displacement curve defining each hysteresis loop

$$\beta_{eff} = \frac{2}{\pi}\left(\frac{E_{loop}}{K_{eff}(|\Delta_{max}| + |\Delta_{min}|)^2}\right) \qquad 3.12$$

The calculated effective stiffness and damping values are shown in Table 3-2 and Table 3-3. From the data presented in the tables it can be observed that the effective stiffness decreases as the bearing is cycled at a given lateral displacement amplitude. This is due to scragging, which was discussed in Section 1.5.1. The scragging effect is significantly less pronounced during subsequent cycles. These finding are consistent with those observed by Toopchi-Nezhad (2008) and de Raaf (2009). The reduction in stiffness seen in the hysteresis loops of Figure 3.5 is also seen in Table 3-2 and Table 3-3. The trends of lateral stiffness as a function of lateral displacement are advantageous. The high initial stiffness limits displacements during serviceability (wind) loading. As rollover occurs, the reduced stiffness increases the period, thus increasing the efficiency of the bearings during an earthquake.

The lateral stiffness, assuming a pure shear deformation, can be estimated using Equation 3.13,

$$K_h = \frac{GA}{t_r} \tag{3.13}$$

where K_h is the lateral stiffness, G is the shear modulus of the rubber, taken as 0.35MPa. A, is the area of the loaded surface, 3969mm^2, and t_r is the total thickness of rubber in the bearing, 19.05mm. Using equation 3.13, a lateral stiffness value of 72.9N/mm is obtained. The value is in good agreement with the experimentally obtained average stiffness value of 74.9N/mm at 25%t_r. This is due to the shearing deformation experienced at low amplitude displacements before significant rollover occurs. As the bearing begins to roll over, contact surface is lost and the area, A, decreases thus lowering the effective stiffness, K_h, which is seen in the experimental results shown in Table 3-2 and Table 3-3.

At normalized lateral displacement amplitudes of 200%t_r and greater, the effective stiffness of the bearing increases (see Figure 3.6). The stiffness increase at 200%t_r is a result of the originally vertical surfaces (faces) of the bearing fully contacting the upper and lower platens. Review of video recordings indicates that full vertical facial contact of the bearings occurred at approximately 200%t_r (see Figure 3.4).

Kelly and Konstantinidis (2007) derived the following expression (Equation 3.14) to estimate ultimate displacement (full vertical facial contact) of an unbonded bearing with flexible reinforcement,

$$\Delta_{fc} = \frac{5h}{3t_r} \qquad 3.14$$

where t_r is the total thickness of rubber and h is the total height of the bearing, including the reinforcement layers. Using the above expression, the predicted displacement corresponding to full vertical facial contact for the bearings investigated in this study was approximately 201%t_r. This value is in good agreement with that observed during experimental testing.

The damping results tabulated in Table 3-2 and Table 3-3 provide an averaged damping ratio of approximately 9.8% at 25%t_r. This value is approximately 2 times greater than the 5% damping specified for the elastomer. The increased level of damping in fibre reinforced elastomeric isolators has been observed by others in experimental tests (Kelly 1999), (Toopchi-Nezhad 2008), (de Raaf 2009) and the source of the additional damping has been postulated by Kelly (1999) to be a product of the flexible fibre fabric reinforcement. The additional damping is produced from the tension in the fibre reinforcement strands. Due to the tension and the rollover deformation of SU-FREI bearings, the fibres of the reinforcement slip against one another causing frictional forces that dissipate energy. This additional damping is not found in steel reinforced elastomeric isolators (SREI) bearings. This increased damping is advantageous, as the additional damping limits displacements and the bearings do not require special high damping rubber. The trend of the damping with respect to lateral displacement amplitude is graphically shown in Figure 3.7. The damping

decreases as the displacement amplitude increases up to 150%t_r; at this amplitude the damping increases slightly and then decreases again at 200%t_r, leveling out to a constant value of approximately 8%.

To show the variability in the experimentally obtained lateral stiffness and damping values, the average effective lateral stiffness and damping for each displacement amplitude tested along with one standard deviation error bars are shown in Figure 3.6 and Figure 3.7. Table 3-4 gives the mean, standard deviation and coefficient of variation for each normalized displacement amplitude. ASCE 7 (2005) states that for test specimen adequacy the stiffness of all cycles of a displacement amplitude must be within 15% of each other and of their mean value. The results of the statistical analysis indicate that the bearings satisfy the limitations of the ASCE 7 (2005) as shown in Figure 3.6.

3.3.1 Influence of Vertical Load

The influence of vertical load on effective lateral stiffness and damping properties are examined in this section. Three bearings denoted B3-12, B4-21 and B4-11 were tested using the lateral cyclic testing procedures presented in Chapter 2. Each bearing was tested to a maximum normalized lateral displacement amplitude of 200%t_r. Bearing B3-12 was tested under a 2kN load; B4-12 a 4kN load; and B4-11 a 12kN load. The hysteresis loops for the three bearings are shown in Figure 3.8. The calculated effective stiffness and damping are shown in Table 3-5. Test results show that as the vertical load increases, the effective lateral stiffness of the bearing decreases, while the damping increases. The increased

damping associated with the increased vertical loading is assumed to be related to the damping provided by the carbon fibre reinforcement. For comparison purposes, effective lateral stiffness and damping values listed in Table 3-5 have been normalized with respect to 8kN vertical load test results and are plotted in Figure 3.9 and Figure 3.10, respectively. The normalized effective lateral stiffness is found to fluctuate approximately 30% and the effective damping approximately 40% over the range of vertical loads considered. The observed trends are in agreement with response behaviour described by other researchers including Kelly (1999), Tsai and Kelly (2004) and de Raaf (2009).

3.3.2 Observed Damage Assessment

After each test, the bearing was removed from the testing device and inspected for signs of damage in the form of delamination. Upon completion of all testing, B3-21 was the only bearing observed to have experienced any visible damage. A small delamination occurred at approximately the mid height of the bearing between the elastomer layer and fibre, shown in Figure 3.11. Upon review of video footage, the damage occurred at the peak displacement of the first cycle of the 250%t_r amplitude.

3.3.3 Influence of Lateral Loading on Vertical Stiffness

Vertical testing was completed before and after lateral testing of bearings B1-11, B1-23, B1-13 and B3-21. The resulting data calculated from the tests is shown in Table 3-6. Results of the test show that the vertical stiffness reduced

after lateral cyclic testing. This loss of stiffness can be attributed to two factors: the first is due to scragging in the vertical direction; and the second from internal damage and scragging in the lateral direction. The data shows that bearings B1-23 and B1-13, with initially higher vertical stiffness had a reduction of around 30%, whereas B1-11 and B3-21 with slightly lower initial vertical stiffness had a reduction of less than 25%. Although a reduction in vertical stiffness was found to occur, the vertical to lateral stiffness ratio remained 120 times greater at low displacement amplitudes and 330 times greater at 150%t_r.

3.4 Rollout Testing

Rollout testing was carried out in accordance with the procedures outlined in Chapter 2 to determine the ultimate displacement limitations of the bearings. These limitations are the displacement amplitude at which the bearing loses stability, (i.e. lack of positive tangential stiffness) and the displacement amplitude at which delamination of the elastomer to fibre occurs. Three bearings, denoted B1-11, B1-13 and B1-23, were selected for rollout testing. A displacement amplitude that would provide delamination or negative tangential stiffness was unknown, therefore, bearing B1-11 was initially tested up to a normalized displacement amplitude of 300%t_r. As no sign of delamination or negative lateral tangential stiffness occurred, the bearing was tested twice more at normalized displacements amplitudes of 350% and 400%t_r. The hysteresis loops obtained from the rollout tests on B1-11 are shown in Figure 3.12. Bearing B1-11

maintained positive lateral tangential stiffness, however, a small delamination occurred between the bottom layer elastomer and fibre sheet at 400%t_r. Bearings B1-13 and B1-23 were subsequently tested at the normalized displacement amplitude of 400%t_r. A photograph of the deformed bearing at the normalized displacement amplitude of 400%t_r is shown in Figure 3.13. From this figure it is seen that substantial rollover deformation has occurred and the bearing has made full vertical facial contact. In fact, most of the contacted surface is due to the originally vertical surfaces as the originally contacted surfaces (horizontal) have rolled to extreme displacements and have lost contact. The hysteresis loops for all three bearings at 400%t_r are shown in Figure 3.14. Upon completion of testing at 400%t_r, delamination was observed to have occurred in both bearings B1-13 and B1-23 as shown in Figure 3.15 and Figure 3.16.

The lateral secant stiffness and tangential stiffness of the bearings was calculated using a backbone curve analysis approach presented by Toopchi-Nezhad et al. (2008c) and further discussed in Chapter 4. The results of the analysis for bearing B1-11 at 400%t_r are shown in Figure 3.17. From the figure, it can be seen that the tangential stiffness of the bearing remained positive. Analysis of all three bearings showed the same behaviour.

In addition to a backbone curve analysis, numerical differentiation of the hysteresis curves was completed to obtain the secant stiffness and tangential stiffness. The term stiffness is used but it is prudent to note that the values do not represent the actual stiffness of the bearing, as the damping force is included in

the hysteresis curves. Figure 3.18 and Figure 3.19 show the numerically differentiated secant stiffness and tangential stiffness plots of the hysteresis loops for bearing B1-11. Figure 3.20 and Figure 3.21 show the calculated stiffness values for the three bearings tested at 400%t_r. The plots show that there is good agreement between the test results. From the figures of the secant stiffness, the bearings have the lowest secant stiffness value at approximately 175%t_r making it the region of highest efficiency. The secant stiffness begins to increase past 175%t_r and level out with a slower rate of increase beyond 201%t_r, which is the expected full vertical facial contact point for the bearing. As for the tangential stiffness, it is lowest at a normalized displacement amplitude of approximately 150%t_r. The tangential stiffness begins to rapidly increase past this point implying that initial facial contact of the originally vertical surfaces is occurring, thus increasing the stiffness of the bearing. The bearing reaches a peak tangential slope at approximately 200%t_r, again within range of expected full vertical facial contact.

3.5 Serviceability

Serviceability requirements are crucial to ensuring occupancy comfort. Base isolated structures can be particularly susceptible to wind loading due to the flexible isolation layer. Therefore, the bearings in this study are tested under wind load excitation. The wind load testing procedures described in Chapter 2 were completed on bearing B2-11. As all wind load testing was completed on a single

bearing the tests were completed in ascending amplitude of force to capture the unscragged hysteresis properties. The hysteresis loops corresponding to the three amplitudes are shown in Figure 3.22 to Figure 3.24. Due to testing under load control, as discussed in Chapter 2, the displacements increased as the bearing was cycled due to decreasing stiffness. The decreasing lateral stiffness and increase in displacement amplitude with each cycle is due to scragging and can be seen in the hysteresis loops as well as the displacement time history plot for the maximum wind loading test (q=0.6kPa), shown in Figure 3.25.

The calculated stiffness and damping values corresponding to the three amplitudes of wind loading (q=0.31kPa, 0.4kPa and 0.6kPa) are summarized in Table 3-7. From the data in the table, the effects of scragging can be quantified. The stiffness reduction over the 20 cycles for q values of 0.31kPa, 0.4kPa and 0.6kPa are, respectively, 6.7%, 8.4% and 15%. The lateral stiffness data is normalized with respect to the first cycle and is visually represented in Figure 3.26. The effective damping is normalized with respect to the first cycle and is shown in Figure 3.27. From Figure 3.27 it is seen that the largest damping value corresponded to q=0.4kPa (approximately 50%t_r). The total reduction in damping over 19 cycles was found to be 7.4%, 1.1% and 1% for 0.31kPa, 0.4kPa and 0.6kPa, respectively. Note that damping was only considered up to 19 cycles as the 20th cycle loop returns to a zero load.

Upon completion of the tests, the bearing was inspected for signs of damage, with no visible signs observed. The ASCE 7 (2005) test specimen

adequacy requirements state that a specimen should not lose more than 20% of its initial stiffness over twenty cycles. From this statement, the bearing tested in this study satisfies ASCE 7 (2005) limitations with acceptable degradation values of both lateral stiffness and damping.

3.6 Fatigue Testing

In accordance with procedures for fatigue testing described in Chapter 2, two bearings denoted B4-12 and B2-21 were laterally cycled at a frequency of 1.03Hz under displacement control at the prescribed normalized displacement amplitude of 150%t_r. The data obtained from the tests is shown in Figure 3.28 and Figure 3.29 in the form of hysteresis plots. The data was used to numerically calculate the effective lateral stiffness and damping for both bearings, which are shown in Table 3-8. The effective lateral stiffness and damping for both bearings are displayed in Figure 3.30 and Figure 3.31, respectively. The largest reduction in both stiffness and damping occurs within the first few cycles. This behaviour is consistent with that observed during serviceability testing. The reduction in lateral stiffness and damping were 11.8% and 19% for bearing B4-12 and 17.9% and 20%, respectively for bearing B2-21. ASCE 7 (2005) states that to satisfy test specimen adequacy, the bearings lateral stiffness and damping cannot fall below 20% of the first cycle's values. The above results indicate that the bearings conform to this requirement. Upon completion of testing, both bearings were inspected for damage with neither bearing showing any visible signs.

3.7 Conclusions and Comments

From the testing completed on the SU-FREI bearings, a substantial amount of data was obtained and presented within this chapter. The results of the vertical testing show the vertical stiffness ranged between ≈14 to 18kN/mm at the design vertical load of 8kN. Comparing the results of the experimental data to a theoretical evaluation of stiffness proposed by Tsai and Kelly (2002), the theoretical stiffness of 13.8kN/mm was in good agreement with experimental results for low vertical loads (14.41kN/mm), while underestimating the vertical stiffness at higher vertical loads.

The bearings, laterally cycled at low amplitude displacements, had lateral stiffness values ranging between 69N/mm to 85N/mm. This provided a vertical stiffness that was approximately 165 times greater than the lateral stiffness. The lateral stiffness of the bearings for low amplitude displacements was in good agreement with the theoretical predicted value. However, the theoretical prediction overestimates lateral stiffness as the bearing experiences higher displacements due to rollover effects. The decrease in effective lateral stiffness is a positive feature of SU-FREI bearings as it lengthens the period of the isolated structure, providing increased isolator efficiency. At full vertical facial contact the, lateral stiffness increased, ensuring stability of the bearings. The full vertical facial contact, which occurred at approximately 200%t_r, was in good agreement with the theoretically predicted value.

The influence of vertical loading on lateral cyclic testing was examined and results showed that as the vertical load increased, the effective lateral damping of the bearing increased, while the effective lateral stiffness decreased. Upon completion of lateral cyclic testing, vertical testing was completed at the 8kN design load to determine vertical stiffness degradation. Vertical stiffness degradation between 21 and 30% occurred; despite this reduction the vertical stiffness remained 120 to 330 times greater than the lateral stiffness. Bearing B3-21 was the only bearing to experience any visible signs of damage during lateral cyclic testing. The bearing experienced a small delamination near the mid-height layer of elastomer and fibre fabric at the normalized displacement amplitude of 250%t_r.

Rollout testing of the bearings showed that they are not susceptible to loss of stability in the typical working range of 100%t_r to 250%t_r. The normalized displacement amplitude of 400%t_r could be considered an upper bound limit to the bearings as all three bearings tested experienced some level of delamination at this displacement amplitude. The testing also showed that delamination has little effect on stability, as all three of the bearings experienced delamination but maintained positive lateral load resisting capacity (positive tangential stiffness).

The results of the serviceability tests showed that the bearings were capable of providing adequate stiffness to the structure under low-level accelerations from wind forces. The degradation of the bearings' lateral stiffness and damping fell within code specified limits.

Fatigue testing was conducted within the displacement amplitude of the bearings minimal stiffness (150%t_r). It was found that the bearings maintained adequate stiffness after repeated cyclic loading. The losses associated with fatigue loading, like serviceability, were within code specified limits.

Table 3-1 Vertical test results.

		B1-11			B1-23			B1-13		
Load (kN)	Cycle	Stiffness (kN/mm)	Modulus (MPa)	Frequency (Hz)	Stiffness (kN/mm)	Modulus (MPa)	Frequency (Hz)	Stiffness (kN/mm)	Modulus (MPa)	Frequency (Hz)
4	1	13.4	64.1	28.9	15.8	75.9	31.3	16.5	79.0	32.0
	2	12.8	61.6	28.3	14.7	70.5	30.2	15.4	73.9	30.9
	3	12.5	60.1	27.9	14.0	67.4	29.5	14.6	70.0	30.1
8	1	15.6	74.7	22.0	17.1	82.2	23.1	18.0	86.3	23.7
	2	14.4	69.3	21.2	15.9	76.1	22.2	16.6	79.5	22.7
	3	13.9	66.6	20.8	15.2	72.9	21.7	15.8	76.0	22.2
12	1	17.9	85.7	19.2	19.4	93.1	20.1	20.6	98.7	20.7
	2	16.3	78.0	18.4	17.6	84.5	19.1	18.6	89.4	19.7
	3	15.4	74.0	17.9	16.7	79.9	18.6	17.6	84.6	19.1
16	1	20.5	98.4	17.8	22.1	106.3	18.6	23.8	114.2	19.2
	2	18.3	88.0	16.9	20.0	96.1	17.6	21.3	102.5	18.2
	3	17.1	82.0	16.3	18.8	90.0	17.1	19.9	95.4	17.6

Table 3-2 Effective lateral stiffness and damping values (25%t_r – 250%t_r).

Displacement Amplitude (%t_r)	Cycle	B1-11 Effective Stiffness (N/mm)	B1-11 Effective Damping (%)	B1-13 Effective Stiffness (N/mm)	B1-13 Effective Damping (%)	B1-23 Effective Stiffness (N/mm)	B1-23 Effective Damping (%)	B3-21 Effective Stiffness (N/mm)	B3-21 Effective Damping (%)
25	1	69.4	8.8	85.2	10.6	73.2	9.0	75.8	9.1
	2	68.9	9.5	83.8	11.4	72.2	9.5	73.7	9.6
	3	68.4	9.7	83.1	11.2	71.8	9.8	73.3	9.2
50	1	59.6	8.8	70.5	10.5	62.1	9.2	63.8	9.3
	2	57.4	8.4	67.4	10.2	59.7	8.8	60.7	8.6
	3	56.9	8.3	66.6	10.2	59.1	8.6	60.0	8.6
75	1	51.5	8.4	59.1	10.0	53.2	8.7	54.3	8.7
	2	49.3	7.9	56.1	9.7	50.9	8.3	51.5	8.2
	3	48.7	7.9	55.4	9.6	50.3	8.3	50.9	8.1
100	1	44.9	8.1	50.8	9.8	46.2	8.5	46.9	8.6
	2	43.0	7.6	48.3	9.5	44.2	8.0	44.6	8.0
	3	42.4	7.6	47.5	9.4	43.6	8.0	43.9	8.0
150	1	35.6	9.3	40.4	10.6	37.0	9.4	37.9	9.4
	2	33.7	7.8	38.2	9.5	35.1	8.2	35.9	8.1
	3	33.0	7.8	37.4	9.4	34.5	8.1	35.1	8.1
200	1	37.4	8.0	43.6	9.0	38.5	8.3	39.8	8.3
	2	34.4	7.0	40.4	8.0	35.7	7.2	36.6	7.3
	3	33.3	6.9	39.1	8.0	34.8	7.1	35.5	7.3
250	1	42.4*	7.9*	45.9	8.7	41.8	7.8	42.7	8.1
	2	39.6*	7.2*	42.5	7.9	38.6	7.0	39.2	7.5
	3	38.4*	7.2*	41.2	7.9	37.5	6.9	38.0	7.7

*-These values were extracted from a retest on B1-11 as the maximum displacement of the initial test only 200%t_r.

Table 3-3 Effective lateral stiffness and damping values (25%t_r – 200%t_r).

Displacement Amplitude (% t_r)	Cycle	B3-12 (8kN) Effective Stiffness (N/mm)	B3-12 (8kN) Effective Damping (%)	B4-21 (8kN) Effective Stiffness (N/mm)	B4-21 (8kN) Effective Damping (%)	B4-11 (8kN) Effective Stiffness (N/mm)	B4-11 (8kN) Effective Damping (%)
25	1	71.9	9.2	72.9	9.3	83.6	9.2
	2	70.9	10.5	71.9	10.1	81.0	9.6
	3	70.3	10.1	71.3	10.3	80.3	9.6
50	1	58.9	9.7	59.6	9.7	68.1	9.5
	2	57.2	9.4	57.9	9.4	64.8	8.7
	3	56.7	9.4	57.4	9.4	64.0	8.6
75	1	49.3	9.2	49.7	9.1	57.0	8.8
	2	47.7	9.1	48.2	9.1	54.1	8.3
	3	47.3	9.0	47.8	9.1	53.4	8.2
100	1	42.7	9.1	43.0	9.0	49.1	8.6
	2	41.4	8.9	41.8	8.9	46.8	8.0
	3	41.0	8.9	41.4	8.9	46.1	7.9
150	1	35.7	9.6	35.6	9.6	39.2	9.6
	2	34.5	8.7	34.4	8.7	37.1	8.2
	3	34.0	8.7	33.9	8.7	36.3	8.2
200	1	40.6	8.2	39.6	8.2	42.2	8.5
	2	38.0	7.5	37.3	7.4	38.8	7.6
	3	36.9	7.4	36.4	7.3	37.7	7.5

Table 3-4 Statistical analysis of effective lateral stiffness and damping.

Displacement (%t_r)	Mean	Standard Deviation	Coefficient of Variation (%)
25	74.9	5.3	7.1
50	61.4	4.0	6.6
75	51.7	3.3	6.3
100	44.7	2.7	6.0
150	35.9	1.9	5.2
200	37.9	2.5	6.6
250	40.7	2.4	5.9

Table 3-5 Variation in effective lateral stiffness and damping with vertical load.

Displacement ($\%t_r$)	Cycle	B3-12 (2kN)		B4-21 (4kN)		B4-11 (12kN)	
		Stiffness (N/mm)	Damping (%)	Stiffness (N/mm)	Damping (%)	Stiffness (N/mm)	Damping (%)
25	1	85.0	8.4	73.5	9.4	66.0	10.8
	2	83.3	8.7	79.9	9.6	65.0	11.7
	3	82.7	8.7	78.4	10.0	64.4	11.9
50	1	68.6	8.2	65.5	9.3	54.6	11.4
	2	66.5	7.4	59.9	7.6	52.4	11.3
	3	65.8	7.4	64.8	8.0	51.8	11.1
75	1	57.1	7.6	56.7	8.0	46.6	10.9
	2	55.1	7.0	54.5	7.5	44.6	10.9
	3	54.5	7.0	54.1	7.4	44.0	11.0
100	1	49.4	7.4	49.4	7.7	40.4	10.9
	2	47.9	6.7	47.9	7.1	38.7	10.9
	3	47.3	6.7	47.6	7.0	38.1	11.0
150	1	40.0	8.5	40.2	8.4	33.9	11.8
	2	38.5	6.8	38.6	7.0	32.4	11.1
	3	37.9	6.6	37.8	6.9	31.8	11.1
200	1	42.6	8.9	44.3	7.1	36.6	10.9
	2	40.3	8.1	40.7	6.3	34.1	10.3
	3	39.0	7.8	40.5	5.6	33.1	10.4

Table 3-6 Vertical testing to investigate influence of lateral loading.

		Test 1			Test 2			% Reduction		
Bearing	Cycle	Stiffness (kN/mm)	Modulus (Mpa)	Frequency (Hz)	Stiffness (kN/mm)	Modulus (Mpa)	Frequency (Hz)	Stiffness	Modulus	Frequency
B1-11	1	15.6	74.7	22.0	12.0	57.8	19.4	22.6	22.6	12.1
	2	14.4	69.3	21.2	11.4	54.5	18.8	21.3	21.3	11.4
	3	13.9	66.6	20.8	11.0	53.0	18.5	20.4	20.4	10.9
B1-23	1	17.1	82.2	23.1	11.9	57.0	19.2	30.6	30.6	16.6
	2	15.9	76.1	22.2	11.1	53.2	18.6	30.1	30.1	16.3
	3	15.2	72.9	21.7	10.6	50.7	18.1	30.4	30.4	16.5
B1-13	1	18.0	86.3	23.7	12.7	60.8	19.9	29.6	29.6	16.0
	2	16.6	79.5	22.7	11.6	55.8	19.0	29.8	29.8	16.2
	3	15.8	76.0	22.2	11.0	52.8	18.5	30.5	30.5	16.6
B3-21	1	16.4	78.7	22.6	12.3	59.3	19.6	24.7	24.7	13.1
	2	15.3	73.3	21.8	11.5	55.1	18.9	24.8	24.8	13.2
	3	14.5	69.7	21.2	11.1	53.1	18.5	23.9	23.9	12.7

Table 3-7 Wind loading test data for service, design and maximum wind loading conditions.

Cycle	q=0.31kPa		q=0.4kPa		q=0.6kPa	
	Effective Stiffness (N/mm)	Effective Damping (%)	Effective Stiffness (N/mm)	Effective Damping (%)	Effective Stiffness (N/mm)	Effective Damping (%)
1	77.4	9.5	70.4	9.0	55.9	9.9
2	75.8	9.0	68.4	9.0	53.1	9.0
3	74.9	8.9	67.5	8.9	51.6	9.0
4	74.2	8.9	67.1	9.0	50.7	8.9
5	74.0	8.9	66.7	8.9	50.2	8.8
6	73.7	8.8	66.2	8.9	49.7	8.9
7	73.5	9.0	65.9	8.8	49.4	8.8
8	73.0	8.8	65.8	8.8	49.1	8.9
9	73.1	8.9	65.6	8.8	48.9	8.9
10	73.1	8.8	65.4	8.9	48.7	8.9
11	72.8	8.8	65.3	8.9	48.5	8.9
12	72.6	8.9	65.2	8.9	48.3	8.9
13	72.8	8.9	64.9	8.7	48.2	8.9
14	72.6	8.8	65.0	9.0	48.1	8.9
15	72.5	8.7	64.9	8.9	48.0	8.9
16	72.4	8.9	64.8	8.9	47.9	8.9
17	72.3	8.8	64.7	8.9	47.8	8.9
18	72.3	8.8	64.7	8.9	47.7	8.8
19	72.2	8.8	64.5	8.9	47.6	8.9
20	72.2	8.5	64.5	8.4	47.5	8.4

Table 3-8 Fatigue test results.

	B4-12				B2-21			
Cycle	Effective Stiffness (N/mm)	% Reduction	Effective Damping (%)	% Reduction	Effective Stiffness (N/mm)	% Reduction	Effective Damping (%)	% Reduction
1	41.0	-	11.1	-	38.8	-	11.9	-
2	39.0	4.9	9.5	13.9	36.4	6.2	10.5	11.4
3	38.1	7.0	9.4	14.7	35.5	8.5	10.6	11.4
4	37.5	8.6	9.4	14.9	35.0	9.8	10.6	11.3
5	37.1	9.6	9.4	14.7	34.3	11.5	10.6	11.0
6	36.9	9.9	9.4	14.8	33.7	13.1	10.6	11.3
7	36.5	10.9	9.4	15.5	33.4	13.9	10.6	10.8
8	35.8	12.6	9.6	13.4	33.1	14.7	11.0	7.3
9	35.8	12.7	9.3	16.0	32.3	16.6	9.9	17.2
10	36.2	11.8	9.0	19.0	31.8	17.9	9.5	20.5

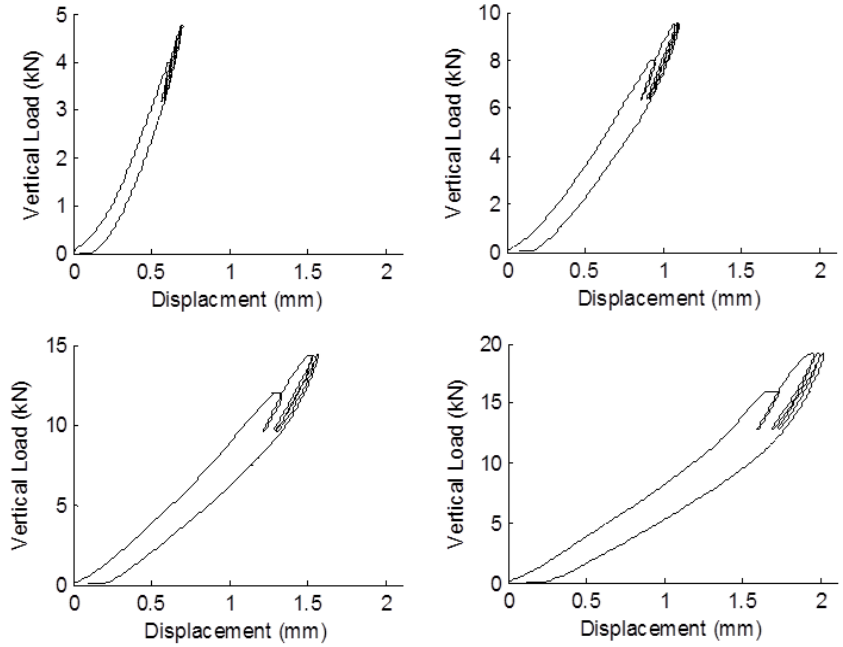

Figure 3.1 Vertical load versus displacement (bearing B1-11) at 4kN, 8kN, 12kN and 16kN.

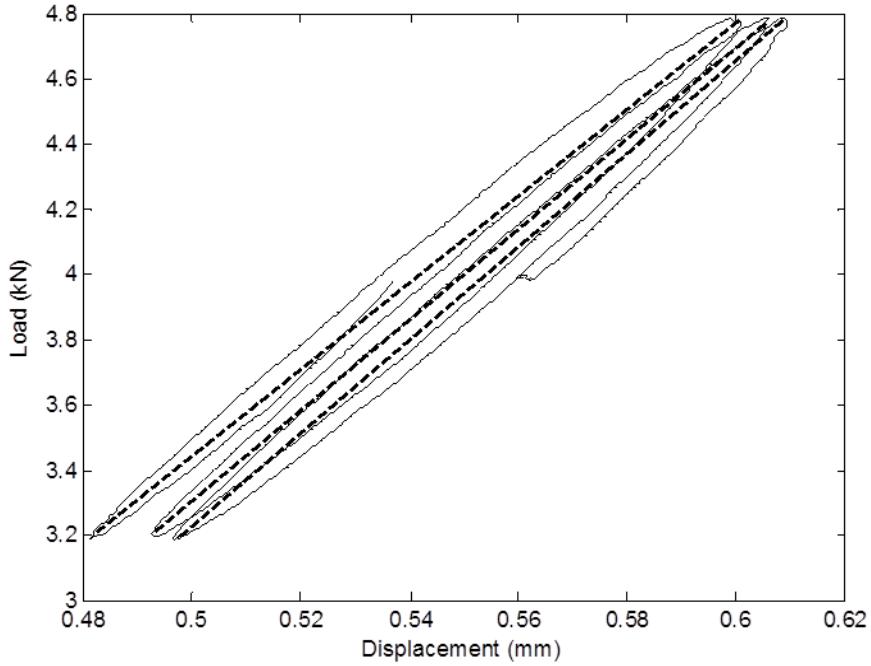

Figure 3.2 Plot of effective vertical stiffness, K_v.

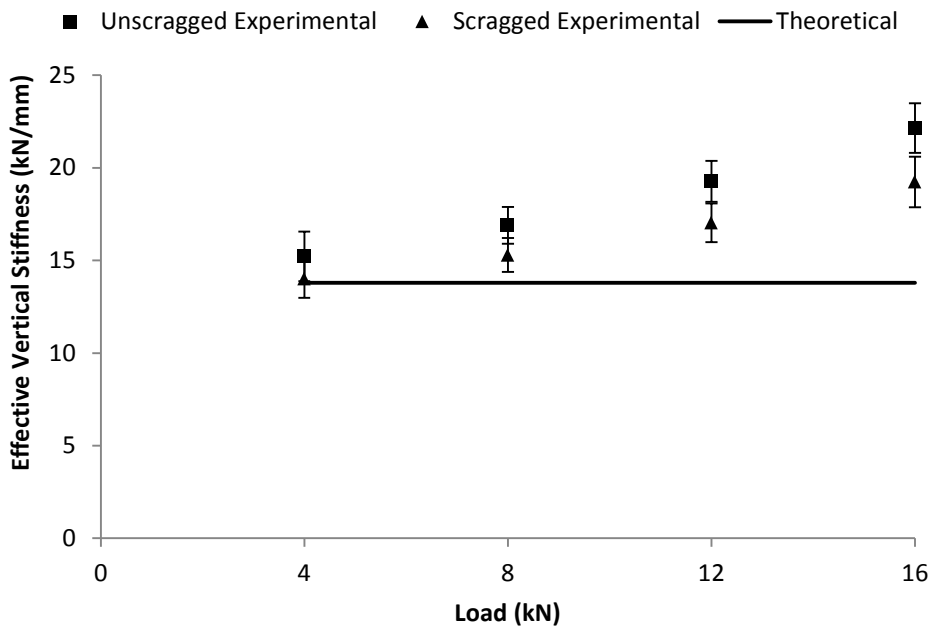

Figure 3.3 Comparison of predicted versus experimentally obtained vertical stiffness values. Experimental results are plotted with ±1 standard deviation.

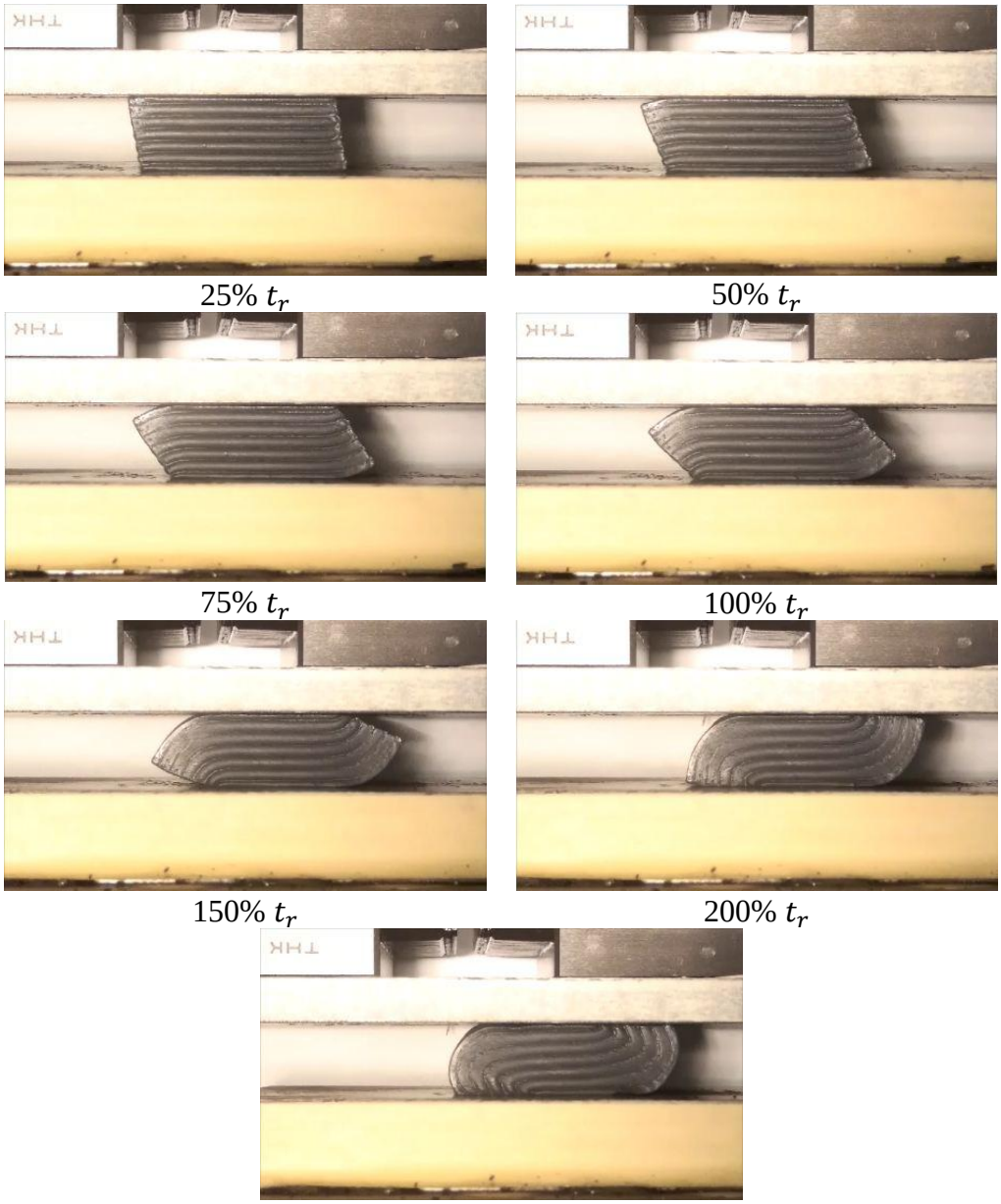

Figure 3.4 Deformation at prescribed lateral displacement amplitudes.

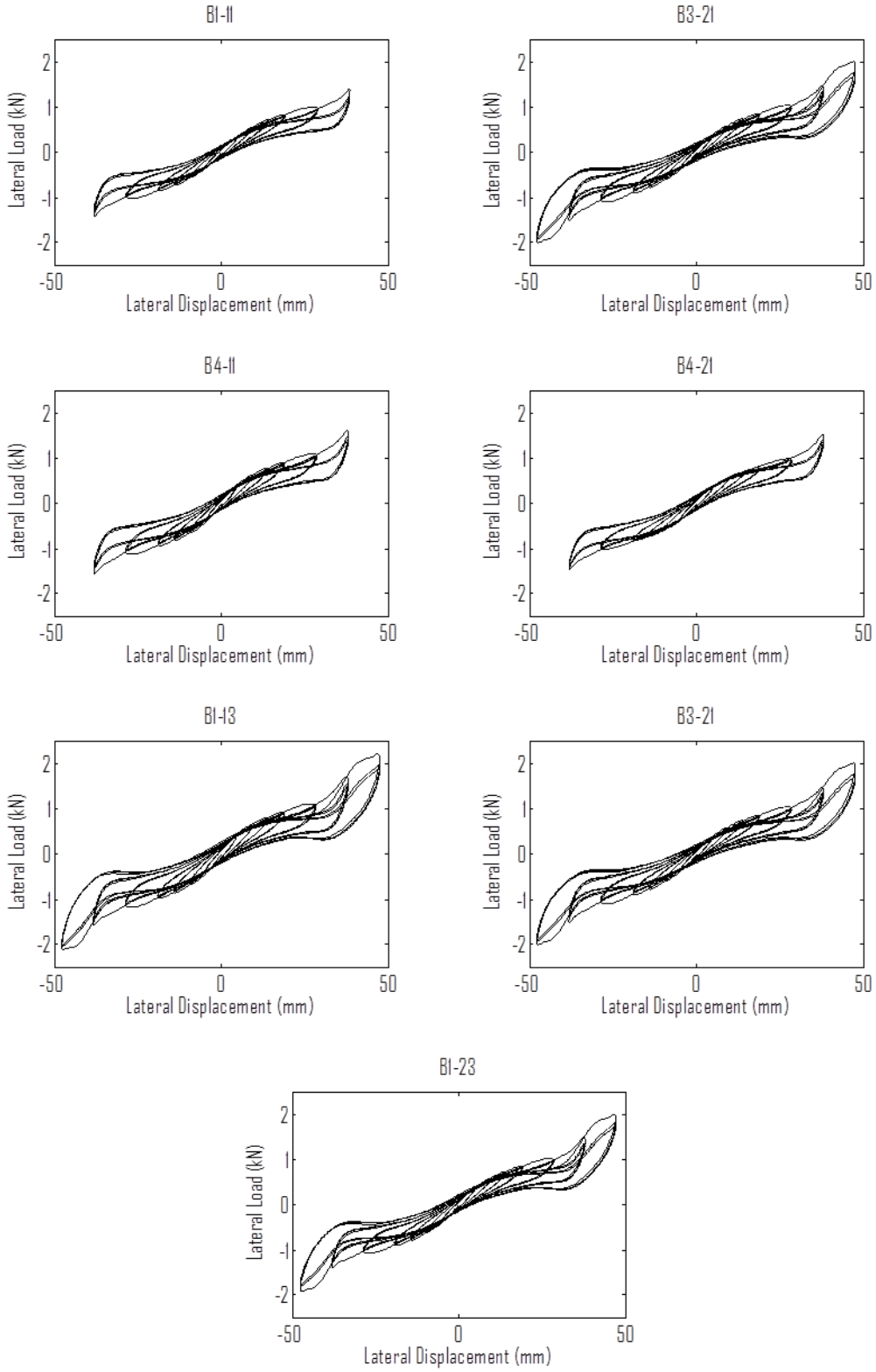

Figure 3.5 Lateral cyclic hysteresis loops.

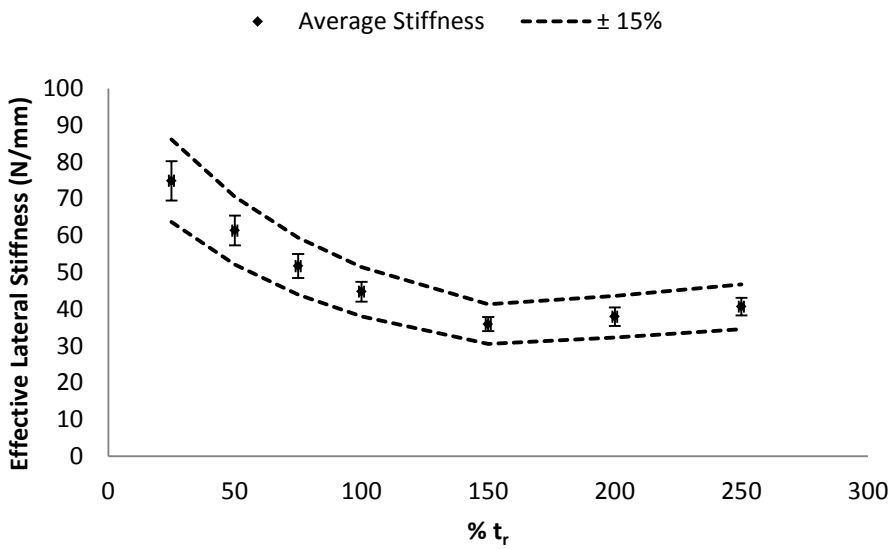

Figure 3.6 Average lateral effective stiffness vs. % t_r, with ±1standard deviation error bars and ±15% average.

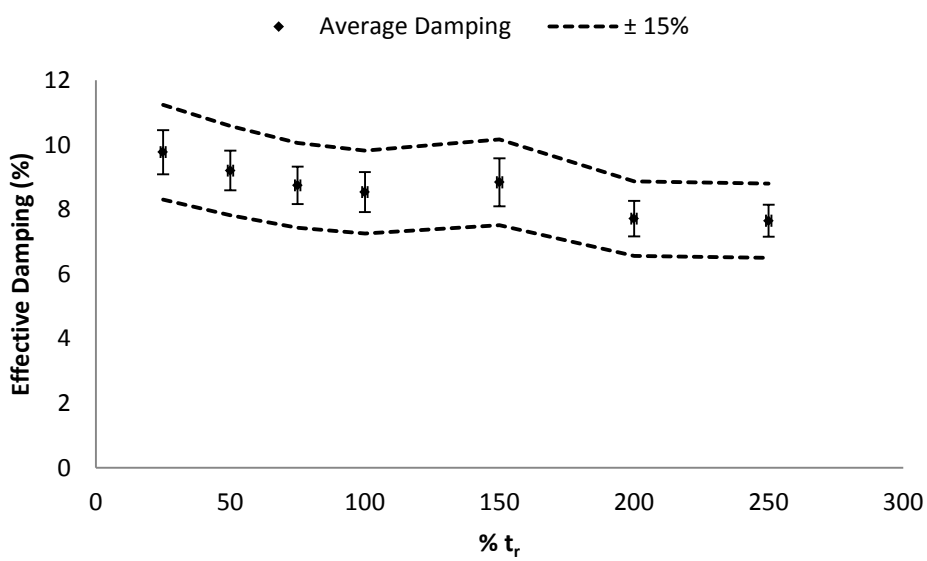

Figure 3.7 Average effective damping vs. % $t_r$with ±1 standard deviation error bars and ±15% average.

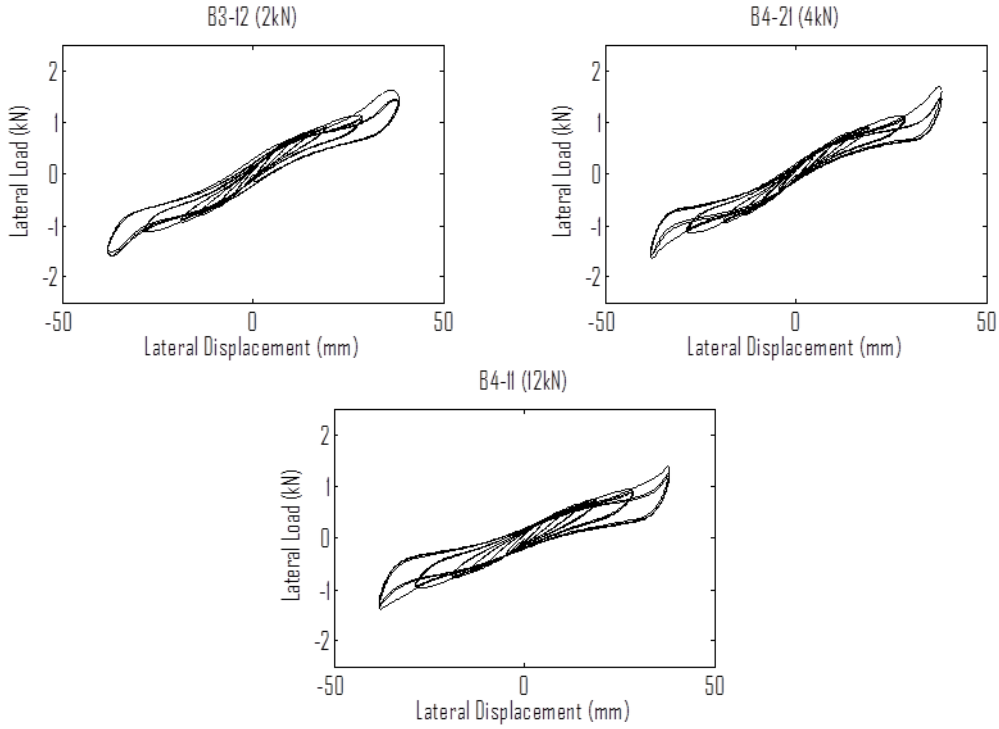

Figure 3.8 Influence of vertical load on lateral hysteresis loops.

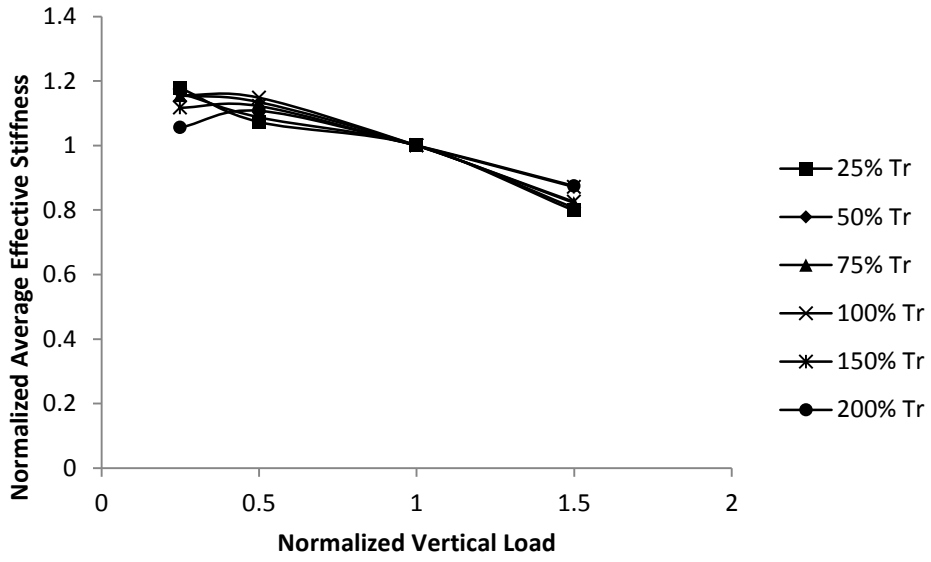

Figure 3.9 Influence of vertical load on normalized average effective lateral stiffness.

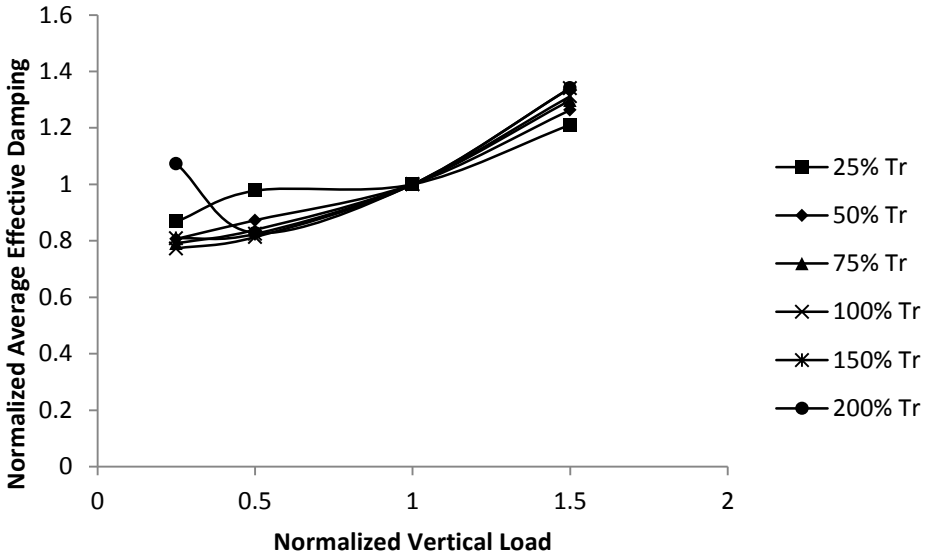

Figure 3.10 Influence of vertical load on normalized average effective damping.

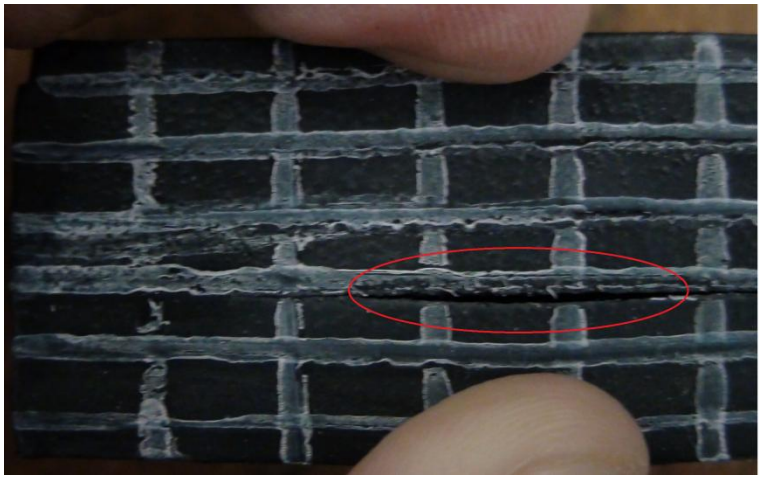

Figure 3.11 Observed delamination in bearing B3-21.

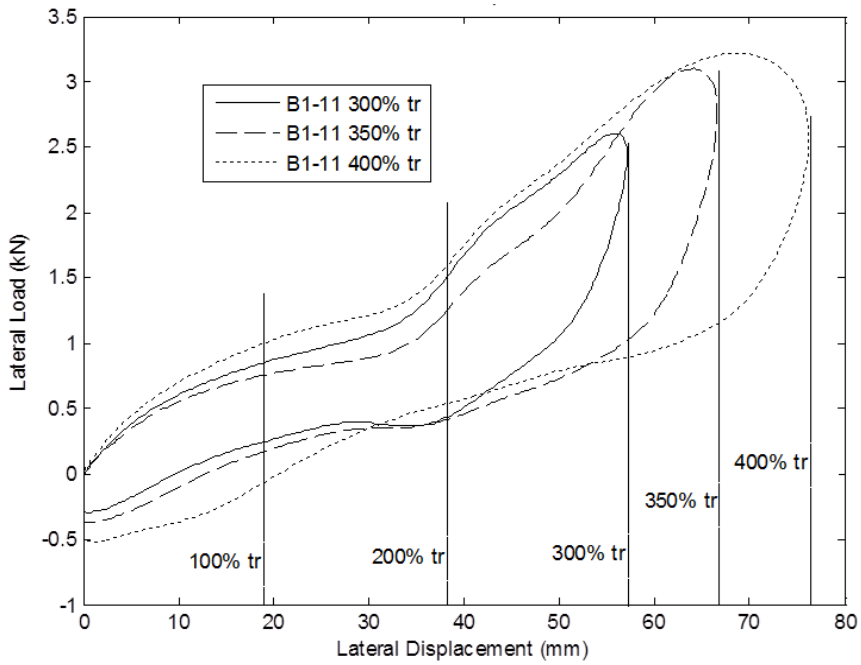

Figure 3.12 Hysteresis loops (bearing B1-11) at rollover amplitudes of 300, 350 and 400%t_r.

Figure 3.13 Rollover deformation at 400%t_r displacement amplitude.

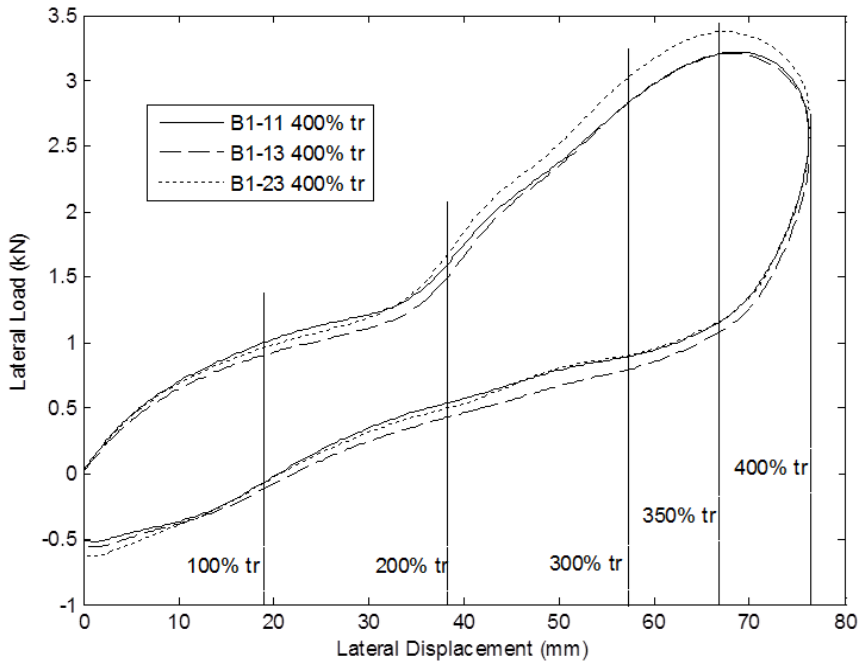

Figure 3.14 Hysteresis loops from rollout tests at 400% t_r displacement amplitude.

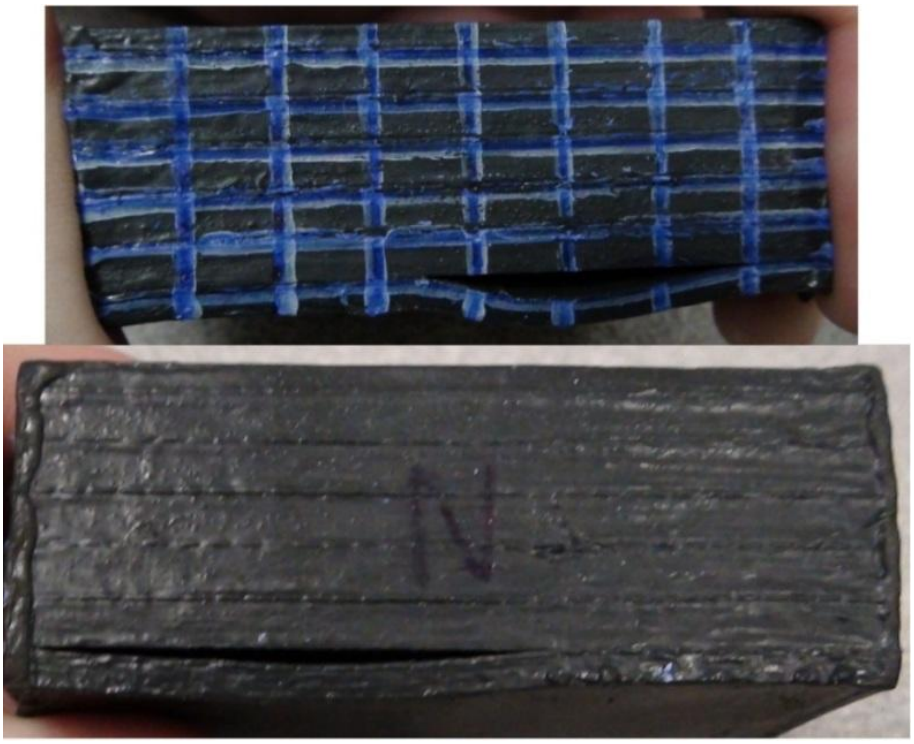

Figure 3.15 Observed delamination in bearing B1-13 at 400%t_r displacement amplitude.

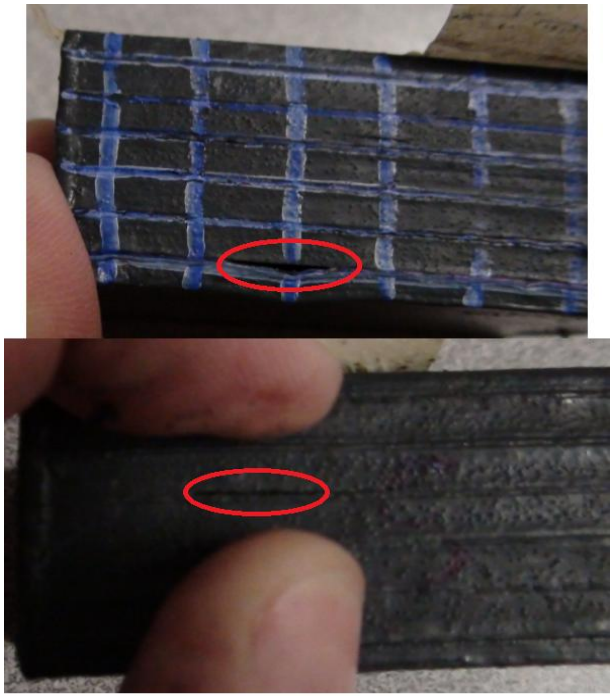

Figure 3.16 Observed delamination in bearing B1-23 at 400%t_r displacement amplitude.

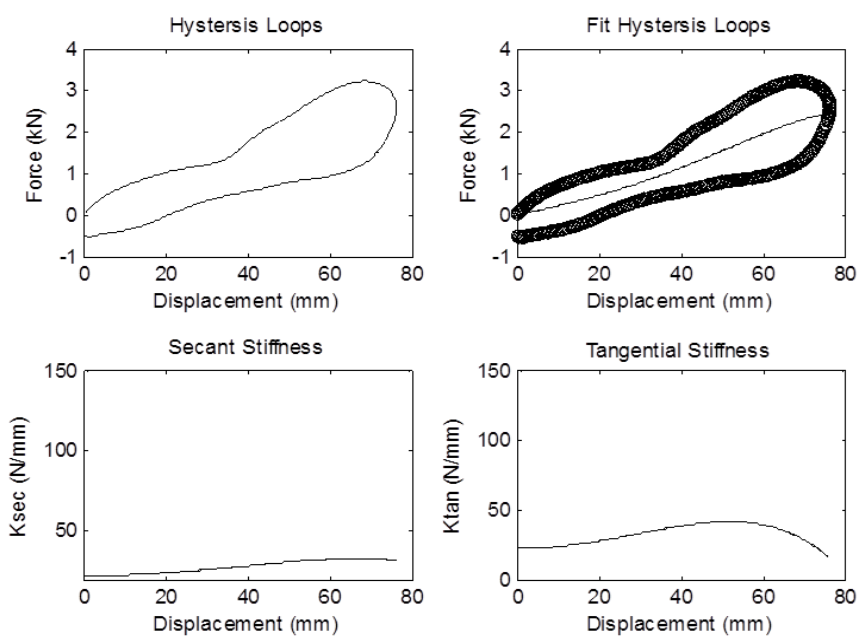

Figure 3.17 Bearing B1-11 hysteresis loop (400%t_r), fitted 5th order polynomial, secant stiffness and tangent stiffness.

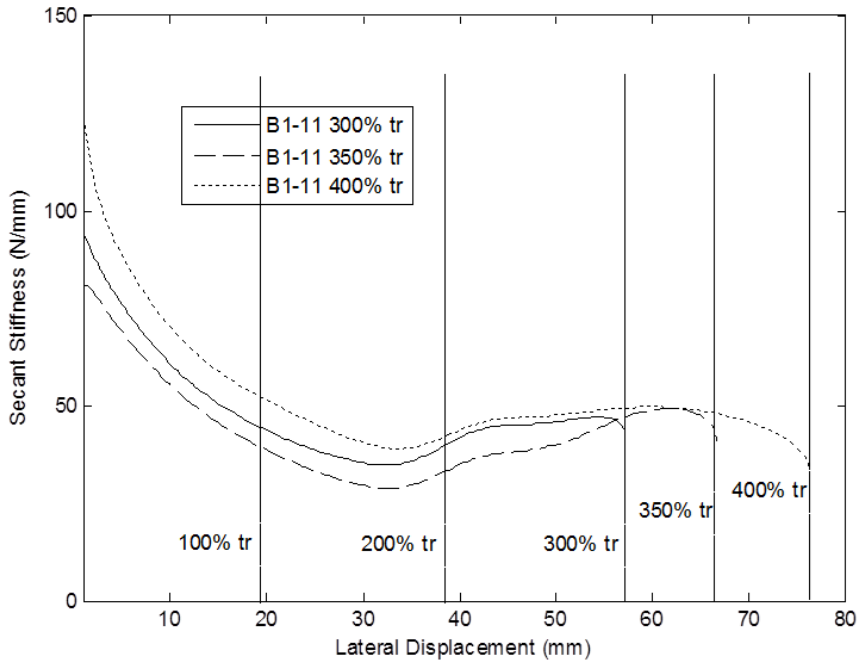

Figure 3.18 Numerically evaluated lateral secant stiffness (bearing B1-11) for three displacement amplitudes.

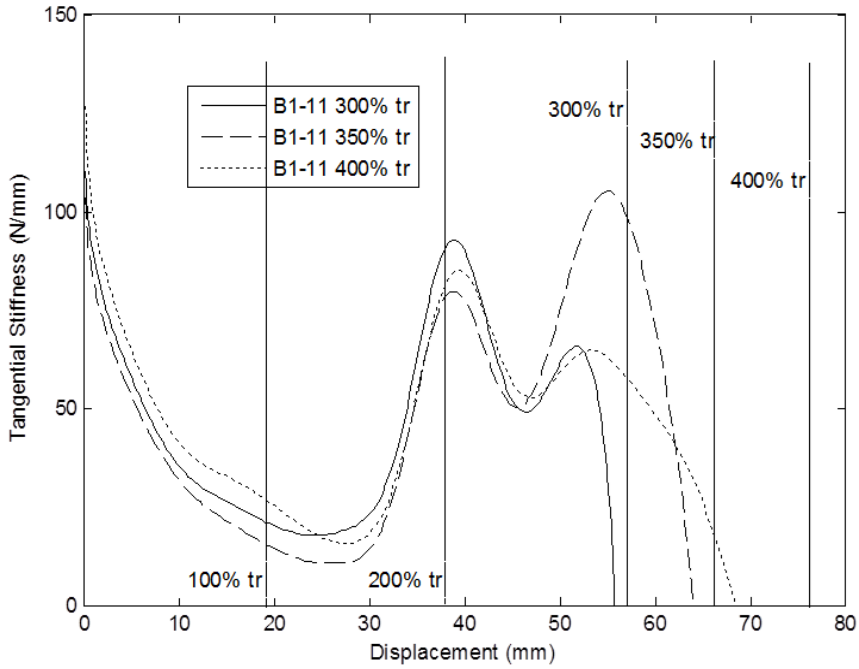

Figure 3.19 Numerically evaluated lateral tangential stiffness (bearing B1-11) for three displacement amplitudes. Note: The lateral tangential stiffness is calculated to the maximum force value.

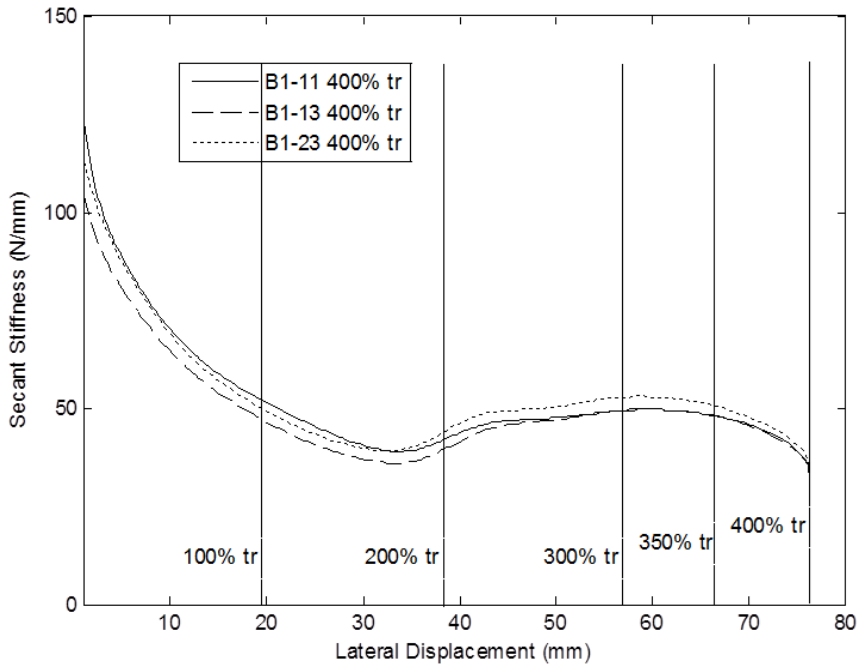

Figure 3.20 Numerically evaluated lateral secant stiffness (400%t_r).

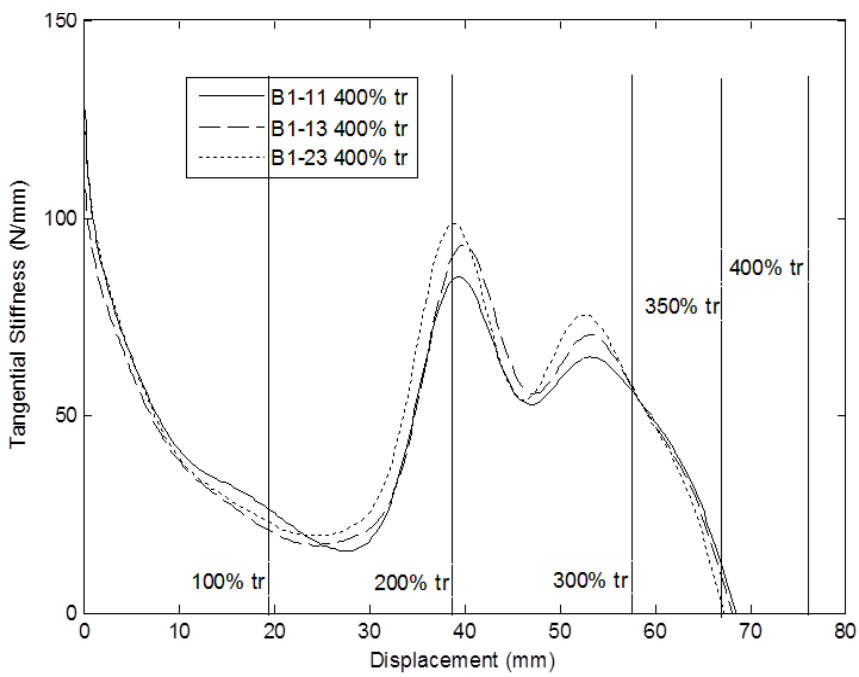

Figure 3.21 Numerically evaluated lateral tangential stiffness (400%t_r). Note: The lateral tangential stiffness is calculated to the maximum force value.

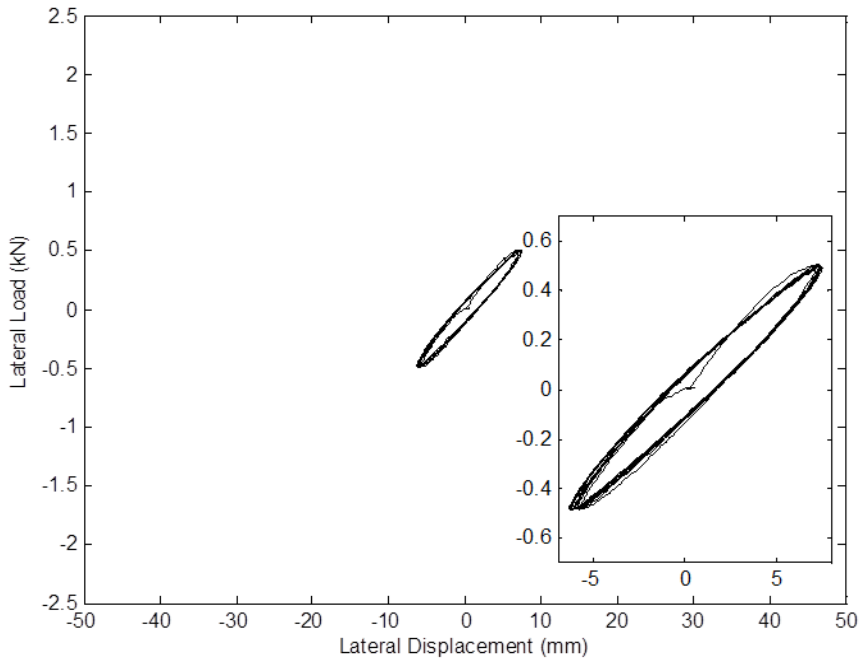

Figure 3.22 Hysteresis loops for service wind loading conditions (q=0.31kPa).

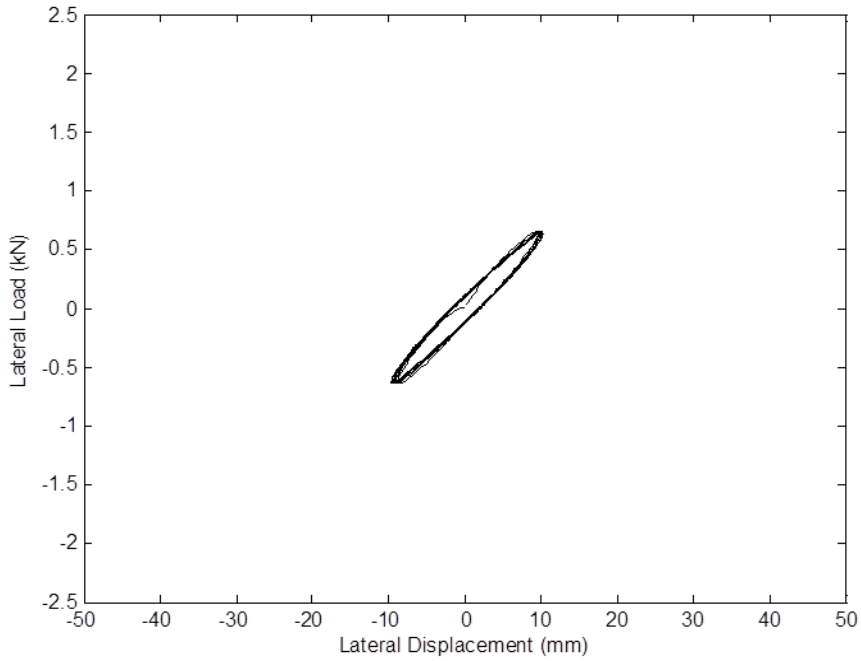

Figure 3.23 Hysteresis loops for design wind loading conditions (q=0.4kPa).

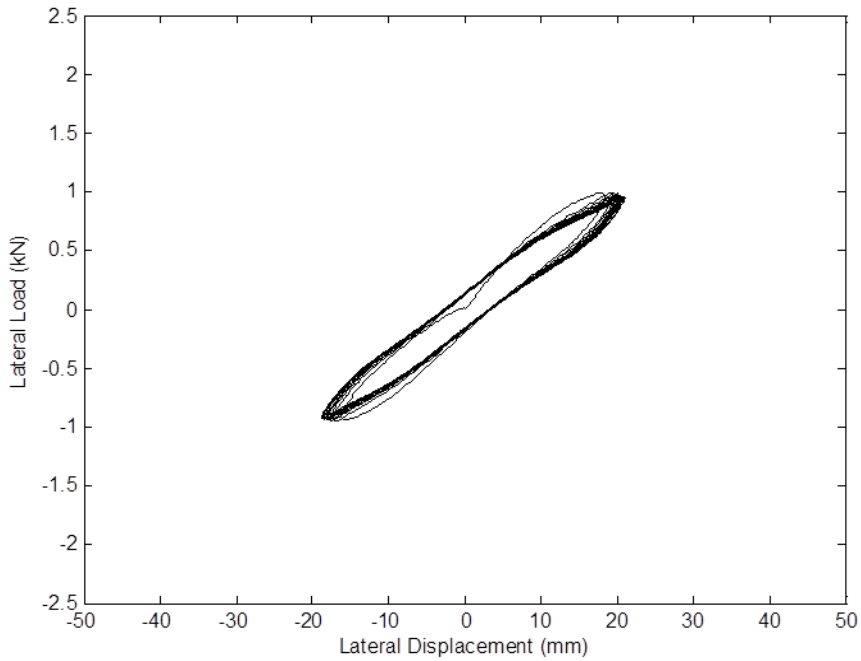

Figure 3.24 Hysteresis loops for maximum wind loading conditions (q=0.6kPa).

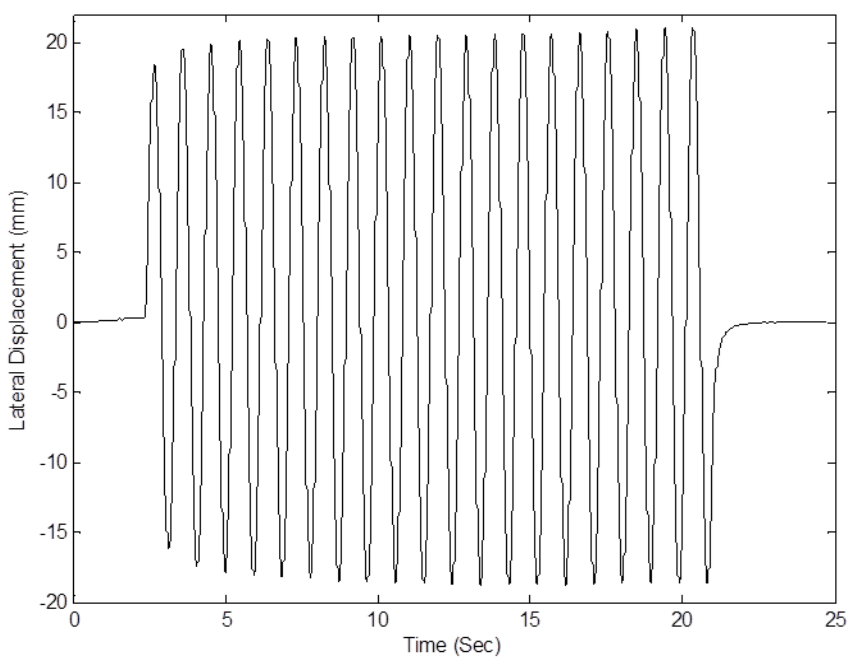

Figure 3.25 Displacement time history of the maximum wind loading test (q=0.6kPa).

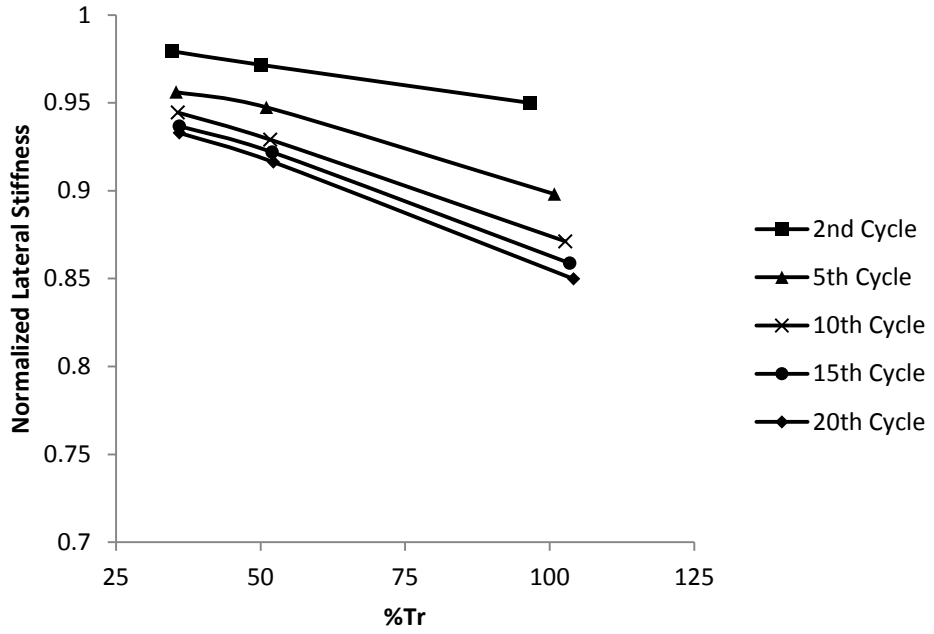

Figure 3.26 Normalized lateral stiffness versus $\%t_r$. Note: The vertical distance between lines indicates the change in stiffness.

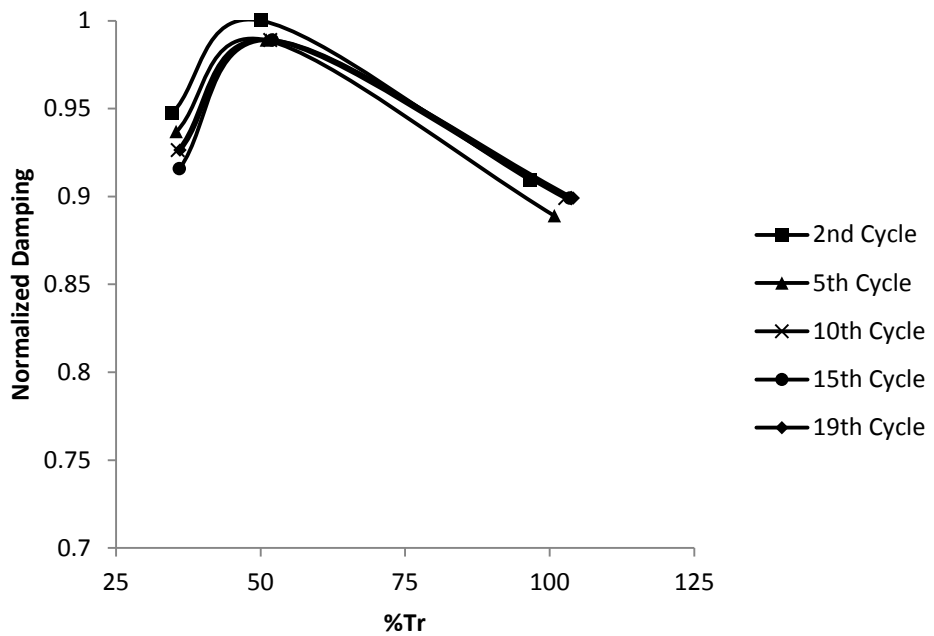

Figure 3.27 Normalized damping versus $\%t_r$. Note: The vertical distance between lines indicates the change in damping.

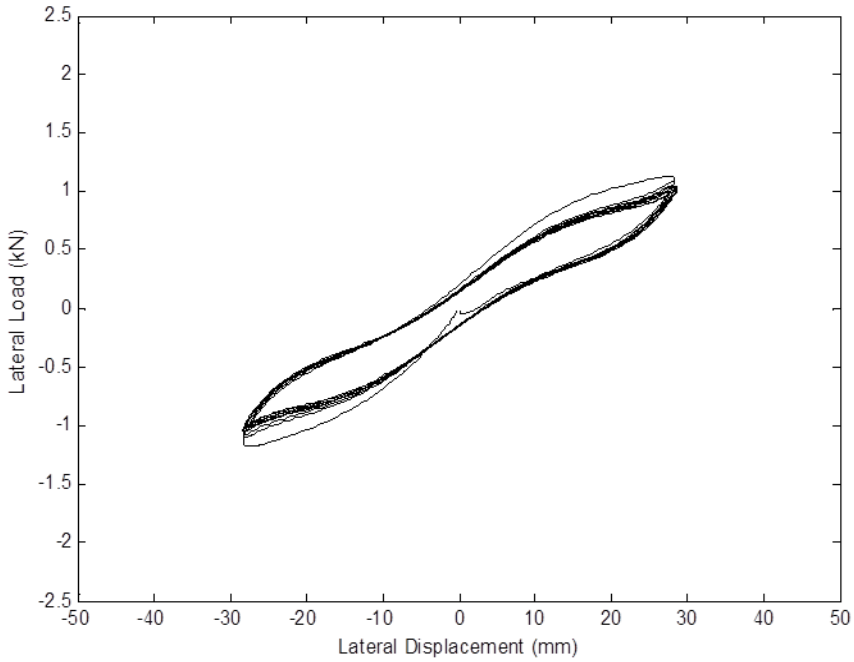

Figure 3.28 Hysteresis loops (bearing B4-12), fatigue testing.

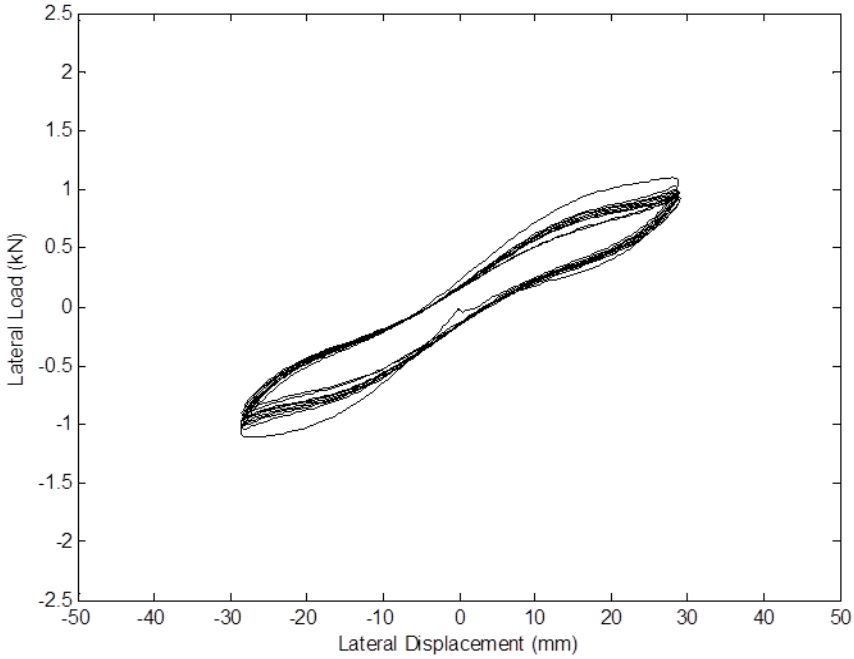

Figure 3.29 Hysteresis loops (bearing B2-21), fatigue testing.

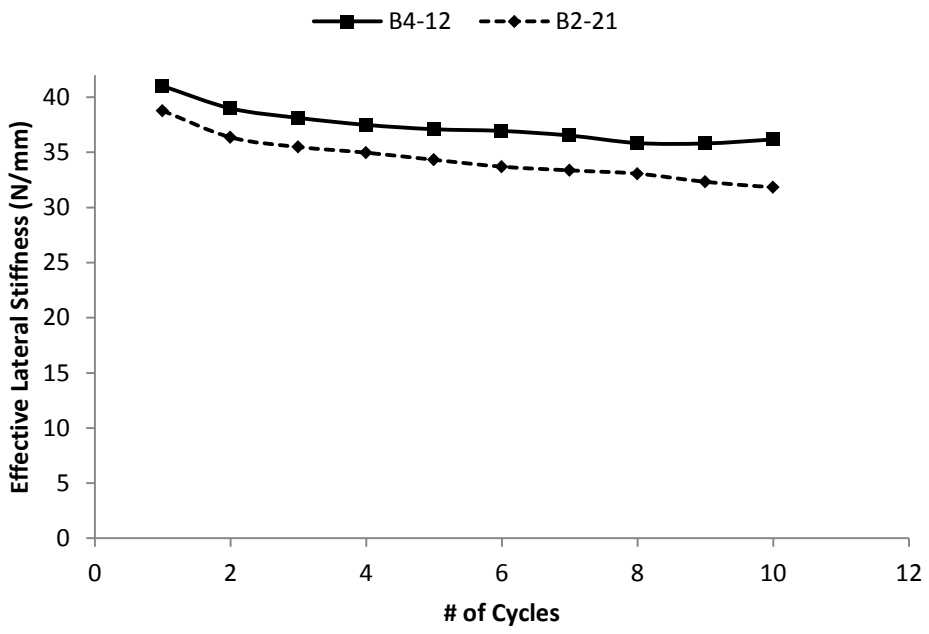

Figure 3.30 Graphical depiction of the fatigue testing stiffness results.

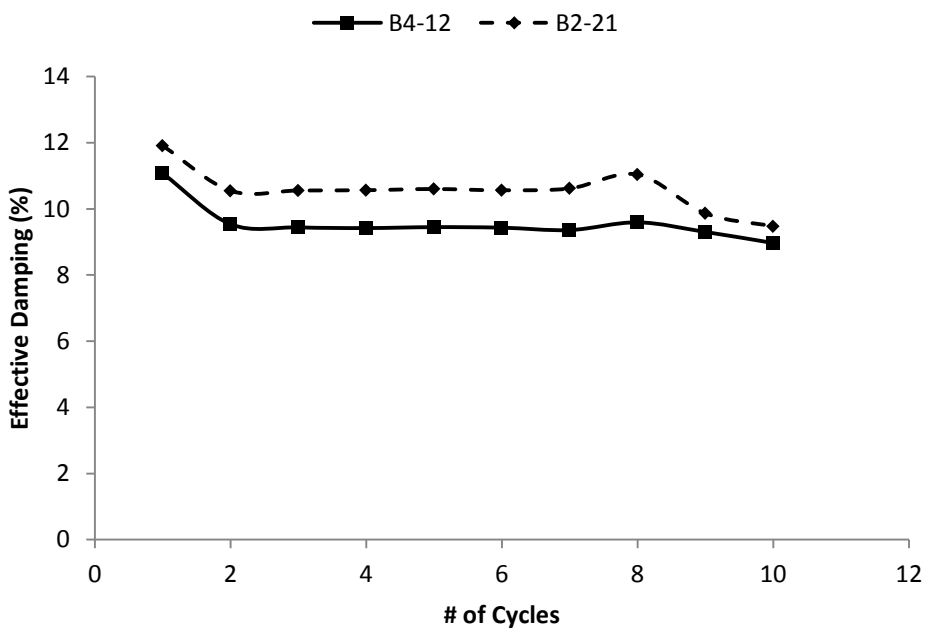

Figure 3.31 Graphical depiction of the fatigue testing damping results.

Chapter 4. Stable Unbonded Fibre Reinforced Elastomeric Isolator (SU-FREI) Models

4.1 Introduction

Several mathematical models have been employed to describe the nonlinear force-displacement behaviour of SU-FREI bearings. The variation in complexity of these models is significant, ranging from the common three parameter bilinear model, described by Naiem and Kelly (1999) to the ten parameter rate and amplitude dependent stiffness and damping model proposed by Hwang et al. (2002). In addition to these two models, a modified Bouc-Wen model (Love et al. 2011) and a nonlinear stiffness, constant equivalent viscous damping model, referred to as the Backbone Curve model (Toopchi-Nezhad 2008), have also been used to simulate the response behaviour of SU-FREI bearings.

The bilinear model (BLM) and the backbone curve model (BCM) are selected in this study to simulate the hysteretic behaviour of the SU-FREI bearings. A detailed description of both models is presented in this chapter. The required model parameters are subsequently determined using the lateral load-displacement hysteresis loops presented in Chapter 3. For evaluation purposes, the response of the bearings, generated from the calibrated models, is compared to the experimental results. It should be noted that both models assume the SU-FREI bearings are rigid in the vertical direction.

4.2 Bilinear Model (BLM)

The bilinear model is based on three parameters k_1, k_2 and q, which are established from the unscragged lateral force-displacement hysteresis data. A graphical representation of the variables is shown in Figure 4.1. The post yield stiffness, k_2, can be estimated from the tangent stiffness at zero displacement, whereas q, the characteristic strength, can be calculated by averaging the absolute values of q_1 and q_2, which are where the hysteresis loop crosses the positive and negative vertical (force) axis (Naiem and Kelly 1999). The elastic stiffness, k_1, which is more difficult to determine, is discussed later.

The effective secant lateral stiffness of an individual bearing, k_{bi}, is defined by Equation 4.1 for a lateral displacement amplitude $v_b \geq v_{b,y}$, where $v_{b,y}$ is the yield displacement, described by Equation 4.2.

$$k_{bi}(t) = k_2 + \frac{q}{v_b(t)} \tag{4.1}$$

$$v_{b,y} = \frac{q}{k_1 - k_2} \tag{4.2}$$

The effective equivalent viscous damping ratio of the bearing, $\zeta_{eff}(t)$, is defined by Equation 4.3,

$$\zeta_{eff}(t) = \frac{4q\left(v_b(t) - v_{b,y}\right)}{2\pi k_{bi}(t) v_b^2(t)} \tag{4.3}$$

where the numerator is the energy dissipation per cycle (area within the hysteresis loop) and the denominator is proportional to the restoring energy.

Introducing two new dimensionless parameters, one based on displacement and the other on the characteristic strength, defined in Equation 4.4 and Equation 4.5, respectively, Equation 4.3 can be expressed in the form of Equation 4.6.

$$y(t) = v_b(t)/v_{b,y} \tag{4.4}$$

$$\alpha = q/k_2 v_{b,y} \tag{4.5}$$

$$\zeta_{eff}(t) = \frac{2\alpha}{\pi}\frac{y(t)-1}{(y(t)+\alpha)y(t)}, for\ y(t) > 1 \tag{4.6}$$

For a constant α it can be shown that the maximum damping ratio, $\zeta_{eff,max}$, occurs at $y_{\zeta_{eff,max}}$, defined by Equation 4.7 (Naiem and Kelly 1999).

$$y_{\zeta_{eff,max}} = 1 + (1+\alpha)^{\frac{1}{2}} \tag{4.7}$$

By substituting Equation 4.7 into Equation 4.6 the maximum value of the damping ratio, $\zeta_{eff,max}$, can be expressed as

$$\zeta_{eff,max} = \frac{2\alpha}{\pi}\frac{1}{2(1+\alpha)^{\frac{1}{2}} + (2+\alpha)} \tag{4.8}$$

From Equation 4.2, α can be expressed in terms of $k_1$and k_2.

$$\alpha = \frac{k_1 - k_2}{k_2} \qquad 4.9$$

Therefore, once k_2 and $\zeta_{eff,max}$ are determined from experimental data, the value of k_1 can be calculated.

$$k_1 = (1 + \alpha)k_2 \qquad 4.10$$

4.3 Backbone Curve Model (BCM)

The backbone curve model involves fitting a 5th order polynomial function to experimentally obtained lateral force-displacement response data. The lateral force in an individual bearing "i" can be expressed as

$$f_{b,i}\,(t) = f_{sb,i}\,(t) + f_{db,i}\,(t) \qquad 4.11$$

where $f_{sb,i}$ represents the stiffness force and $f_{db,i}$ the damping force. The stiffness force, $f_{sb,i}\,(t)$, of an individual bearing can be expressed as

$$f_{sb,i}\,(t) = k_{b,i}\big(v_b(t)\big)v_b(t) \qquad 4.12$$

where $k_{b,i}\big(v_b(t)\big)$ is the effective lateral (secant) stiffness of the bearing as a function of the displacement, $v_b(t)$. The effective lateral stiffness, $k_{b,i}\big(v_b(t)\big)$, can be modeled as a polynomial of order 4.

$$k_{b,i}\big(v_b(t)\big) = b_o + b_1 v_b(t) + b_2 v_b^2(t) + b_3 v_b^3(t) + b_4 v_b^4(t) \qquad 4.13$$

The five parameters, b_0 to b_4, are determined by a least squares fit to the experimentally obtained lateral load displacement data. By taking the first derivative of the backbone curve, the tangential stiffness can be evaluated to determine if positive incremental lateral load carrying capacity is maintained. Equation 4.14 gives the first derivative of the backbone curve.

$$k_{tb,i}\big(v_b(t)\big) = \frac{df_{sb,i}\,(t)}{dv_b(t)} \qquad 4.14$$

$$= b_o + 2b_1 v_b(t) + 3b_2 v_b^2(t) + 4b_3 v_b^3(t) + 5b_4 v_b^4(t)$$

The equivalent viscous damping force of the hysteresis model, $f_{db,i}(t)$, is a Rayleigh damping idealization that models the energy dissipation of the individual bearings and is expressed as

$$f_{db,i}(t) = C_{bi}(t)\dot{v}_b(t) \qquad 4.15$$

where the damping coefficient,$C_{bi}(t)$, at any instant in time is calculated by

$$C_{bi}(t) = 2\zeta_{eff}\sqrt{\frac{k_{b,i}(v_b(t))P}{g}} \qquad 4.16$$

where P, is the applied load on an individual bearing, g, is the acceleration due to gravity, and ζ_{eff} is a constant effective damping value (Toopchi-Nezhad et al. 2008c).

4.4 Fitting/Calibration of Models

4.4.1 Bi-Linear

Figure 4.2 shows a visual representation of the k_1 and k_2 values used in the model. The values of k_1, k_2 and q for a total of seven amplitudes, ranging from 25%t_r to 250%t_r maximum displacement amplitude, are listed in Table 4-1. The value of k_2 was calculated by completing a least squares fit to ±75% maximum displacement amplitude of the data. This amplitude range is in close agreement to that suggested by Naiem and Kelly (1999). The value of q was determined by taking the average magnitude of force at zero displacement. Finally, k_1 was calculated as $(1+\alpha)k_2$, where α is calculated based on an averaged experimentally evaluated damping ratio value of 8%.

4.4.2 Backbone Curve

A backbone curve is developed by carrying out a least squares fit to the lateral load-displacement unscragged hysteresis loop data. It should be noted that the least squares fit is to all unscragged hysteresis loops up to and including the displacement amplitude under consideration. As an example, the backbone curve corresponding to 100%t_r would be evaluated using a least-squares fit to the unscragged hysteresis loops at 100%t_r, 75%t_r, 50%t_r and 25%t_r.

The damping ratio used in the model is a constant value selected based upon the effective damping evaluated from lateral cyclic test results. The selected damping value used for the model was 8%, which is an average of the effective

damping values determined in the 100%t_r to 250%t_r displacement range. This displacement range covers the expected displacement amplitudes of the bearing during shake table testing discussed in Chapter 5. Figure 4.3 shows the fitted backbone curves for the unscragged hysteresis data, while Table 4-2 lists the backbone curve coefficients for each lateral displacement amplitude.

4.5 Modelled Hysteresis Loops

The simulated hysteresis loops, generated using the bilinear model and backbone curve model are presented in Figure 4.4 along with the experimentally measured lateral load displacement hysteresis loops at 100%t_r. The displacement time history used to generate the simulated and experimental hysteresis loops is shown in Figure 4.5. The distinct shape of the hysteresis loop generated using the bilinear model, as a result of the two stiffness values k_1 and k_2, can be observed in Figure 4.4(a). At 100%t_r displacement amplitude, the effective stiffness predicted by the bilinear model is 11% higher than the value evaluated from the experimentally measured lateral load displacement hysteresis loop shown in Figure 4.4(c). Figure 4.4(b) shows the hysteresis loop generated using the backbone curve model. The predicted effective lateral stiffness value of the backbone curve model at 100%t_r displacement amplitude is approximately 43.1N/mm, which is in excellent agreement with the value obtained from experimental test results.

4.6 Discussions and Conclusions

Two simple models were selected and calibrated to experimental lateral load-displacement results. The first model was a 3 parameter bilinear model, while the second model was a 6 parameter backbone curve model introduced by Toopchi-Nezhad et al. (2008c). The models were used to generate hysteresis loops using measured displacement time history data. The generated hysteresis loops were compared to experimentally measured data at 100%t_r displacement amplitude. Implementation of these models and further evaluation is discussed in Chapter 6.

Table 4-1 Bilinear model parameter values at respective displacement amplitude.

Displacement Amplitude	q (N)	k_2 (N/mm)	k_1 (N/mm)
25%t_r (≈4.75mm)	66.9	71.6	118.7
50%t_r (≈9.50mm)	103.0	60.7	100.6
75%t_r (≈14.25mm)	114.9	51.9	86.1
100%t_r (≈19.00mm)	122.5	44.9	74.4
150%t_r (≈28.50mm)	140.6	35.9	59.5
200%t_r (≈38.00mm)	151.8	31.6	52.4
250%t_r (≈47.50mm)	175.4	32.7	54.2

Table 4-2 Backbone curve model coefficients at respective displacement amplitude.

Displacement Amplitude	b_0 (N/mm)	b_1 (N/mm^2)	b_2 (N/mm^3)	b_3 (N/mm^4)	b_4 (N/mm^5)
25%t_r (≈4.75mm)	7.30E+01	7.13E-01	-1.55E-01	-2.39E-02	3.42E-03
50%t_r (≈9.50mm)	7.02E+01	-1.55E-01	-2.71E-01	4.57E-04	1.78E-03
75%t_r (≈14.25mm)	6.38E+01	-1.77E-01	-1.15E-01	3.52E-04	2.63E-04
100%t_r (≈19.00mm)	5.94E+01	-1.56E-01	-7.81E-02	2.54E-04	1.01E-04
150%t_r (≈28.50mm)	5.62E+01	-9.71E-02	-6.08E-02	8.45E-05	4.33E-05
200%t_r (≈38.00mm)	5.25E+01	-9.84E-02	-4.84E-02	8.94E-05	2.54E-05
250%t_r (≈47.50mm)	4.49E+01	-4.10E-02	-2.79E-02	3.74E-05	1.16E-05

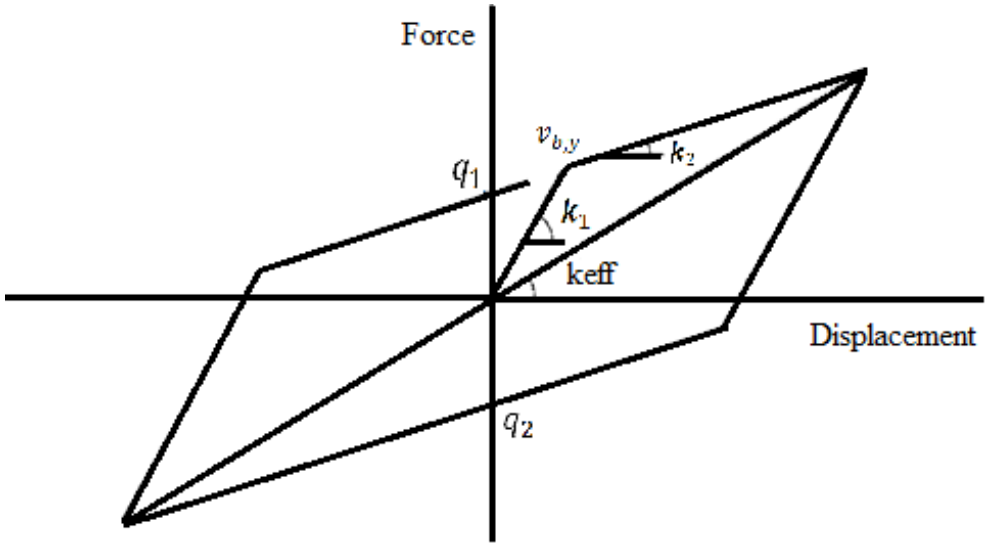

Figure 4.1 Bilinear idealization with visual representation of parameters.

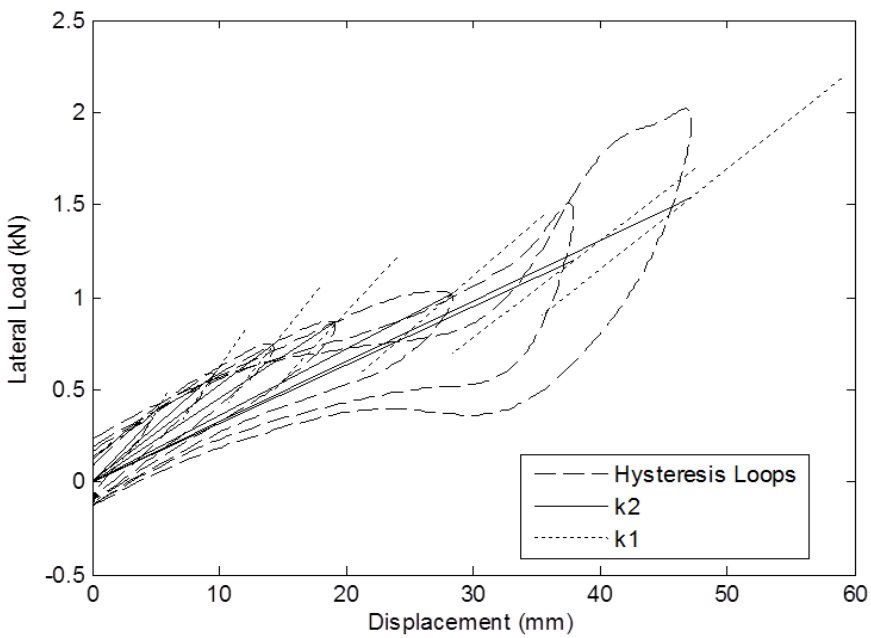

Figure 4.2 Visual representation of k_1 and k_2 of the bilinear model.

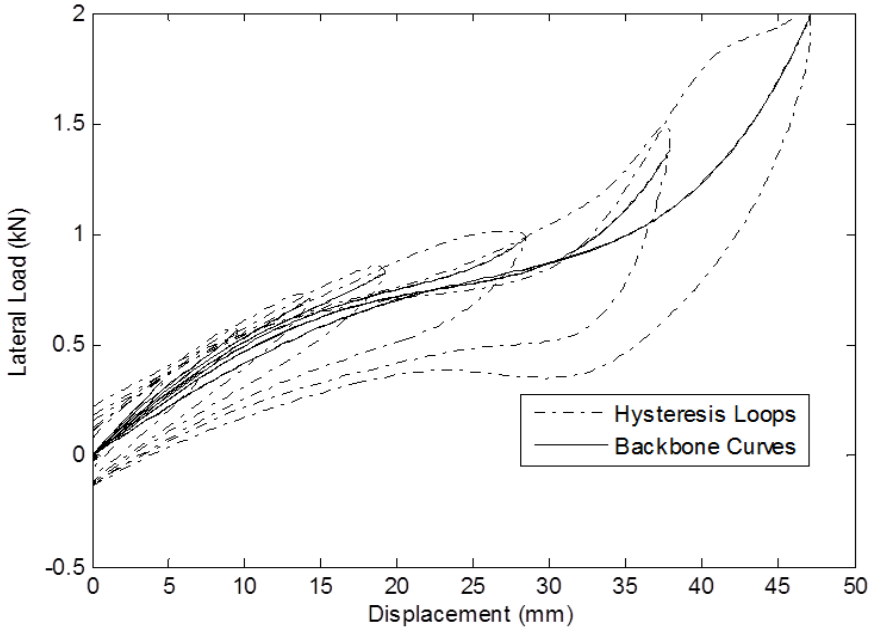

Figure 4.3 Backbone curves fit to the unscragged hysteresis loops.

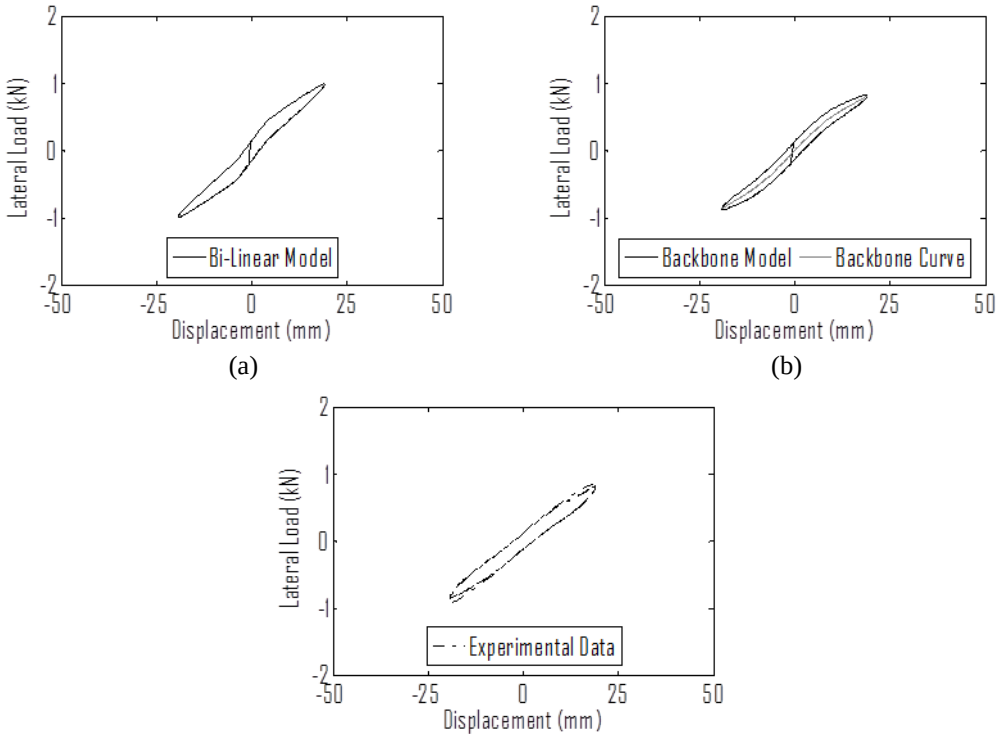

Figure 4.4 Hysteresis loops (100%t_r) for (a) bilinear model, (b) backbone curve model and (c) experimentally measured.

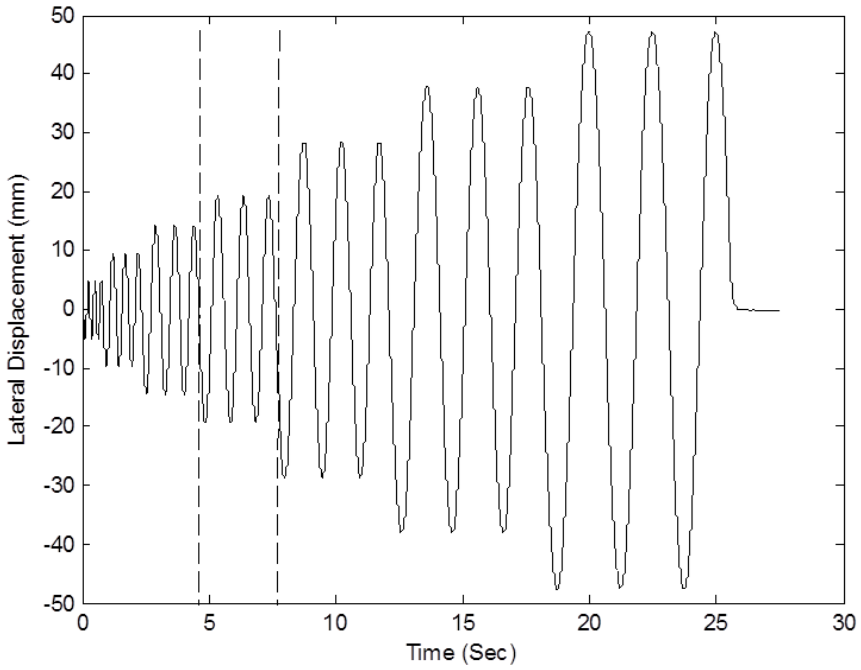

Figure 4.5 Lateral displacement time history signal used for model input.

Chapter 5. Shake Table Tests

5.1 Introduction

Shake table testing provides a direct way to simulate earthquake ground motion effects on a structure. As a result, shake table tests are often used to study the behaviour and evaluate the performance of base isolation systems. This chapter describes a series of shake table tests conducted on a quarter scale SU-FREI base isolated structure.

Details of the quarter scale two story structure are first presented followed by the isolation system, test setup and instrumentation, test procedures and input earthquakes. Next, experimental results from shake table tests on the SU-FREI base isolated structure are introduced and discussed. Test results from the shake table study are used to investigate the behaviour of a quarter scale SU-FREI base isolated structure. Efficiency of the SU-FREI isolation system is subsequently evaluated by comparing time history analyses (THA) of a fixed base (FB) model of the structure subjected to the recorded shake table acceleration response time history signals to experimentally obtained base isolation system test results. Finally, conclusions from this shake table test program are presented.

5.2 Model Scale Base Isolated (BI) Structure

The test structure used in this study is a modified version of the structure used by Toopchi-Nezhad et al. (2009a). A photograph of the quarter scale two

storey, single bay moment resisting steel test structure is shown in Figure 5.1. The plan dimensions of the structure are 1500mm by 1400mm with a height of 1679mm (see Figure 5.2). The columns are hollow square sections (HSS 64x64x6.4mm) and the beams are built up sections consisting of a square hollow section (HSS 51x51x6.4mm) welded to the top of a rectangular hollow section (HSS 76x51x6.4mm). The floor system of the structure consists of three precast concrete floor slabs. To satisfy dynamic similitude (Harris and Sabnis 1999) additional mass is added using four steel plates bolted to each floor slab (12 plates in total) as shown in Figure 5.3. The total weight of the structure is 32.1kN. The experimentally measured natural fundamental period (frequency) of the fixed base structure, which is discussed in greater detail in Section 5.6, is 0.102s (9.8Hz).

5.3 Isolation System

The isolation system consists of a total of four SU-FREI bearings. A single bearing is placed under each of the four columns of the structure. The lateral stiffness of the isolation system at low amplitude displacements (25%t_r) is expected to be approximately 300N/mm based on the results of the individual bearing stiffness values presented in Chapter 3. The properties of the bearings are amplitude dependent, therefore, the fundamental natural period (frequency) of the base isolated structure (isolation mode) is estimated to range between 0.614s (1.63Hz) and 0.990s (1.01Hz) assuming the base isolated structure can be modeled as a single degree of freedom (SDOF) system.

Modal analysis was carried out to estimate the three natural periods (frequencies) and corresponding mode shapes. It is recognized that modal analysis is not applicable to non-classically damped structures; therefore, the calculated values should be treated as approximate values. Table 5-1 summarizes the estimated natural periods (frequencies) of the isolated structure determined using modal analysis. The corresponding mode shapes are shown in Figure 5.4. It can be observed that the structure essentially responds as a rigid body in the first mode and deformation occurs at the isolator level. As a result, the calculated natural period (frequency) for the base isolation mode (first mode) is in good agreement with that obtained using a SDOF model approach. From Figure 5.4 it can be observed that the second and third modes involve deformation of both the isolation system and the structure.

5.4 Setup and Instrumentation

The unidirectional shake table used in this study is shown Figure 5.1 Instrumentation used to obtain the data is shown in Figure 5.2 and Figure 5.3. A total of six displacement transducers (string potentiometers) were used to measure displacements of the structure. A displacement transducer was connected at each floor level of the structure and to the table. These four displacement transducers recorded absolute displacements. In addition, the base floor level had two displacement transducers connected near the columns (see Figure 5.2), which were used to calculate both rotational motion and bearing deformation during testing. A unidirectional accelerometer was also attached at each floor level and to

the shake table in order to measure lateral in plane accelerations. In addition, two bi-directional accelerometers were attached at the roof level to measure out of plane and vertical accelerations. Finally, strain gauges were placed on two columns, diagonal to one another, to record strain at the base of the column. All measurements were recorded at 200Hz and filtered at 50Hz using a 16-channel data acquisition system. The response of the base isolated structure and bearings was captured by three video cameras. The first camera was attached to the shake table and recorded the motion of a single bearing. A second camera was attached to the structure itself and recorded the motion of a second bearing. The third camera was used to record the motion of the entire base isolated structure. The locations of camera 1 and camera 2 are shown in Figure 5.2.

5.5 Free Vibration Tests

5.5.1 Fixed Base Structure

Free vibration testing was performed on the structure in a fixed base configuration. From free vibration test results, shown in Table 5-2, the periods of the first and second mode of the fixed based structure were found to be 0.102 and 0.035 seconds, respectively, which match the theoretically calculated values. The logarithmic decrement method (Equation 5.1) was used to estimate the damping ratio (Chopra 2007),

$$\zeta = \frac{1}{2\pi j}\ln\left(\frac{\ddot{u}_i}{\ddot{u}_{i+1}}\right) \qquad 5.1$$

where j is the number of cycles considered, $\ddot{u}_i$ is the peak acceleration in the first cycle and $\ddot{u}_{i+1}$ is the peak acceleration of the final cycle. The measured damping ratio of the structure was found to be approximately 0.6%

5.5.2 Base Isolated Structure

Free vibration testing was also performed on the isolated structure for each new set of bearings. The average period was approximately 0.44 seconds for all bearing sets, while the damping ratio was estimated to be 8.6%, 7.2% and 8.6%, respectively, for the bearing sets corresponding to El Centro-t, Loma Prieta-t and Chile-t tests. The results are presented in Table 5-2. The period of the base isolated structure obtained from the experimental tests is approximately 33% lower than the theoretically obtained solution of 0.66 seconds, which was evaluated using the lateral stiffness corresponding to 25%t_r. This discrepancy in the natural period is expected as the free vibration test displacement amplitudes were substantially lower than 25%t_r.

5.6 Input Earthquakes

Three separate seismic strong ground motions were used in this shake table testing program, El Centro (1940), Chile (2010) and Loma Prieta (1989), respectively. The ground motion properties of the original earthquakes are given in Table 5-3. The peak ground acceleration (PGA) of each earthquake was scaled from 0.1g to 0.5g by 0.1g increments to obtain a range of records that would sufficiently envelop earthquakes in both eastern and western Canada. To satisfy

dynamic similitude requirements, the original records were compressed by a factor of two, corresponding to the square root of the length scale, with respect to time. The original time history signals of El Centro are shown in Figure 5.5. The 5% damped acceleration spectrum of the original record, scaled to 0.3g PGA, is shown in Figure 5.6a. Figure 5.6b shows the 0.3g PGA shake table generated 5% damped acceleration spectrum. To differentiate between the earthquake records, the original scaled records end in '-o' while the input earthquakes generated by the shake table (measured table response accelerations) end in '-t' and are referred to as the scaled and input earthquake records, respectively.

Figure 5.7 and Figure 5.9 show the original time histories of the Loma Prieta and Chile record, respectively. The 5% damped acceleration spectra of the original Loma Prieta and Chile records, scaled to 0.3g PGA and corresponding table generated records are shown in Figure 5.8 and Figure 5.10, respectively. It can be observed from the figures that in the base isolated frequency range, the table-generated spectra values meet or exceed the original scaled spectra values.

5.7 Shake Table Testing Program

A total of 24 shake table tests were completed using the three input earthquake records. Four unscragged bearings were used for each of the three earthquake record test series. An outline of the testing sequence is provided in Table 5-4. The first five tests for each input earthquake, which correspond to the five PGA amplitudes, had the bearings placed in a 90° orientation as shown in Figure 5.11. Upon completion of the Chile-t tests, grit pads were placed on the

bearing contact surfaces to increase the friction coefficient as shown in Figure 5.12. The bearings used for the first Loma Prieta-t test series were rotated 90° and retested under the five PGA amplitudes of the Loma Prieta-t record. Testing concluded with the Loma Prieta-t bearings rotated by 45°, with the grit pads present as shown in Figure 5.13. The grit pads had an adhesive surface on one side, while the surface in contact with the bearing was similar to that of low grit sand paper.

During each test series, the bearings were examined in-situ after the 0.1g and 0.2g tests. For higher amplitude tests, the structure was raised off the bearings, each bearing was removed, and a thorough inspection was carried out.

5.8 Shake Table Test Results

5.8.1 Data Processing

The displacements and accelerations at each floor level were used to calculate the dynamic response parameters of the base isolated structure. Relative displacements of each floor level were calculated by subtracting the table displacement from each corresponding absolute floor displacement. Inertia forces at each floor level were computed by multiplying the measured floor accelerations by the corresponding floor mass. In turn, the inertia forces of the middle and roof level were summed to determine the base shear (V_b) of the structure. Adding the inertia force of the base floor with that of the base shear resulted in the total shear

force in the bearings. The base moment (M_b) was calculated by summing the inertia forces multiplied by their respected heights above the isolators.

5.8.2 Bearing Response

The peak response values obtained from shake table test results corresponding to the three input earthquake records with the SU-FREI bearings in the 90° orientation are presented in Table 5-5. Examining the displacements of the bearings during testing, Figure 5.14 displays the displacement time history response of the El Centro 0.5g PGA record. Shown in Table 5-5, the bearings experienced a displacement amplitude of 205%t_r. This displacement amplitude implies, from the results of Chapter 3, that the bearings initially vertical surfaces experienced full vertical facial contact. The photograph in Figure 5.15 confirms full vertical facial contact, displaying the peak rollover deformation experienced by the bearings in the isolation system.

Due to the high bearing displacement amplitude, it is prudent to determine if the bearings maintained stability throughout testing. Figure 5.16 displays the hysteresis loops obtained from El Centro-t tests at PGA values of 0.1, 0.3 and 0.5g. Examination of the hysteresis loops corresponding to the three PGA values indicates that the bearings remained stable as they maintained positive incremental load carrying capacity throughout the duration of each test.

Figure 5.17 displays the lateral displacement history of the bearings during the 0.5g PGA Loma Prieta-t input record. From Figure 5.17 and Table 5-5, the peak displacement response value is found to be 311%t_r. The rollover

deformation of the bearing at 311%t_r is shown in Figure 5.18, displaying significant rollover beyond full vertical facial contact. The hysteresis loops corresponding to 0.1, 0.3 and 0.5g PGA Loma Prieta-t input records are presented in Figure 5.19. It can be observed that the bearings exhibited stable rollover behaviour as they maintained positive incremental load carrying capacity.

The bearing lateral displacement time history corresponding to the Chile-t input record at 0.5g PGA is shown in Figure 5.20. From Table 5-5, it is found that the bearings reached a peak displacement amplitude of 175%t_r. A photograph of the peak deformation experienced by the bearings is shown in Figure 5.21, confirming that the bearings used for the Chile-t record testing never made full vertical facial contact. The bearing hysteresis loops, see Figure 5.22, show that the bearings remained stable over all test amplitudes.

All bearings remained stable during shake table tests, confirming results from rollout tests in Chapter 3, which showed the bearings can maintain stability up to a lateral displacement amplitude of 400%t_r.

The peak bearing displacement for all three input earthquakes with respect to PGA is presented in Figure 5.23. This plot shows that the lateral displacement increases with increasing PGA intensity. The Loma Prieta-t record experienced larger displacement amplitudes than El Centro-t and Chile-t, which can be attributed to the higher energy content at low frequencies producing higher accelerations within the base isolated range of the structure. The higher accelerations can be seen in the base isolated range of Loma Prieta-t's response

spectrum, Figure 5.8b, compared to the response spectra for El Centro-t and Chile-t, shown in Figure 5.6b and Figure 5.10b, respectively.

5.8.3 Structural Response

The peak structural response parameters determined from the experiments are presented in Table 5-5 and Table 5-6. The time history response of the normalized base shear, $\frac{V_b}{w}$, and normalized roof accelerations, $\frac{a_2}{g}$, are presented in Figure 5.24 to Figure 5.26 for all three 0.5g PGA input earthquake records

The peak response values of the base isolated structure presented in Table 5-5 have been plotted visually in Figure 5.27 with respect to PGA. From Figure 5.27, it can be observed that Loma Prieta-t produces the largest response values from the three input earthquakes considered. The drifts, Δ, accelerations, $\frac{a_0}{g}, \frac{a_2}{g}$, and normalized base shear, $\frac{v_b}{w}$, all increase rapidly beyond the 0.3g PGA level for Loma Prieta-t. It is postulated that increased stiffness that occurs in the isolation system as the bearings experience full vertical facial contact, as discussed in and shown in Chapter 3, is the primary cause of this increase.

Plotting the peak response values against the base floor acceleration provides additional insight into the behaviour of the isolation system, as shown in Figure 5.28. From the plots, it can be observed that the results are well correlated with each other for all tests. The strong correlation between test results shows that there were minor variations in the three isolation system properties. The observed relationship between x_0 and a_0 is a direct result of the nonlinear stiffness

characteristic of the SU-FREI isolation system. The value of x_0 increases at a more rapid rate between approximately 100%t_r and 200%t_r than a_0 as a result of the softening behaviour of the isolation system due to stable rollover behaviour. Another noteworthy result can be found by inspection of the plot of roof acceleration versus base acceleration. The data forms an approximately linear line with a near one to one ratio. This implies negligible amplification in acceleration along the height of the structure occurs. This relationship is a result of the structure responding as a rigid body.

Rigid body motion is also evident from the acceleration amplification envelops shown in Figure 5.29. The figure displays approximately vertical lines, showing constant acceleration along the height of the structure. The amplification envelops show that the peak accelerations are consistently lower than the ground acceleration. The roof accelerations are approximately 45%, 20% and 62% lower than the ground accelerations for the 0.5g PGA El Centro-t, Loma Prieta-t and Chile-t records, respectively. Chile-t produces the lowest structural accelerations from the 0.5g PGA input records, followed by El Centro-t and then Loma Prieta-t. Comparing the roof accelerations of 0.3g PGA, the reductions are approximately 55% for both El Centro-t and Chile-t and 26% for Loma Prieta-t.

To investigate the displacements and forces occurring on the structure, the lateral displacements, inertia forces, shear forces and overturning moments have been plotted along the height of the structure in Figure 5.30. The plots are based on 0.3g PGA results and show that Chile-t and El Centro-t produce near identical

levels of displacements and forces on the structure. Loma Prieta-t produced forces that were approximately 64% larger for the roof inertia force, 59% larger base shear and 60% larger base overturning moment than El Centro-t and Chile-t. These can be attributed to the larger spectral acceleration values (energy) at the base isolated period of the structure (see Figure 5.8). Despite larger forces occurring on the structure during the Loma Prieta-t earthquake, a maximum strain value of 70με was recorded from the strain gauges attached to the base of the columns of the structure. The strain level was 3.5% of the 2000με yield of the steel showing that the structure experienced negligible elastic deformations during testing.

5.8.4 Isolation System Characteristics

5.8.4.1 Period (Frequency)

The base isolated period of the system was determined by performing a fast Fourier transform (FFT) on the measured roof lateral accelerations. The frequencies at which the largest FFT peak values occurred are presented in Table 5-5. Figure 5.31 shows the lateral roof Fourier amplitude spectrum for El Centro at 0.1, 0.2, and 0.5g PGA. As the PGA level is increased, the peak Fourier amplitude shifts to a lower frequency, indicating a longer period. This shift in period is due to the increased displacements that occur at higher amplitude PGA events. The increased period is expected because as the displacement amplitudes increase, the stiffness of the bearing decreases, lengthening the period of the

isolated structure. Figure 5.32 and Figure 5.33 present FFT plots for Loma Prieta-t and Chile-t, respectively. The FFT analysis of Loma Prieta-t and Chile-t show the same trends as the El Centro-t record.

5.8.4.2 Out-of-plane Accelerations/Torsion

The peak transverse (out-of-plane) and vertical accelerations, obtained from the bi-directional accelerometers located on the roof of the structure, are listed in Table 5-6. The values indicate that the transverse accelerations are insignificant relative to the in plane motion of the structure. The measured torsional response of the base isolated structure is plotted in Figure 5.34. The plots show that torsional motion begins to increase rapidly past 200%t_r, when full vertical facial contact of the bearings occurs. The small torsional response motions can be attributed to small discrepancies in the bearing's stiffness values as well as the alignment of the centre of rigidity of the isolation system to the centre of mass of the structure. Another contributing factor related to the increase of torsional response upon full vertical facial contact is the instant that each bearing makes full vertical facial contact. It was shown in Chapter 3 that the full facial contact of the bearings is dependent on the total height of the bearing and thickness of rubber. Should small variations in the heights of the bearings be present, this could result in full vertical facial contact occurring at slightly different displacements for each individual bearing. Finally, the individual bearings comprising the isolation system may stiffen at slightly different rates.

5.8.4.3 Vertical Accelerations/Residual Slip

The peak vertical structural accelerations, summarized in Table 5-6, show a similar trend as that observed for the out of plane accelerations. The peak acceleration values slowly increase with increased PGA intensity, however, once full vertical facial contact is made, the peak acceleration value increases more rapidly. The highest peak vertical acceleration value recorded was 0.15g, which occurred during the 0.5g PGA Loma Prieta-t record. Large vertical accelerations are not desirable as they can lead to a reduction in the vertical force acting on the bearings, which can affect their dynamic properties. In addition, with decreased loading on the isolation system, the bearings are more likely to experience residual slip, resulting in re-centreing issues.

The residual slip experienced by the isolation system is presented in Table 5-6 and plotted visually in Figure 5.35. The slip is negligible up to approximately 200%t_r, the approximate full vertical facial contact displacement. As full facial contact is made, the peak residual slip value increases. As Loma Prieta-t was the only input earthquake to significantly deform the bearing beyond 200%t_r, its residual slip behaviour is examined in more detail. It is seen that at 0.5g PGA amplitude Loma Prieta-t, the residual slip is approximately 41%t_r.

5.8.4.4 Grit Pad Testing

In an effort to reduce the 41%t_r level of residual slip experienced by the Loma Prieta-t earthquake, the base isolated structure was retested with a rough ‘grit pad’ layer between the structure and the bearing, and between the bearing

and table. The grit pads were introduced to increase the level of friction between the bearing contact surfaces. The results of the grit pad tests are presented in Table 5-7 and Table 5-8. The corresponding peak response parameters are also plotted in Figure 5.36. From the results of the grit pad testing, a 66% reduction of residual slip was achieved with negligible effect on the response of the structure or displacement experienced by the bearings. Comparing the no grit paper peak response values to the grit paper peak response values for roof acceleration, base shear and over turning moment, the difference in peak values were found to be less than 10%. The vertical acceleration of the 0.5g PGA Loma Prieta-t record with grit paper was however, approximately 50% larger producing a vertical acceleration of 0.22g. Despite the higher vertical acceleration, the structure experienced less residual slip. Results from the increased frictional surface tests show that residual slip of the structure can be significantly reduced by increasing the bearing contact surface friction with negligible impact on the response behaviour of the base isolated structure.

5.8.5 45° Orientation Testing

To further investigate the SU-FREI base isolation system, 45° orientation (diagonal) testing was completed. Since the bearings used during the Loma Prieta-t input earthquake were scragged in both directions, they were selected for the 45° orientation study. The test results are presented in Table 5-7 and Table 5-8. The data is also plotted in Figure 5.36, along with the results from the previous Loma Prieta-t testing. Results from the diagonal experiments imply that the stiffness and

damping properties of the bearings in the 45° orientation are similar to those in the perpendicular direction, which is in agreement with findings by Toopchi-Nezhad et al. (2008b) and de Raaf (2009). The stiffness in the 45° orientation is slightly less, resulting in reduced roof accelerations and increased bearing lateral displacement amplitudes. The reduction in stiffness at the 45° orientation is attributed to both the orientation of the bearing and scragging incurred from previous tests. Although diagonal tests were completed with the grit pads placed between the bearings contact surfaces, the residual slip was approximately equal to the results of the 90° orientation tests without the grit pads. This implies that the bearing may be more susceptible to residual slip when excited in the diagonal direction.

5.9 Damage Status of the Bearings

During shake table testing, the only bearing to experience damage was bearing B1-12. The bearing experienced a small delamination at the base layer of fibre and elastomer as shown in Figure 5.37. The delamination occurred during the 0.4g PGA Loma Prieta-t record while testing with the grit pads in the 90° orientation. The bearing had been subjected to eight earthquake records prior to delamination. The bearing continued to be used in the isolation system for all remaining Loma Prieta-t tests. Upon completion of the testing, the bearing showed no visibly new (increased) signs of damage.

5.10 Fixed Base (FB) Time History Analysis (THA) Results

To investigate the effectiveness of the isolation system, shake table test results are compared to numerically evaluated fixed base results. Time history analyses were carried out on a 5% damped model of the fixed base structure using the acceleration records obtained from the shake table tests for accurate comparisons. The model of the fixed base structure and time history analysis procedures are further described in Chapter 6.

5.10.1 Time History Response

Plots of base shear and roof acceleration response time histories for both the base isolated and fixed base structures are shown in Figure 5.38 to Figure 5.40 for the three 0.3g PGA earthquake records. The figures present experimental data from the base isolated structure tests along with the results from the fixed base structure time history analyses. The base isolated time histories show a substantial decrease in both parameters. It is also clear from the plots that the base isolated system has a reduced frequency by observing the duration of individual response cycles.

5.10.2 Peak Response

The peak 5% damped fixed base structure response data obtained from the analyses is presented in Table 5-9 along with the percentage reduction/increase of the parameters response compared to the tested base isolated structure. Results show that regardless of lateral displacement amplitude, the base isolated system is

capable of reducing the response of the structure. The system is most efficient between 150 and 200%t_r, because, at this normalized lateral displacement amplitude range, the bearings have minimal effective stiffness. For the El Centro-t 0.3g record, a 74% and 79% decrease in roof acceleration and base shear ratio, respectively, were obtained. For Loma Prieta-t at 0.3g, a 75% and 82% reduction in roof acceleration and base shear ratio were obtained. The largest response reduction was found for Chile-t, where the acceleration and base shear ratio were reduced by 87% and 89%, respectively.

The results of the fixed base to base isolated roof acceleration and base shear values are plotted with respect to PGA in Figure 5.41 and Figure 5.42, respectively. The plots give a graphical depiction of the efficiency ($\frac{FB}{BI}$) of the SU-FREI system for the two peak response parameters at the respected PGA levels. Examining the figures, the isolation system is most efficient for the Chile-t input earthquake and least efficient for the El Centro-t earthquake. This is due to the amplitudes of the response spectra accelerations at the period of the fixed base structure. For Chile-t the spectral acceleration corresponds to approximately 0.95g, whereas for El Centro-t the spectral acceleration is approximately 0.4g at the period of the fixed base structure (0.102s).

Figure 5.43 to Figure 5.45 show the maximum response pattern along the height of the structure for the three input earthquake records scaled to 0.3g PGA. The parameters shown are lateral displacement, inertia force, base shear ratio, and overturning moment, which are plotted with respect to the base floor of the test

structure. The figures show that there is significant change in both the shape and amplitude of the maximum response parameters, highlighting the ability of the base isolation system to mitigate the seismically induced displacements and forces.

5.11 Summary and Conclusions

A base isolated quarter-scaled model, single bay two-story structure was experimentally tested under a total of twenty-four earthquake records, ranging from 0.1g PGA to 0.5g PGA considering three seismic events. The response behaviour of the base isolated structure was subsequently examined. Test results showed that SU-FREI isolation systems are capable of significantly lengthening the period of the structure. This lengthened period results in reductions in both peak structural response and the entire time history response along the entire height of the structure. The base isolated structure experienced negligible relative displacements, indicating that it responded as a rigid body. This rigid body motion is highly desirable as it prevents inter-storey drift and damage within the structure itself. The structure experienced low strain levels remaining below 4% of the linear elastic limit of steel.

Although significant rollover deformations were experienced by the bearings during the higher PGA level tests, the bearings remained stable. The bearings were found to be extremely durable with only a single bearing experiencing minor delamination during testing. Repeated testing on the bearing

showed that the specimen remained stable and experienced no additional damage. Bearing displacement amplitudes beyond the full vertical facial contact amplitude produced a maximum vertical acceleration of 0.15g in the 0.5g PGA Loma Prieta-t record. Furthermore, significant residual slip, which is undesirable as it introduces residual displacements, was observed after the 0.5g PGA Loma Prieta-t earthquake record. Testing carried out with increased levels of friction at the bearing contact surfaces showed that residual slip could be reduced.

Testing of the SU-FREI isolation system with the bearings in a 45° orientation showed that the bearings behave similarly as excited in the perpendicular or parallel orientations. Testing also indicated that bearings excited in the 45° orientation may be more susceptible to residual slip.

Comparison of shake table results with results of a time history analysis of a 5% damped fixed base structure showed that the SU-FREI isolation system was capable of reducing seismic demand on the structure throughout the entire duration of the events selected. It was shown that the SU-FREI isolation system was able to reduce roof accelerations and base shears by a maximum value of 89% and 91%, respectively. The minimum levels of reductions were, respectively, 60% and 68% for roof acceleration and base shear. Overall, the isolation system was found to perform effectively.

Table 5-1 Modal analysis summary.

Parameter	Max./Min.	Mode 1	Mode 2	Mode 3
Period (Sec.)	Max. Stiffness	0.60	0.06	0.03
	Min. Stiffness	0.96	0.06	0.03
Frequency (Hz)	Max. Stiffness	1.66	15.55	30.09
	Min. Stiffness	1.04	15.46	30.07

Table 5-2 Free vibration test results.

Free Vibration Test	Damping Ratio (%)	Period (Sec.)
Fixed Base	0.6	0.102 (0.0035*)
El Centro-t	8.6	0.44
Loma Prieta-t	7.2	0.45
Chile-t	8.6	0.43

*-Mode 2

Table 5-3 Earthquake ground motion specifications.

Ground Motion	Direction	Station	Epic. Distance (km)	Station Site Class	PGA (g)	PGV (mm/s)	PGD (mm)
El Centro (1940)	S00E	117 (USGS)	16.9	Stiff Soil (D)	0.348	332	106.4
Loma Prieta (1989)	315° Component	57563 (CGS)	21	Stiff Soil (D)	0.228	206	52.7
Chile (2010)	7° Component	CCSP (NMI)	109.1	N/A	0.65	381	201.0

Table 5-4 Testing matrix of shake table testing, including PGA, bearings, orientation and contact surfaces.

Test Series	Amplitudes (g)	Bearings	Bearing Orientation	Bearing Contact Surfaces
El Centro-t	0.1-0.5	B1-33, B4-22, B2-12, B5	90°	Machined Aluminum/ Steel
Loma Prieta -t	0.1-0.5	B1-21, B1-32, B2-22, B1-12	90°	Machined Aluminum/ Steel
Chile-t	0.1-0.5	B1-22, B3-11, B3-22, B1-31	90°	Machined Aluminum/ Steel
Loma Prieta -t	0.1-0.5	B1-21, B1-32, B2-22, B1-12	90°	Grit Pads
Loma Prieta -t	0.1-0.4	B1-21, B1-32, B2-22, B1-12	45°	Grit Pads

Table 5-5 Measured response maxima of the base isolated (BI) structure.

Input Earthquake	PGA (g)	PGD (mm)	x_o (%t_r)	a_0 (g)	f_{BI} peak (Hz)	a_2 (g)	V_b/W	Min. Fs_{ove}	Δ (%)
El Centro-t	0.10	8	34	0.07	1.70	0.07	0.05	12.81	0.03
	0.20	16	67	0.11	1.60	0.12	0.07	8.06	0.05
	0.30	24	98	0.13	1.60	0.14	0.09	6.76	0.05
	0.40	31	145	0.17	1.13	0.17	0.11	5.58	0.06
	0.50	42	205	0.24	1.12	0.28	0.17	3.48	0.10
Loma Prieta-t	0.10	10	49	0.09	1.36	0.09	0.06	9.90	0.04
	0.20	21	107	0.14	1.32	0.14	0.09	6.47	0.06
	0.30	34	192	0.20	1.32	0.22	0.14	4.21	0.07
	0.40	45	253	0.30	1.33	0.34	0.21	2.84	0.15
	0.50	55	311	0.34	1.33	0.40	0.23	2.42	0.29
Chile-t	0.10	11	26	0.06	1.62	0.06	0.04	15.73	0.03
	0.20	21	54	0.09	1.62	0.10	0.06	9.24	0.04
	0.30	32	84	0.12	1.63	0.14	0.08	6.95	0.05
	0.40	42	132	0.14	1.62	0.16	0.10	5.84	0.06
	0.50	52	175	0.17	1.42	0.19	0.12	4.90	0.07

*W=weight of the base isolated structure, 32.1kN.

Table 5-6 Measured peak response values of the base isolated (BI) structure.

Input Earthquake	PGA (g)	x_o (%t_r)	Out-of-plane Accel. (g)	Vertical Accel. (g)	Micro Strain (με)	Torsion (Rad.)	Residual Torsional Offset (Rad.)	Residual Slip (%t_r)
El Centro-t	0.10	34	0.005	0.002	11.46	0.0007	0.0000	0.48
	0.20	67	0.007	0.005	17.01	0.0007	0.0001	0.26
	0.30	98	0.009	0.008	19.56	0.0009	0.0000	0.61
	0.40	145	0.012	0.013	23.14	0.0009	0.0000	1.43
	0.50	205	0.023	0.025	43.05	0.0016	-0.0004	0.65
Loma Prieta-t	0.10	49	0.005	0.004	15.04	0.0006	0.0002	0.65
	0.20	107	0.011	0.014	21.52	0.0007	0.0000	0.00
	0.30	192	0.021	0.030	32.63	0.0008	0.0000	7.27
	0.40	253	0.047	0.065	60.40	0.0023	-0.0011	24.14
	0.50	311	0.052	0.149	70.47	0.0038	-0.0015	41.19
Chile-t	0.10	26	0.007	0.004	9.60	0.0008	0.0001	0.48
	0.20	54	0.012	0.006	14.93	0.0009	0.0002	1.21
	0.30	84	0.015	0.009	19.09	0.0010	0.0002	1.12
	0.40	132	0.015	0.011	20.02	0.0010	0.0005	3.38
	0.50	175	0.017	0.019	21.99	0.0009	0.0002	7.10

Table 5-7 Measured response maxima of the Loma Prieta-t earthquake records with grit pads and 45° orientation bearings.

Input Earthquake	PGA (g)	PGD (mm)	x_o (%t_r)	a_0 (g)	f_{BI} peak (Hz)	a_2 (g)	V_b/W*	Min. Fs_{ove}	Δ (%)
Loma Prieta-t	0.10	10.31	49	0.09	1.36	0.09	0.06	9.93	0.04
	0.20	21.42	107	0.14	1.32	0.14	0.09	6.49	0.06
	0.30	33.71	192	0.20	1.32	0.22	0.14	4.23	0.07
	0.40	44.67	253	0.30	1.33	0.34	0.21	2.85	0.15
	0.50	55.36	311	0.34	1.33	0.40	0.23	2.43	0.29
Loma Prieta-t with grit	0.10	10.31	51	0.08	1.37	0.09	0.06	10.61	0.05
	0.20	21.46	110	0.13	1.33	0.14	0.09	6.75	0.06
	0.30	33.52	191	0.21	1.33	0.23	0.14	4.07	0.07
	0.40	44.44	249	0.29	1.33	0.34	0.21	2.77	0.15
	0.50	55.10	301	0.38	1.32	0.40	0.25	2.32	0.27
Loma Prieta-t with grit (45°)	0.10	10.29	50	0.08	1.38	0.08	0.05	11.39	0.04
	0.20	21.38	112	0.12	1.34	0.13	0.09	7.08	0.06
	0.30	33.62	194	0.17	1.32	0.18	0.12	5.14	0.06
	0.40	44.59	261	0.22	1.33	0.24	0.15	3.98	0.11

*W=weight of the base isolated structure, 32.1kN.

Table 5-8 Measured peak values of the base isolated (BI) structure subjected to the Loma Prieta-t records with grit pads and 45° orientation bearings

Input Earthquake	PGA (g)	Out-of-plane Accel. (g)	Vertical Accel. (g)	Micro Strain (με)	Torsion (Rad.)	Residual Torsional Offset (Rad.)	Residual Slip (%t_r)
Loma Prieta-t	0.10	0.005	0.004	15.04	0.0006	0.0002	0.65
	0.20	0.011	0.014	21.52	0.0007	0.0000	0.00
	0.30	0.021	0.030	32.63	0.0008	0.0000	7.27
	0.40	0.047	0.065	60.40	0.0023	-0.0011	24.14
	0.50	0.052	0.149	70.47	0.0038	-0.0015	41.19
Loma Prieta-t With Grit	0.10	0.006	0.003	14.93	0.0006	-0.0001	0.39
	0.20	0.009	0.011	19.44	0.0008	0.0000	0.30
	0.30	0.016	0.030	31.94	0.0008	-0.0002	2.98
	0.40	0.034	0.068	54.27	0.0014	-0.0005	8.52
	0.50	0.056	0.223	72.21	0.0056	-0.0016	13.97
Loma Prieta-t With Grit (45°)	0.10	0.008	0.004	16.66	0.0007	-0.0003	0.48
	0.20	0.014	0.011	22.68	0.0009	-0.0001	1.73
	0.30	0.016	0.020	25.23	0.0016	-0.0001	9.17
	0.40	0.030	0.056	29.74	0.0020	-0.0002	22.11

Table 5-9 Efficiency of the base isolated (BI) structure to the fixed base (FB) structure subjected to the table input earthquake records.

Earthquake	PGA (g)	x_o (%t_r)	a_2 (g)	a_2 (g)	V_b/W*	V_b/W*	Min. Fs_{ove}	Min. Fs_{ove}
			FB	% Reduction	FB	% Reduction	FB	% Increase
El Centro-t	0.10	34.05	0.18	60.4	0.15	67.6	3.88	330.2
	0.20	67.01	0.35	67.3	0.29	74.1	1.98	407.5
	0.30	97.63	0.52	73.7	0.42	79.2	1.34	502.7
	0.40	145.19	0.67	75.2	0.54	80.4	1.04	535.4
	0.50	205.47	0.77	64.4	0.64	73.8	0.89	391.2
Loma Prieta-t	0.10	48.62	0.30	68.4	0.25	75.9	2.28	433.1
	0.20	107.33	0.59	75.8	0.66	85.8	1.14	566.7
	0.30	191.72	0.91	75.3	0.77	82.0	0.74	566.3
	0.40	252.83	1.14	70.3	0.96	78.4	0.60	477.2
	0.50	310.53	1.39	71.5	1.16	80.4	0.50	486.3
Chile-t	0.10	26.32	0.34	82.5	0.26	85.2	2.16	729.1
	0.20	53.72	0.68	85.1	0.52	87.6	1.06	872.2
	0.30	84.17	1.03	86.8	0.79	89.4	0.70	991.1
	0.40	131.62	1.39	88.6	1.07	90.4	0.52	1125.5
	0.50	174.87	1.76	89.2	1.36	91.0	0.41	1196.2

*W=weight of the fixed base structure, 21.4kN

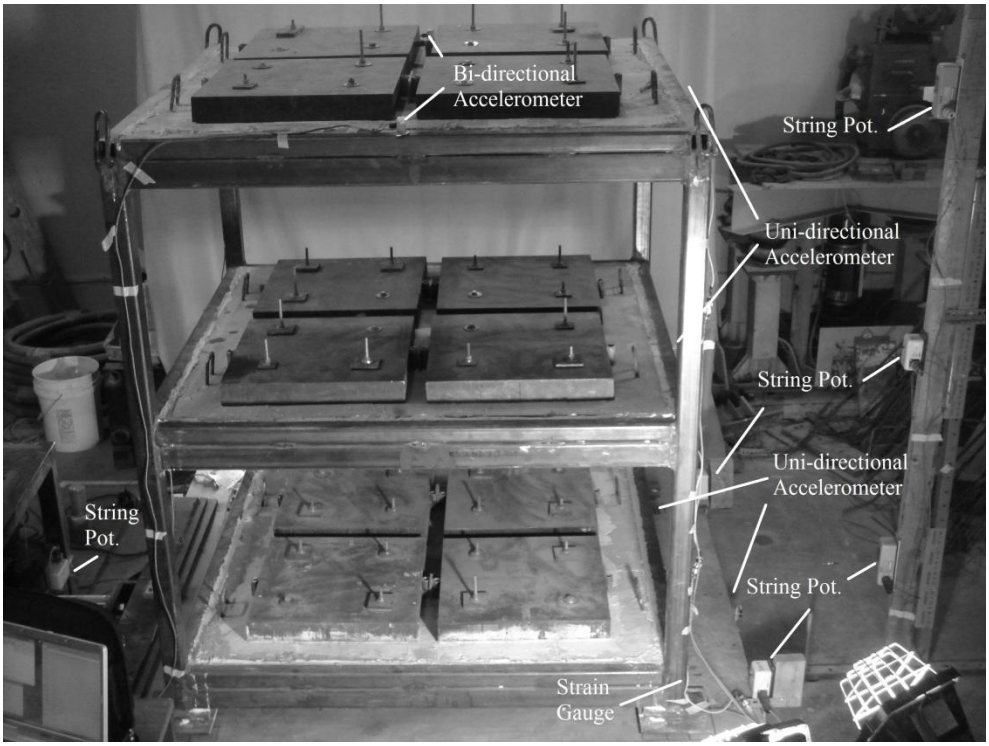

Figure 5.1 Instrumented test structure situated on the shake table

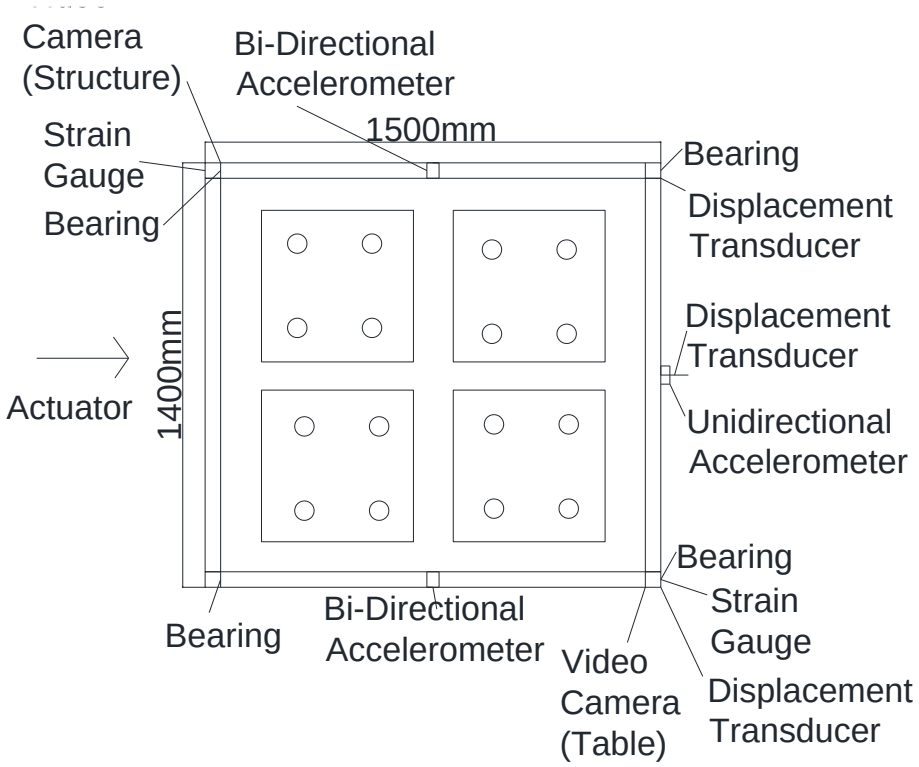

Figure 5.2 Plan view schematic of the quarter-scale structure.

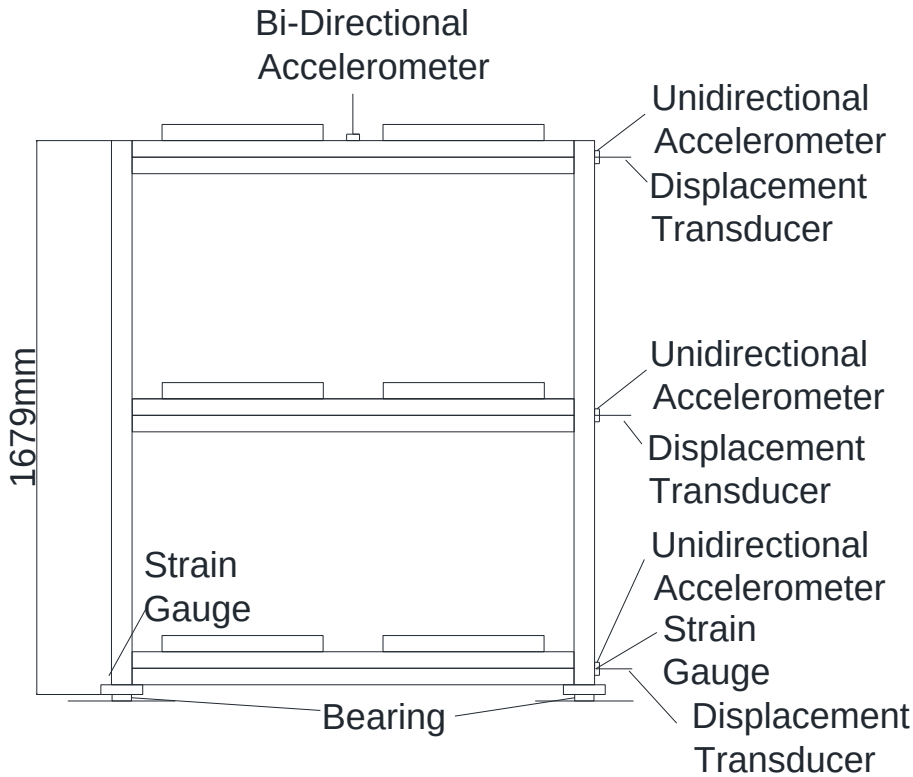

Figure 5.3 Elevation view schematic of the quarter-scale structure

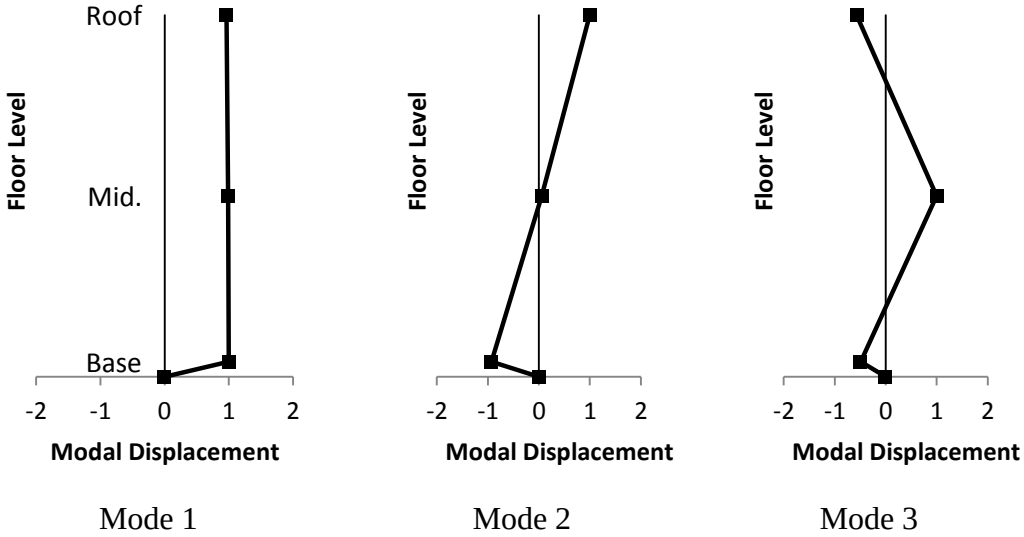

Mode 1 Mode 2 Mode 3

Figure 5.4 Mode shapes of the BI structure.

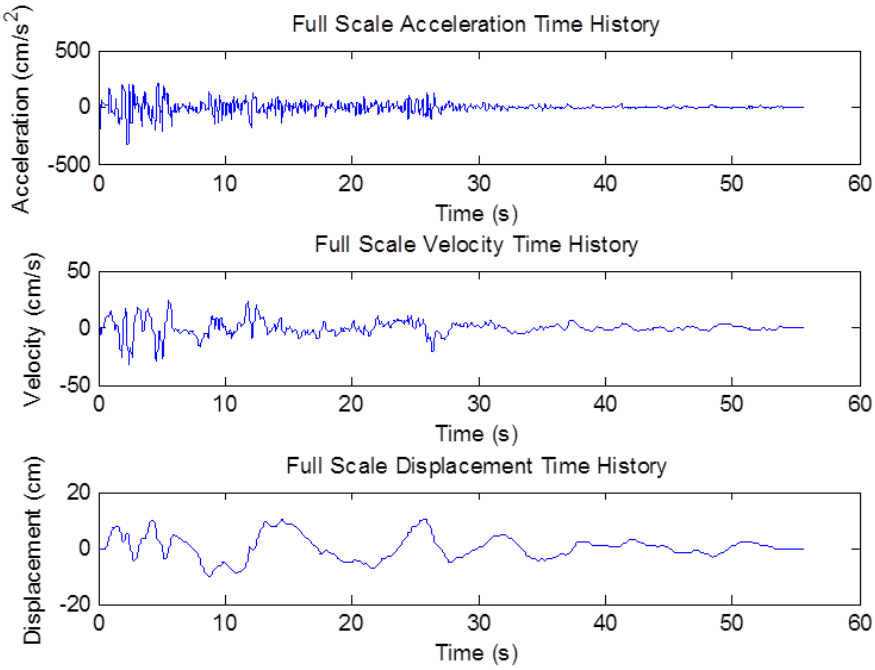

Figure 5.5 Original time history plots of the El Centro (1940) record.

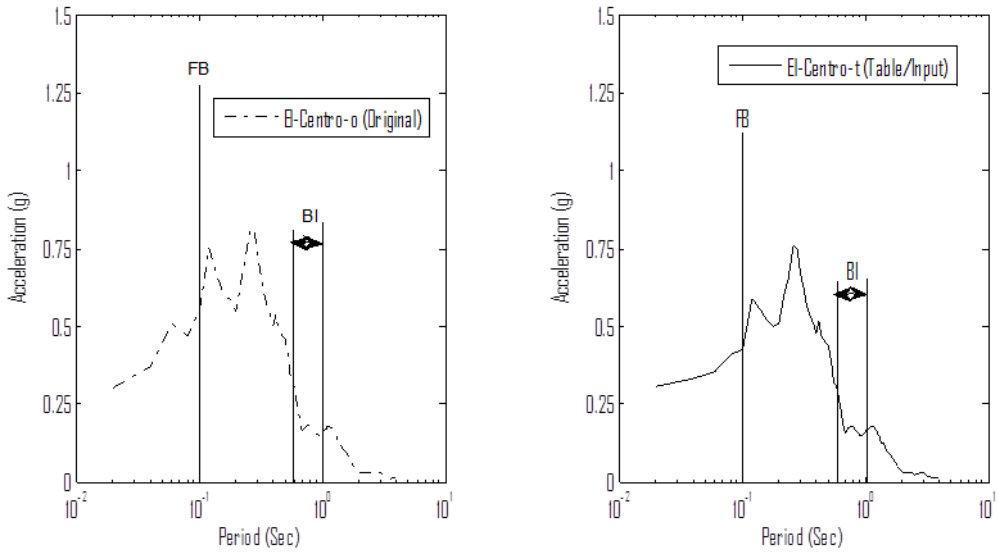

Figure 5.6 (a) Original scaled El Centro-o response spectrum and (b) table generated El Centro-t response spectrum.

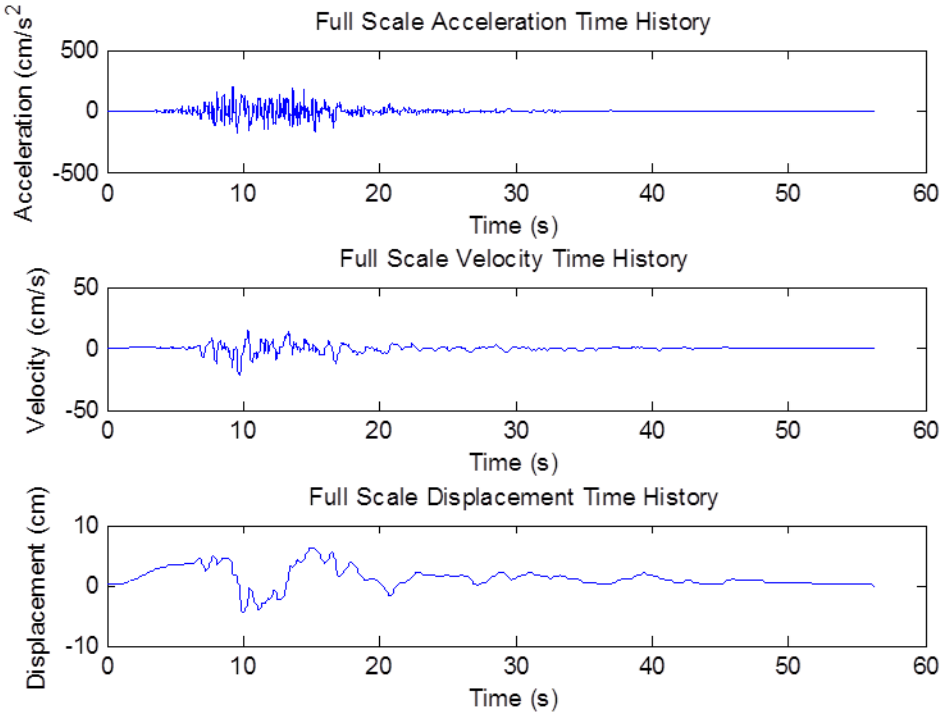

Figure 5.7 Original time history plots of the Loma Prieta (1989) record.

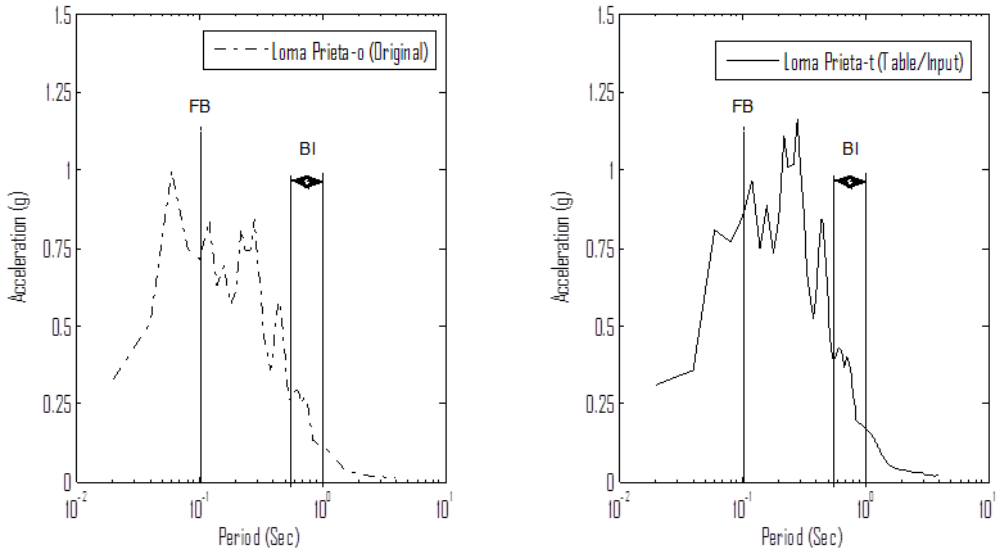

Figure 5.8 (a) Original scaled Loma Prieta-o response spectrum and (b) table generated Loma Prieta-t response spectrum.

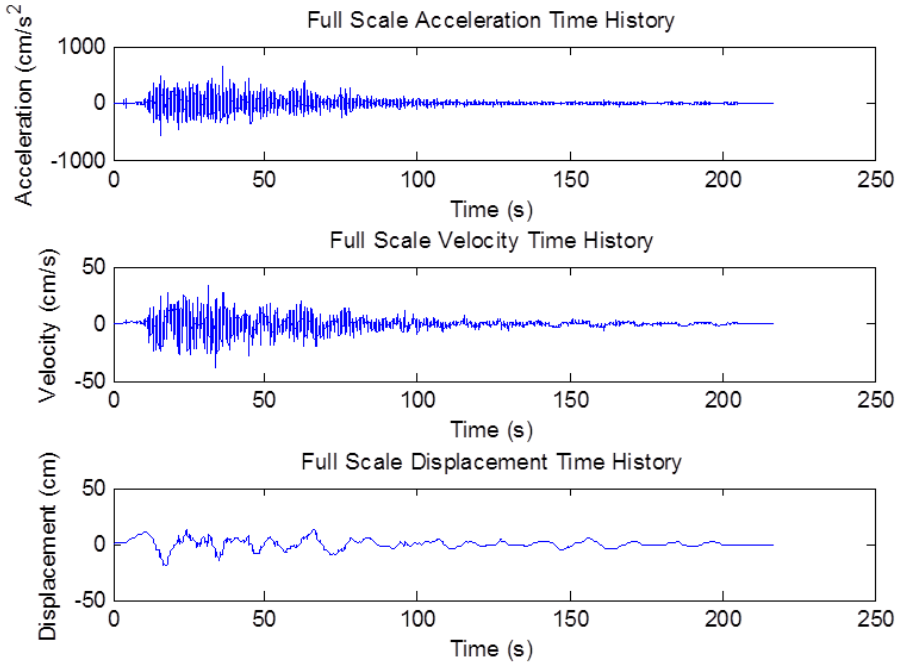

Figure 5.9 Original time history plots of Chile (2010) record.

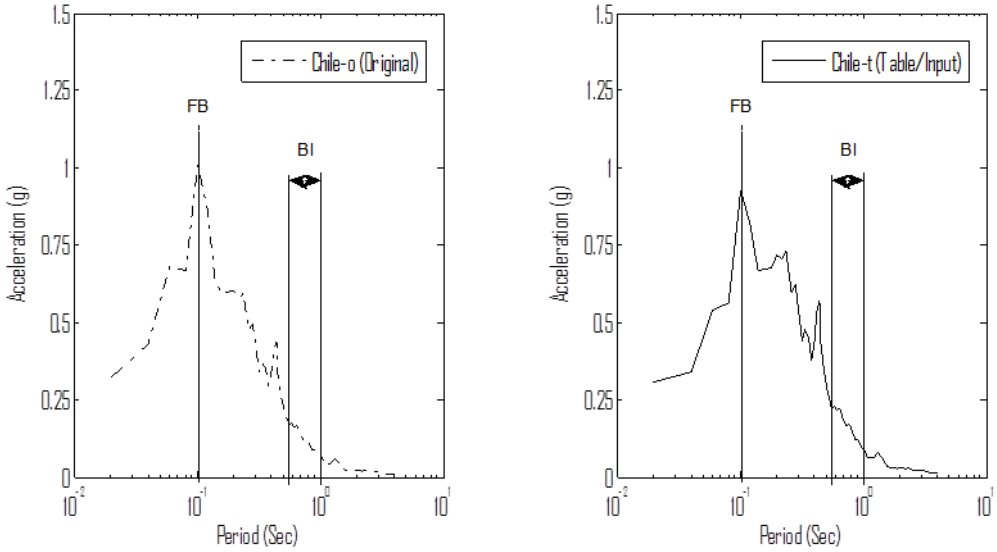

Figure 5.10 (a) Original scaled Chile-o response spectrum and (b) table generated Chile-t response spectrum.

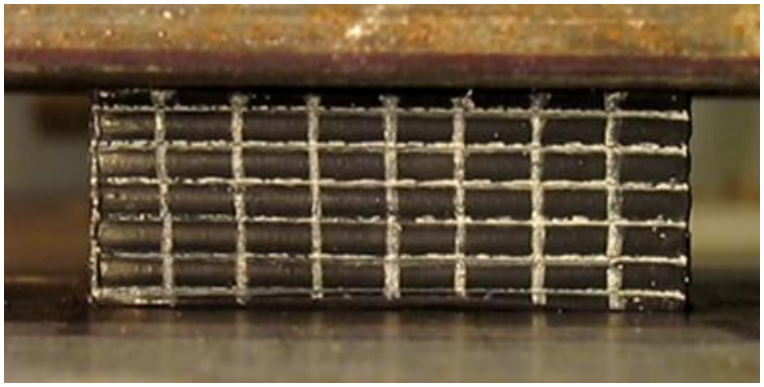

Figure 5.11 90° orientation of the bearing under the test structure.

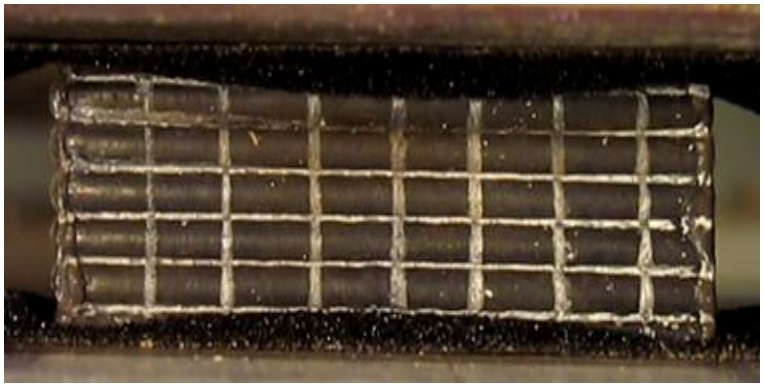

Figure 5.12 Photograph showing the grit paper used to investigate the influence of friction on slip.

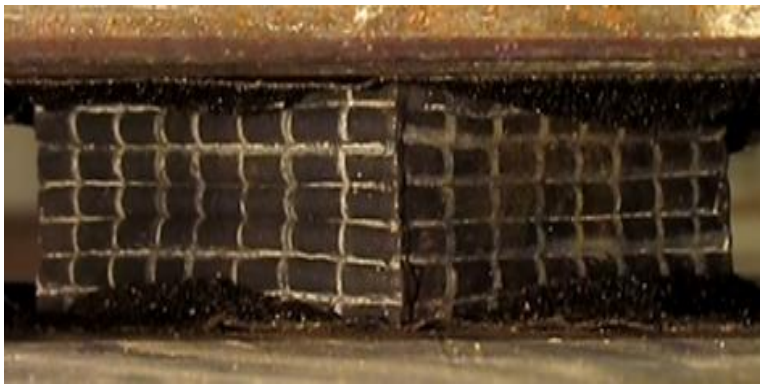

Figure 5.13 45° orientation beneath the test structure with the grit paper.

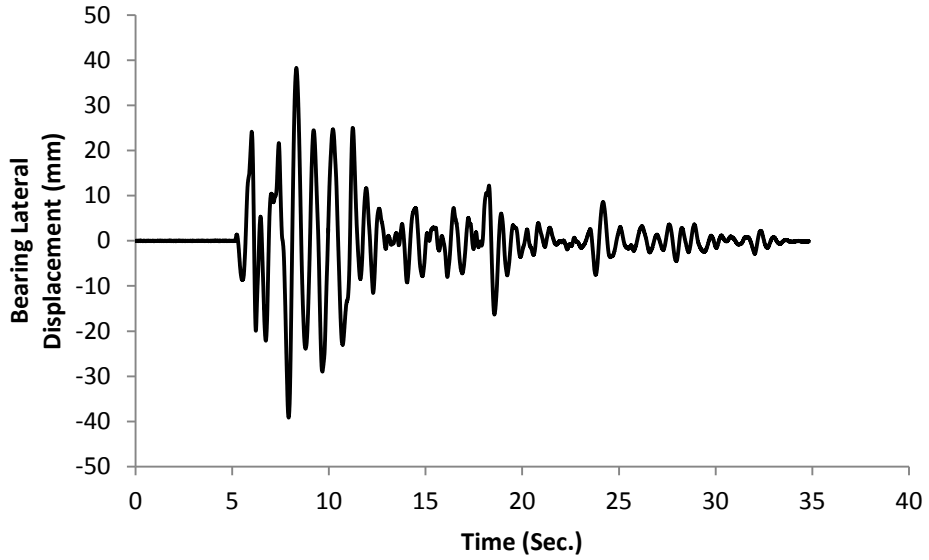

Figure 5.14 Bearing lateral displacement time history for the 0.5g PGA El Centro-t record.

Figure 5.15 Peak rollover deformation during the 0.5g PGA El Centro-t record.

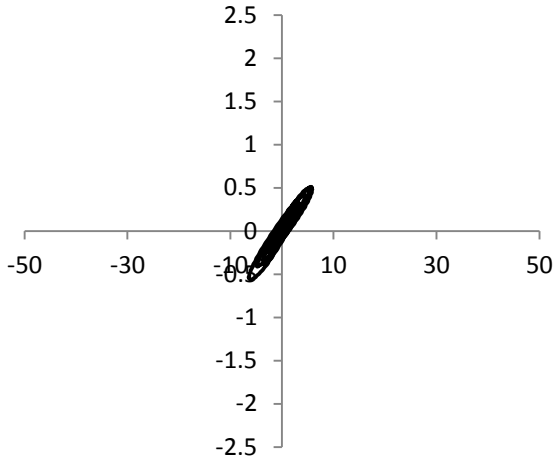

0.1PGA

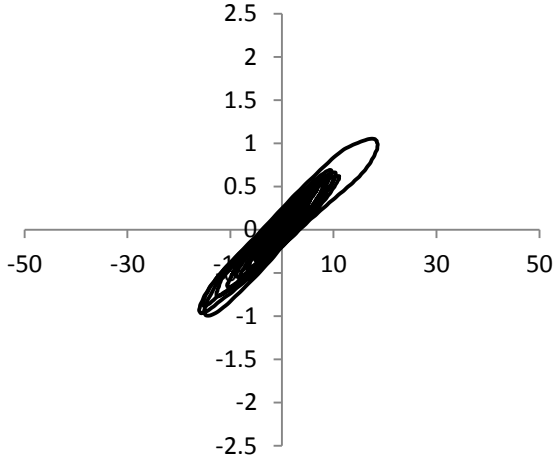

0.3PGA

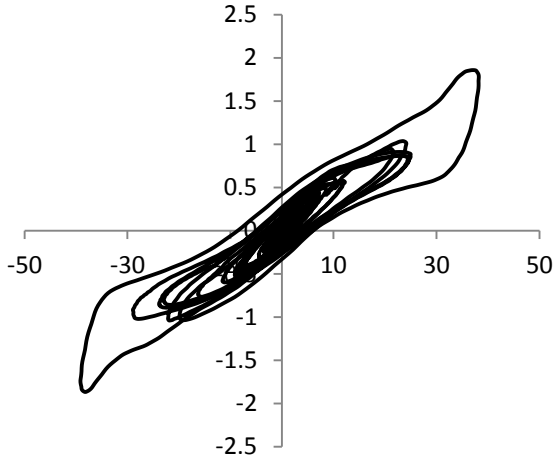

0.5PGA

Figure 5.16 Bearing hysteresis from El Centro-t 0.1, 0.3 and 0.5g PGA.

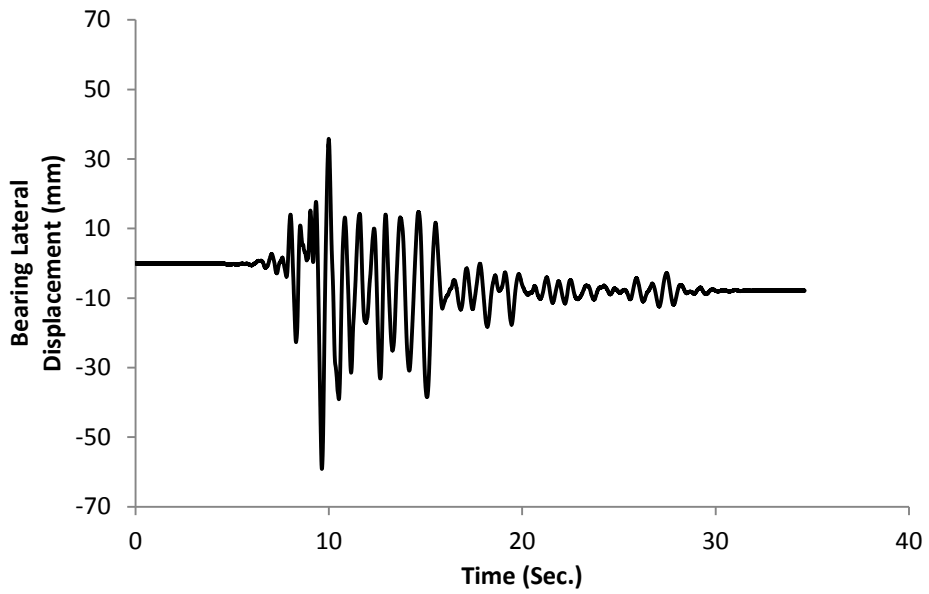

Figure 5.17 Bearing lateral displacement time history for the 0.5g PGA Loma Prieta-t record.

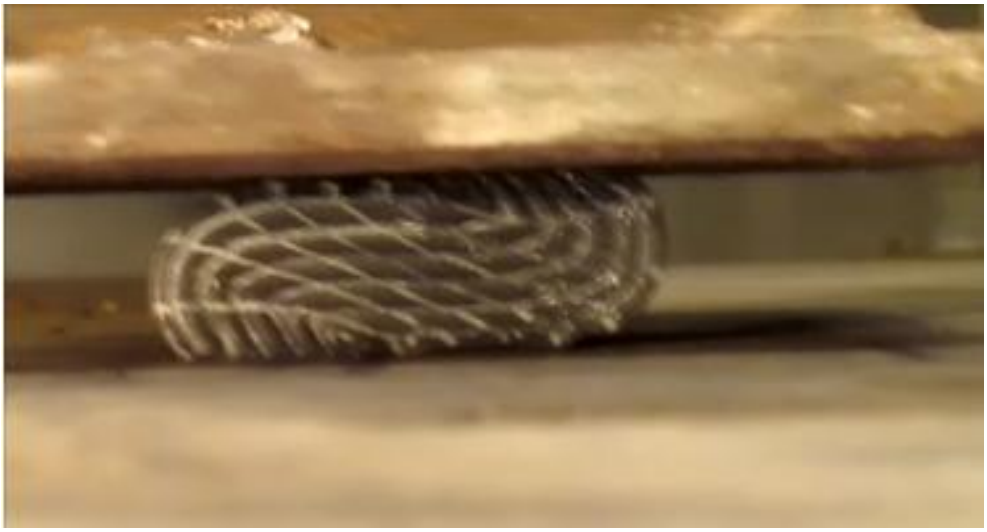

Figure 5.18 Peak rollover deformation during the 0.5g PGA Loma Prieta-t record.

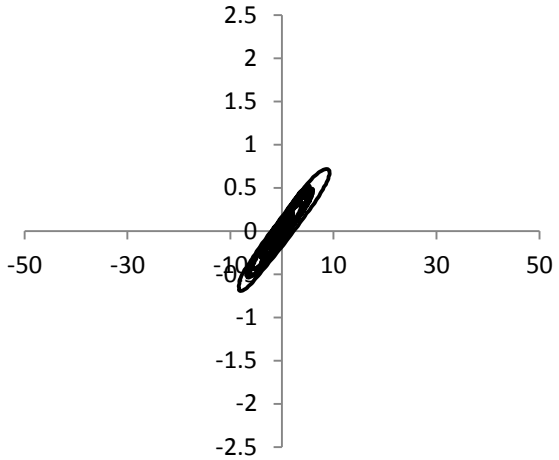

0.1PGA

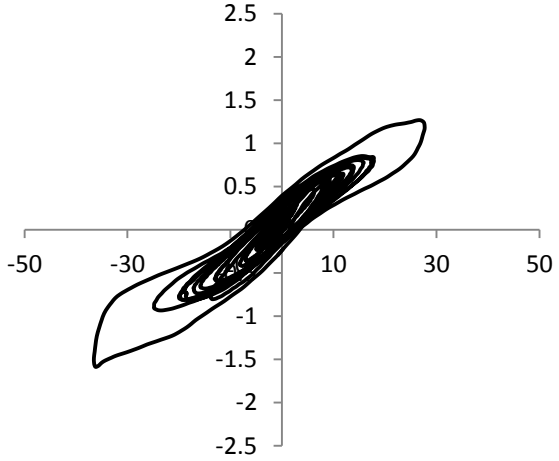

0.3PGA

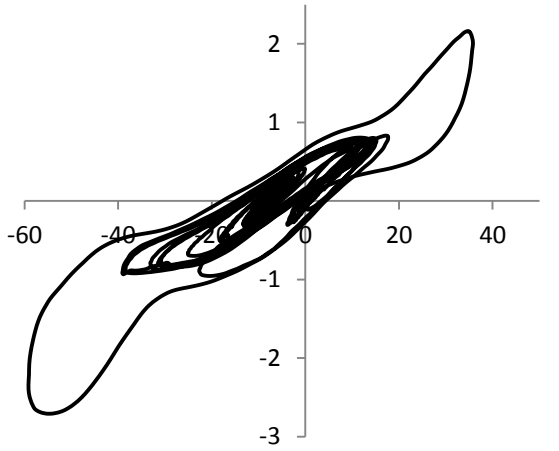

0.5PGA

Figure 5.19 Bearing hysteresis from Loma Prieta-t 0.1, 0.3 and 0.5g PGA.

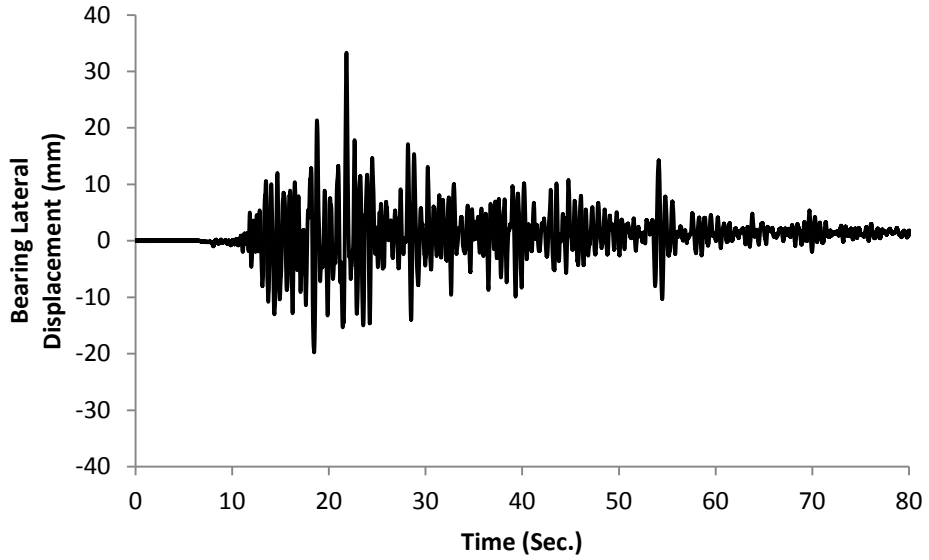

Figure 5.20 Bearing lateral displacement time history for the 0.5g PGA Chile-t record.

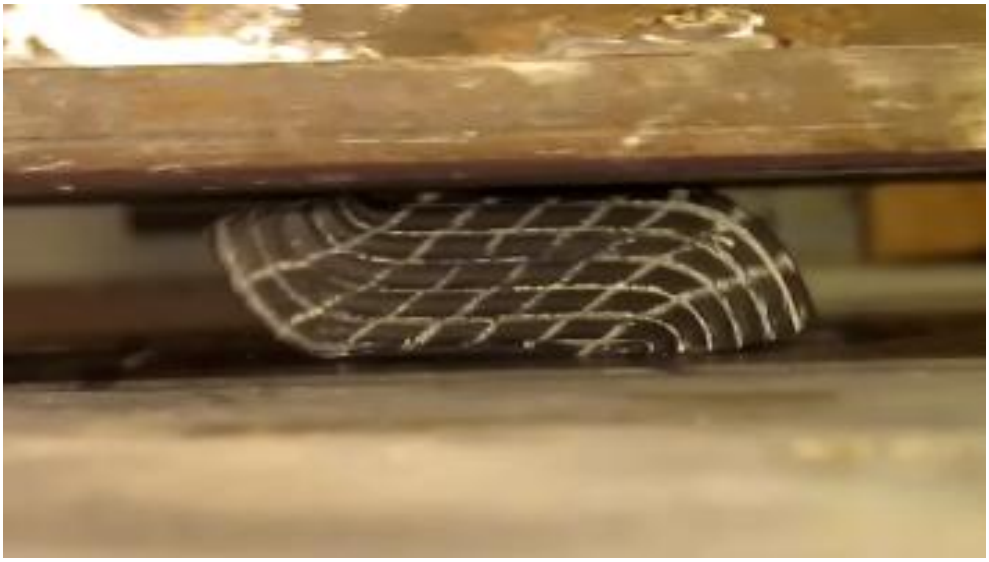

Figure 5.21 Peak rollover deformation during the 0.5g PGA Chile-t record.

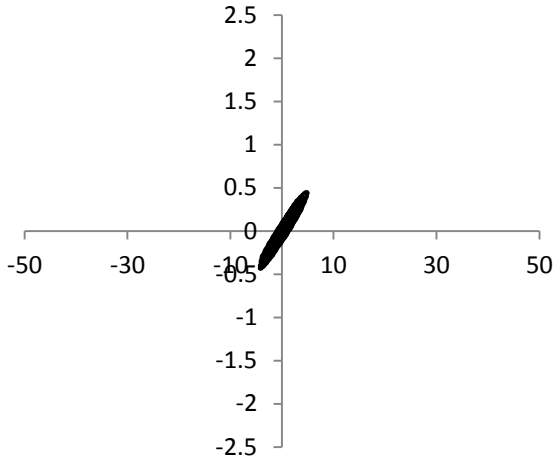

0.1PGA

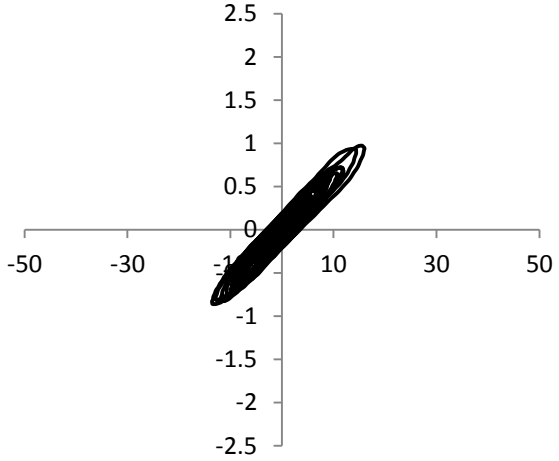

0.3PGA

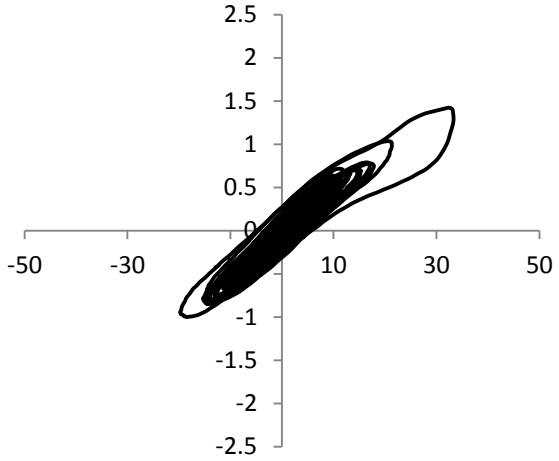

0.5PGA

Figure 5.22 Bearing lateral displacement time history for the 0.5g PGA Chile-t record.

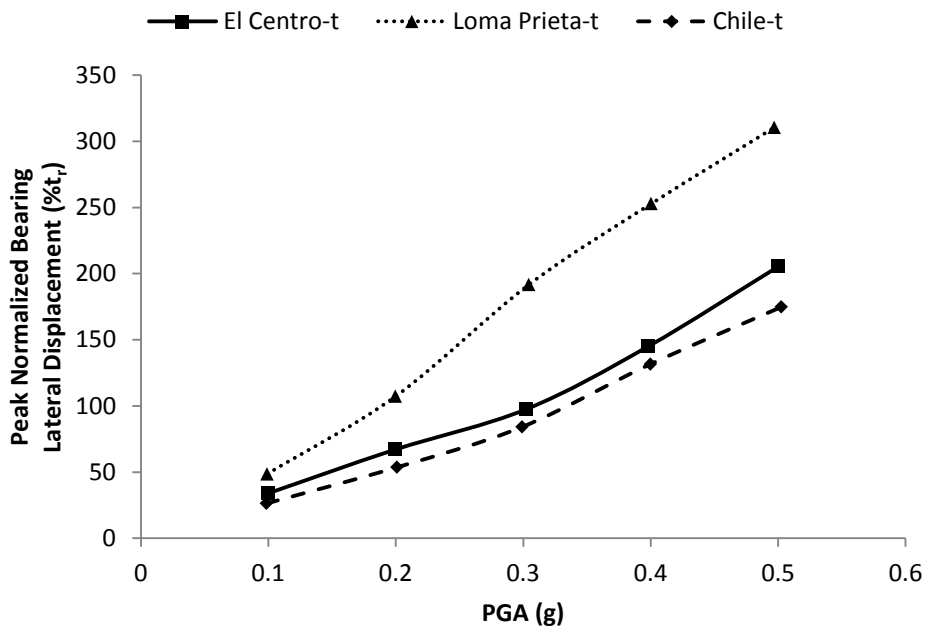

Figure 5.23 Bearing lateral displacement with respect to the ground motion intensity (PGA).

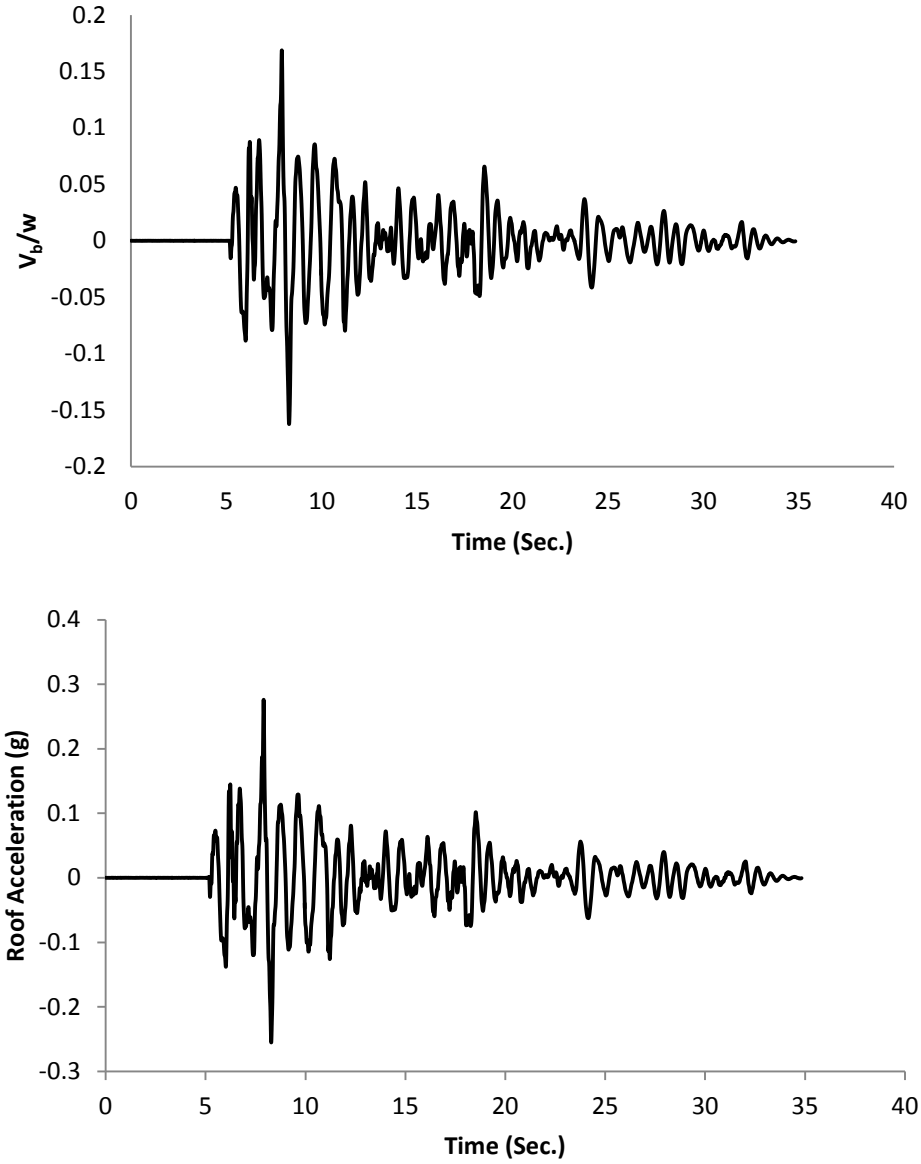

Figure 5.24 Normalized base shear (top) and roof acceleration (bottom) time histories for the 0.5g PGA El Centro-t record.

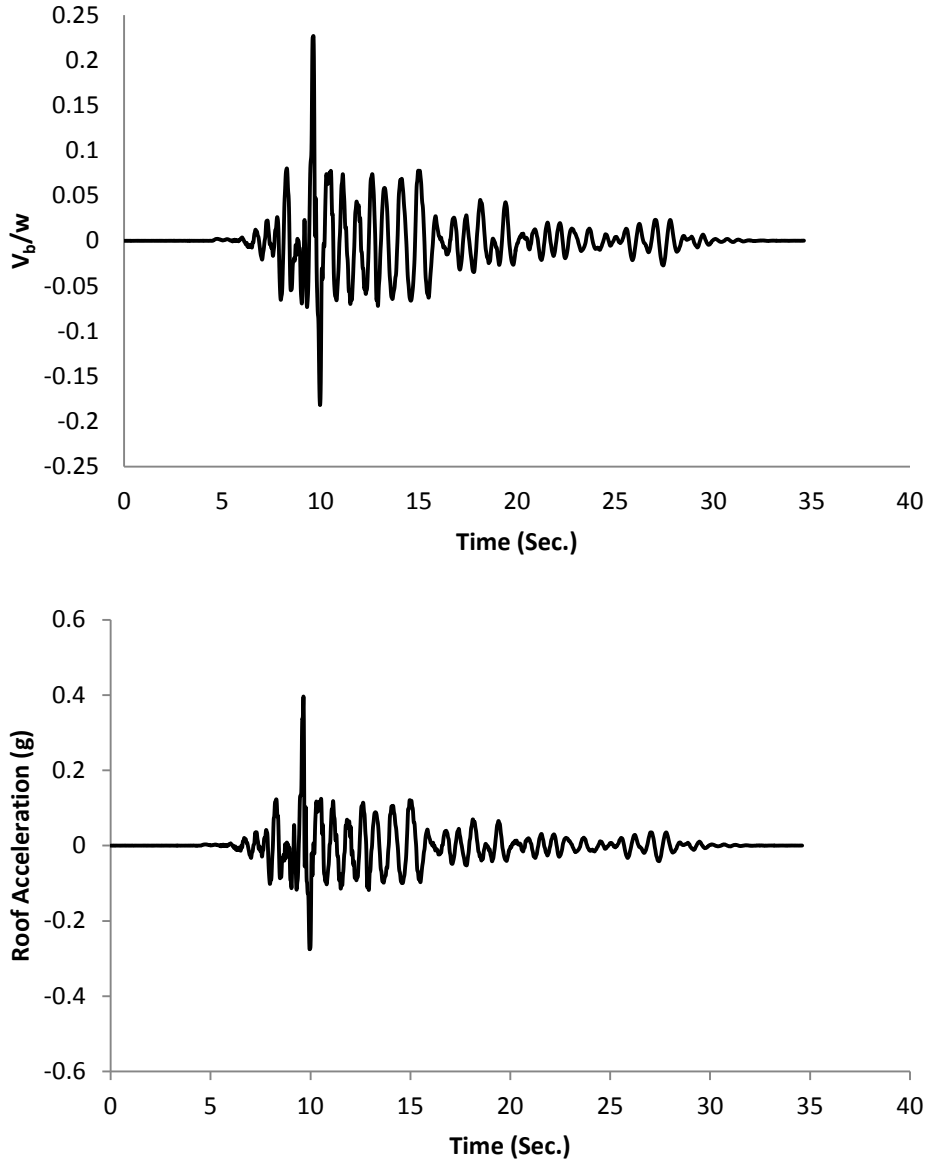

Figure 5.25 Normalized base shear (top) and roof acceleration (bottom) time histories for the 0.5g PGA Loma Prieta-t record.

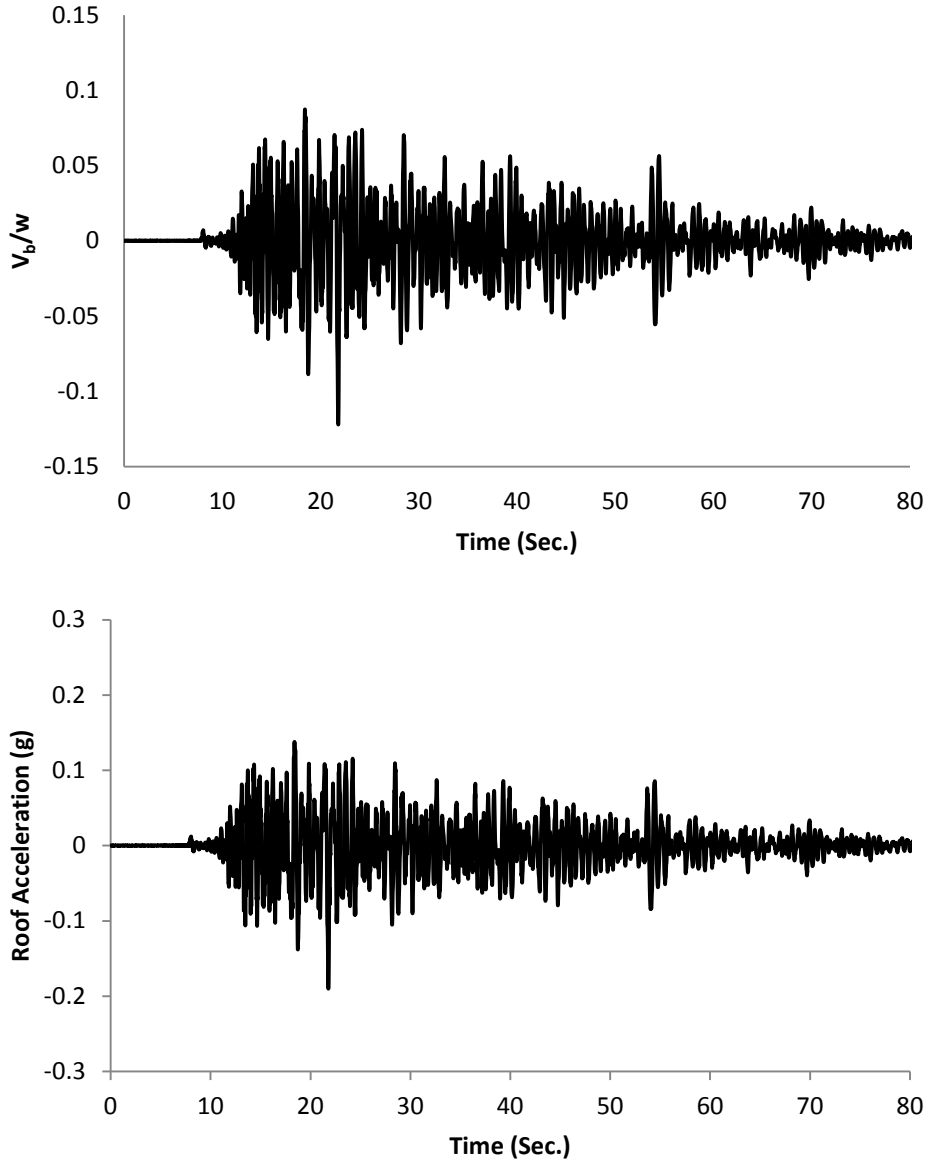

Figure 5.26 Normalized base shear (top) and roof acceleration (bottom) time histories for the 0.5g PGA Chile-t record.

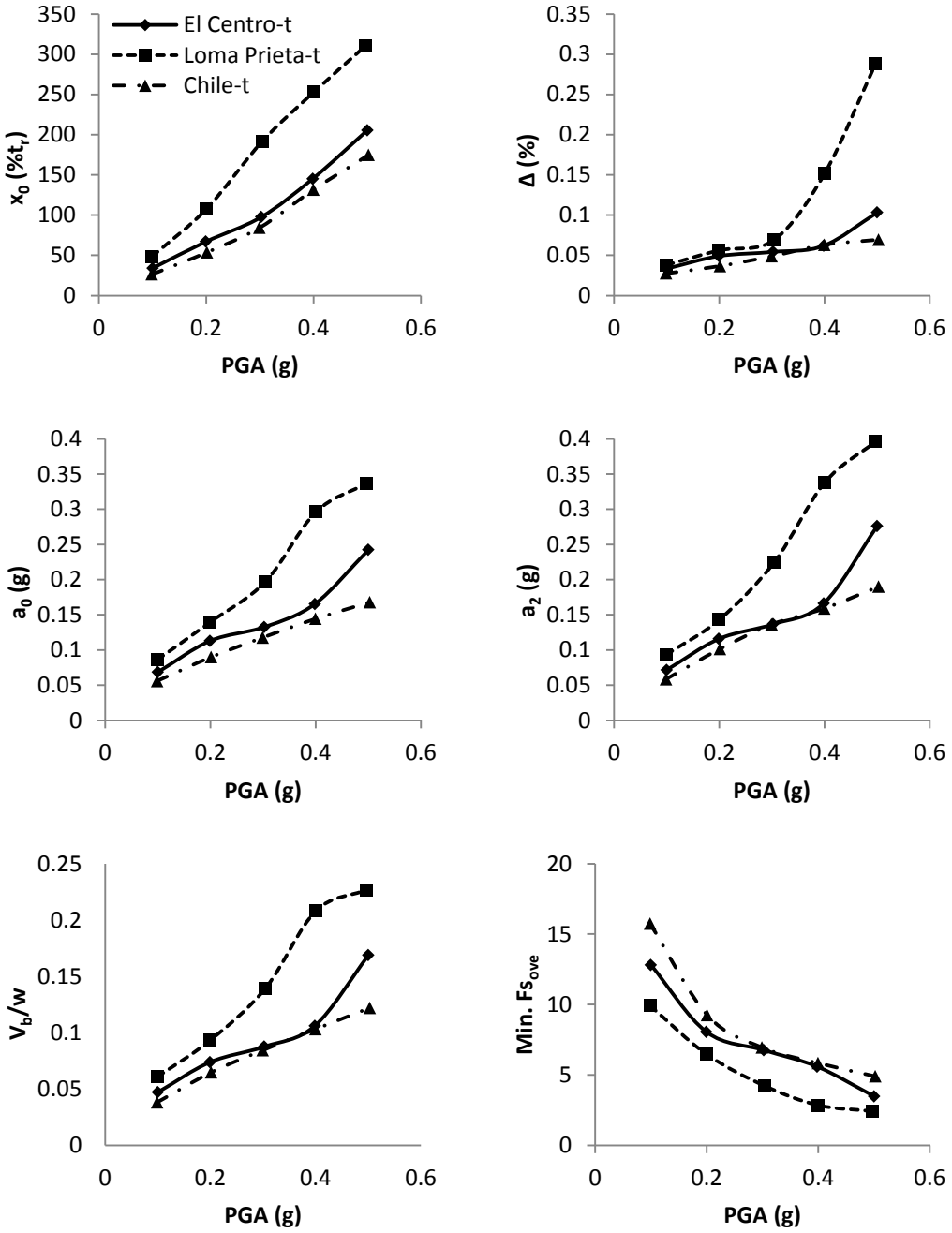

Figure 5.27 Charts displaying the peak response parameters with respect to intensity (PGA).

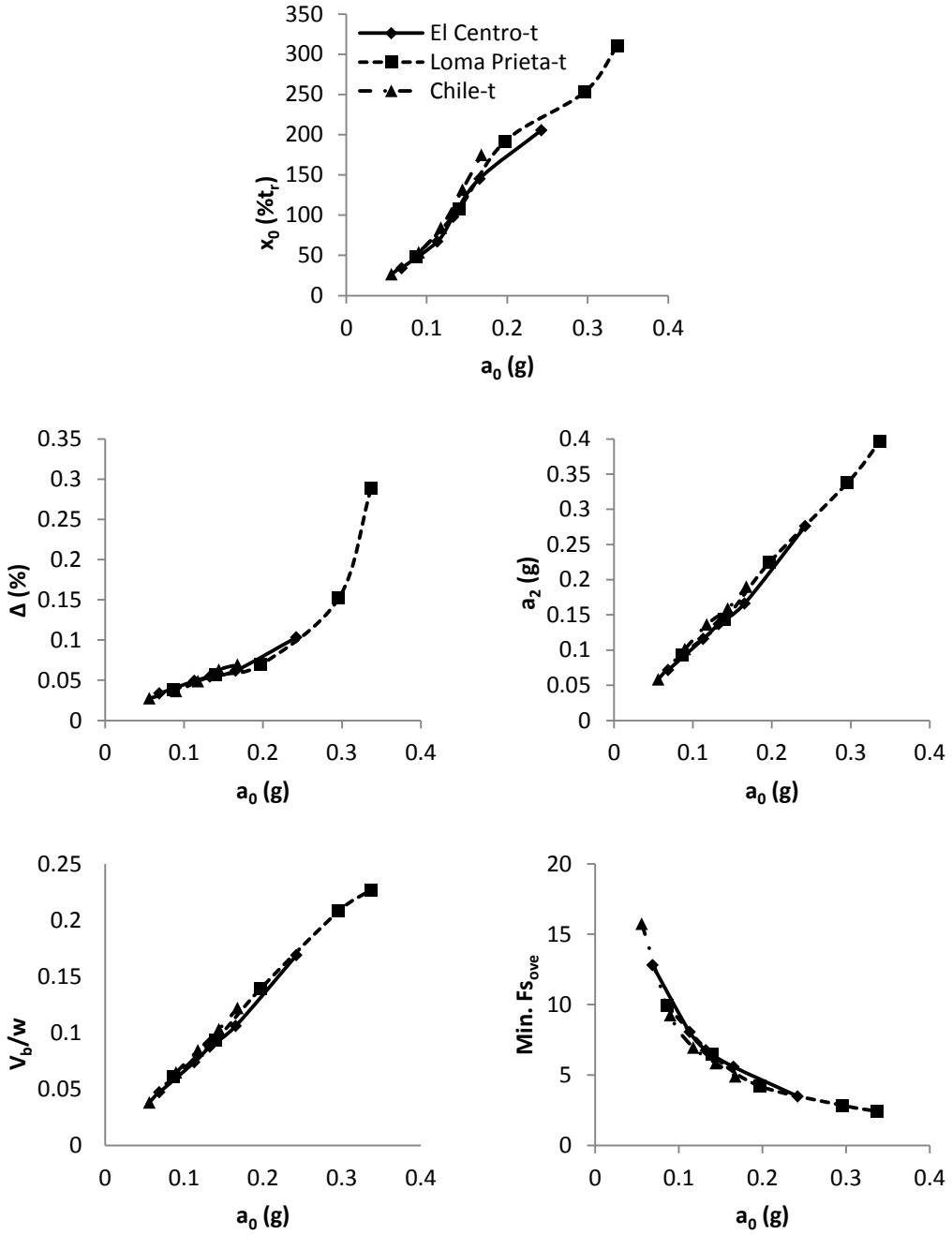

Figure 5.28 Charts displaying the peak response parameters with respect to base acceleration (a_0).

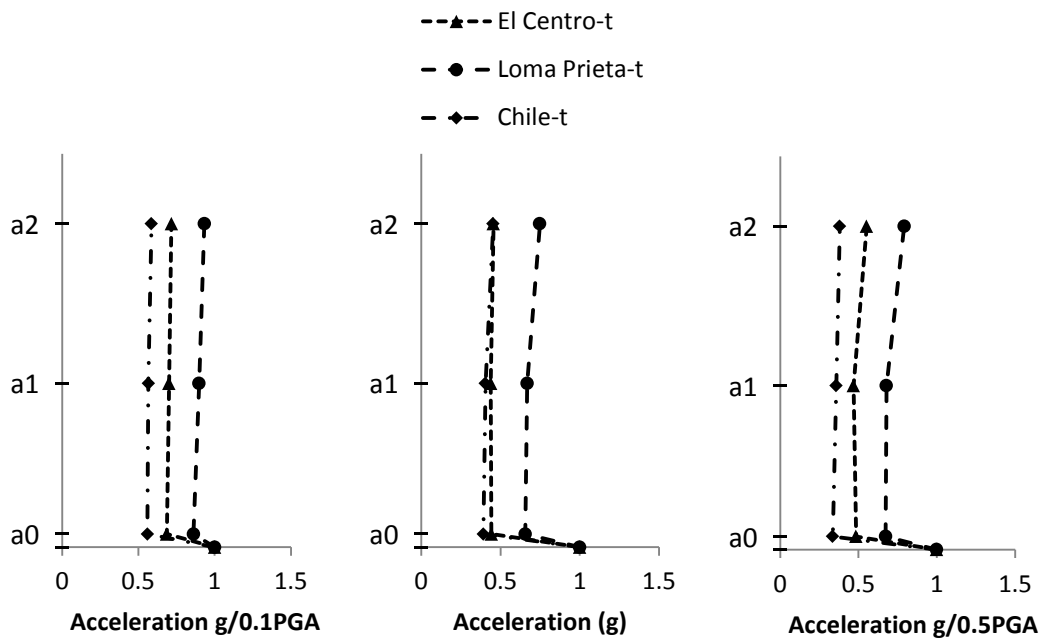

Figure 5.29 Amplification envelops of the peak acceleration response along the height of the structure for the 0.1, 0.3 and 0.5g PGA input earthquake records.

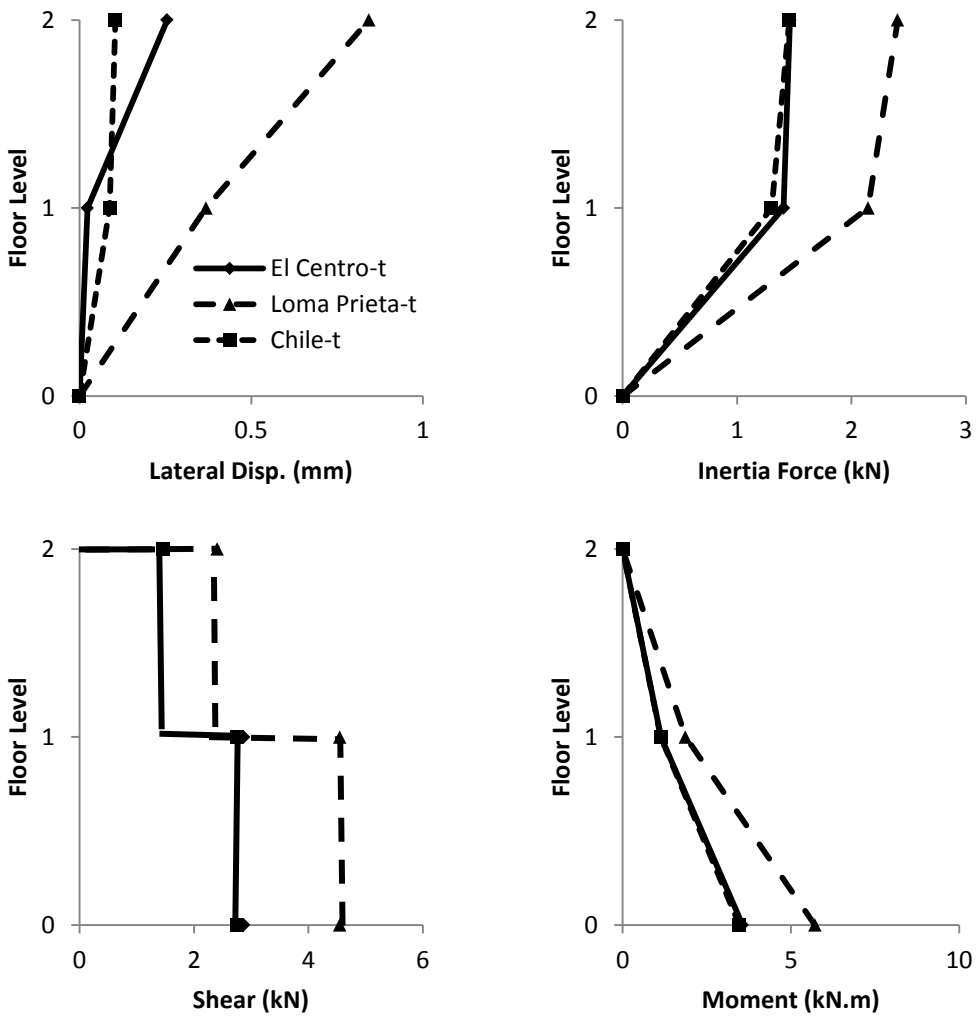

Figure 5.30 Peak response parameters along the height of the structure for the 0.3g PGA input records.

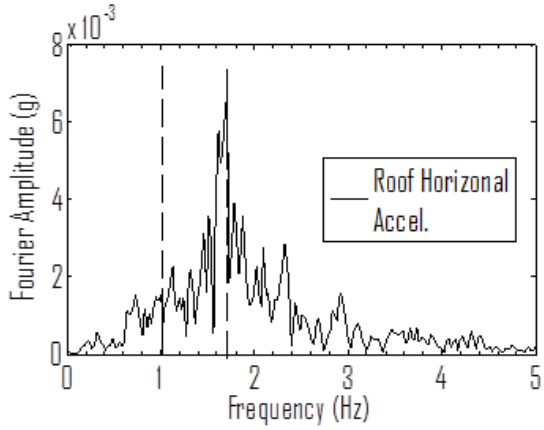

0.1g PGA

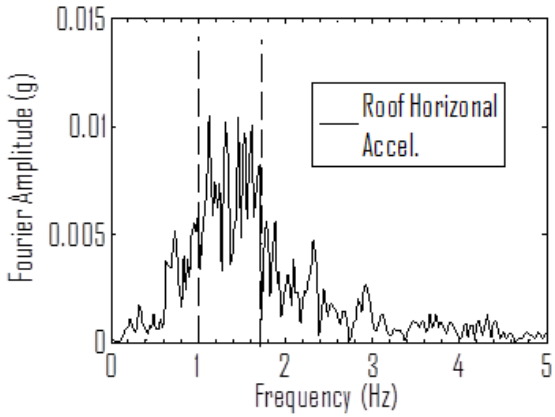

0.3g PGA

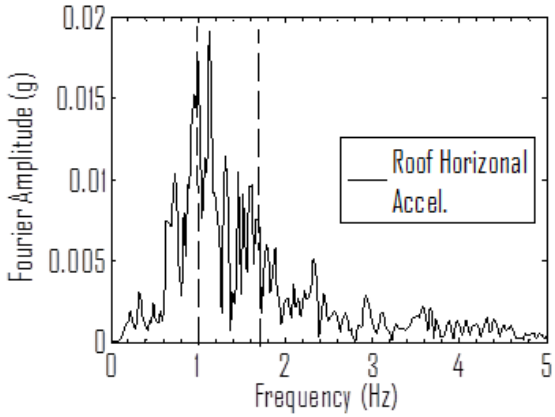

0.5g PGA

Figure 5.31 Lateral (horizontal) Fourier amplitude spectra of the BI-structure subjected to 0.1, 0.3 and 0.5g PGA El Centro-t input earthquake; comparison between the first modes frequency with PGA amplitude. (Note: The dashed vertical lines represent the frequency range or frequency of the expected modes.)

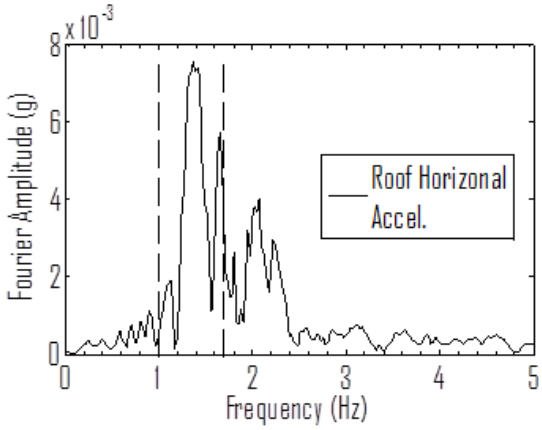

0.1g PGA

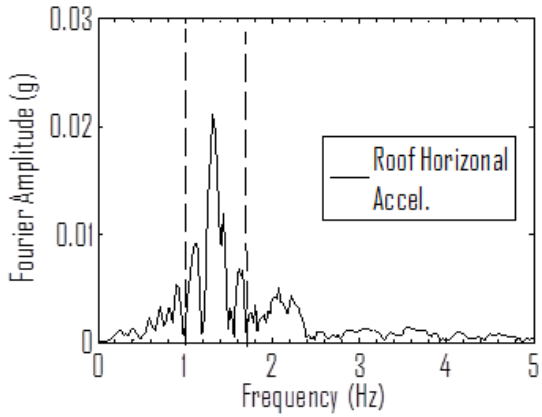

0.3g PGA

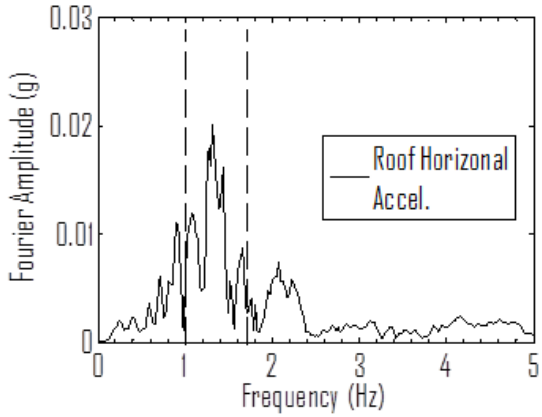

0.5g PGA

Figure 5.32 Lateral horizontal Fourier amplitude spectra of the BI-structure subjected to 0.1, 0.3 and 0.5g PGA Loma Prieta-t input earthquake; comparison between the first modes frequency with PGA amplitude. (Note: The dashed vertical lines represent the frequency range or frequency of the expected modes.)

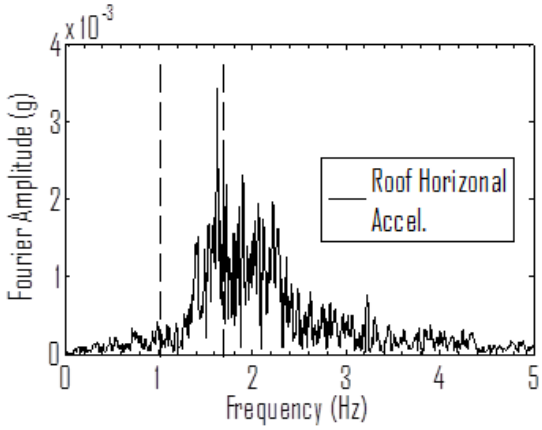

0.1g PGA

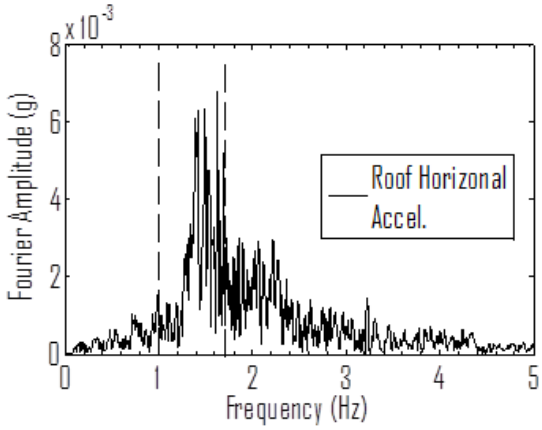

0.3g PGA

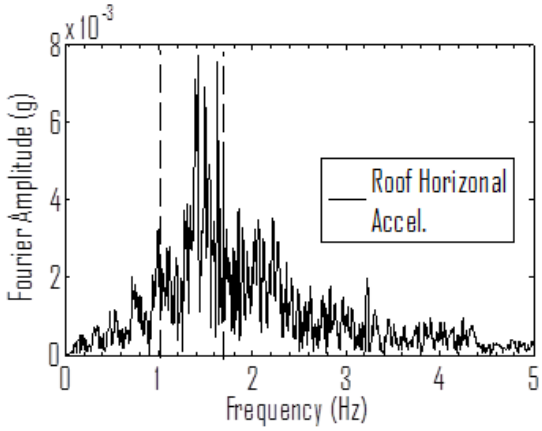

0.5g PGA

Figure 5.33 Lateral horizontal Fourier amplitude spectra of the BI-structure subjected to 0.1, 0.3 and 0.5g PGA Chile-t input earthquake; comparison between the first modes frequency with PGA amplitude. (Note: The dashed vertical lines represent the frequency range or frequency of the expected modes.)

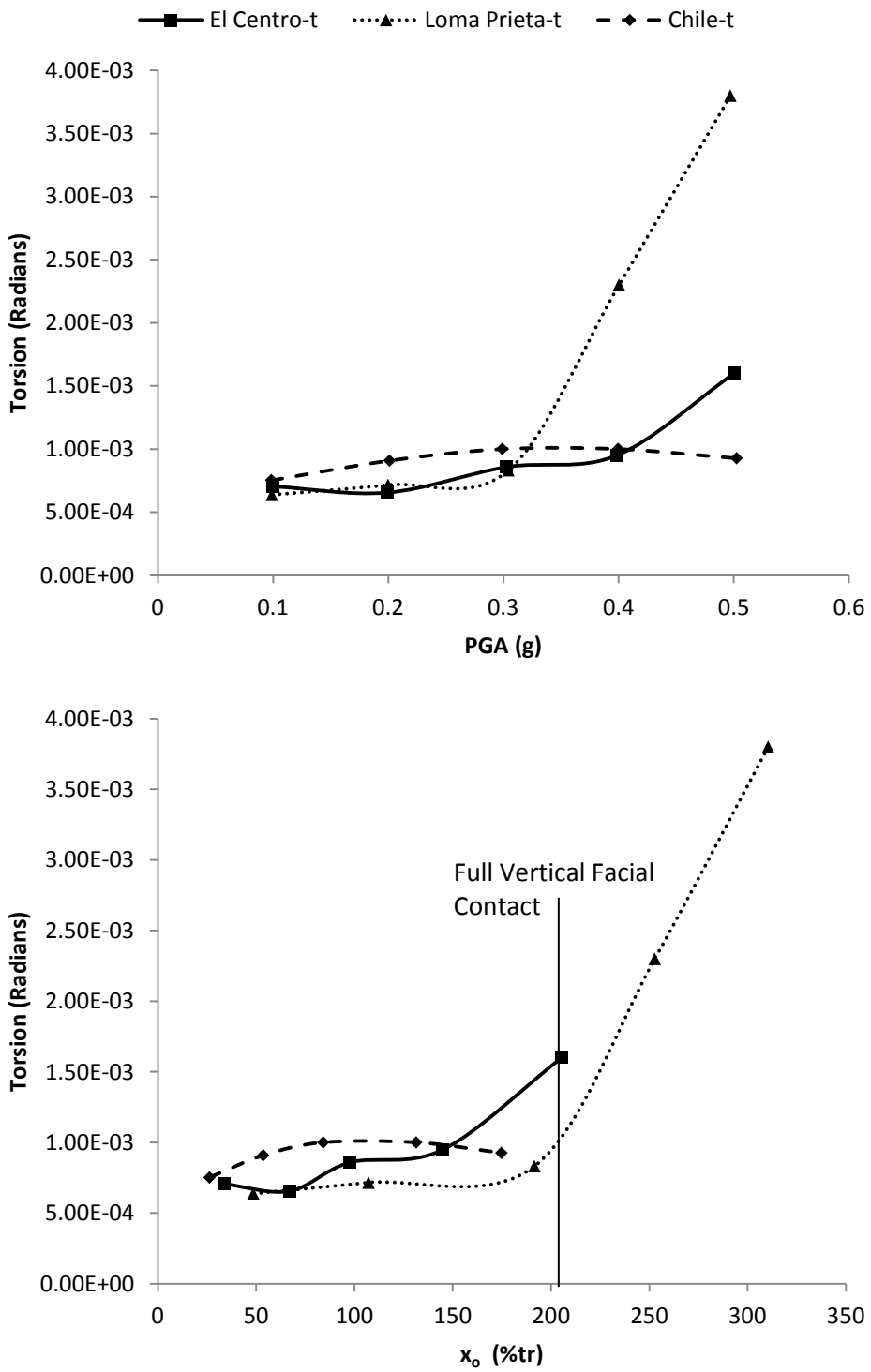

Figure 5.34 Peak torsional response of the BI-structure with respect to PGA (top) and bearing lateral displacement (bottom).

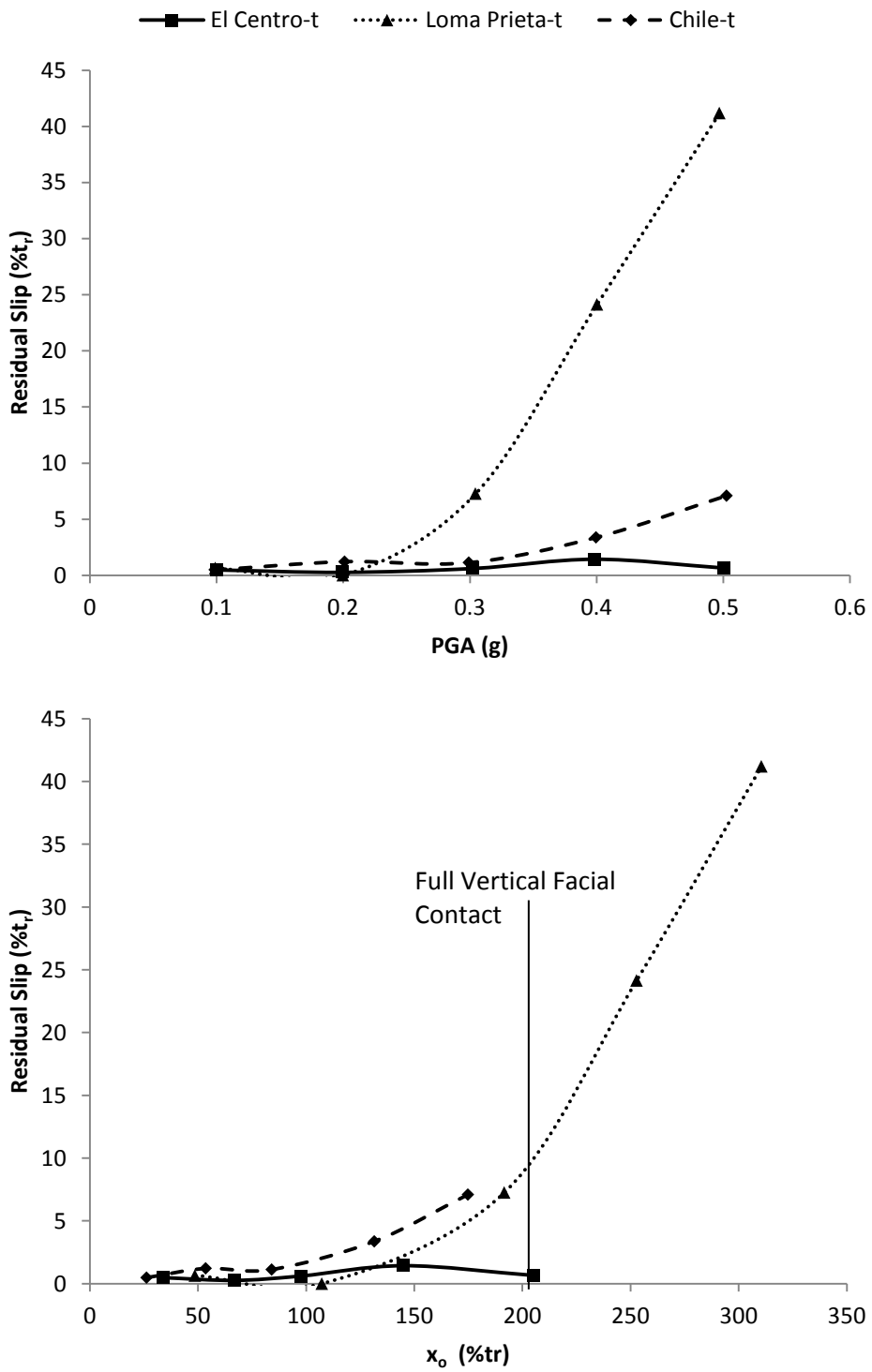

Figure 5.35 Peak residual slip of the BI-structure with respect to PGA (top) and bearing lateral displacement (bottom).

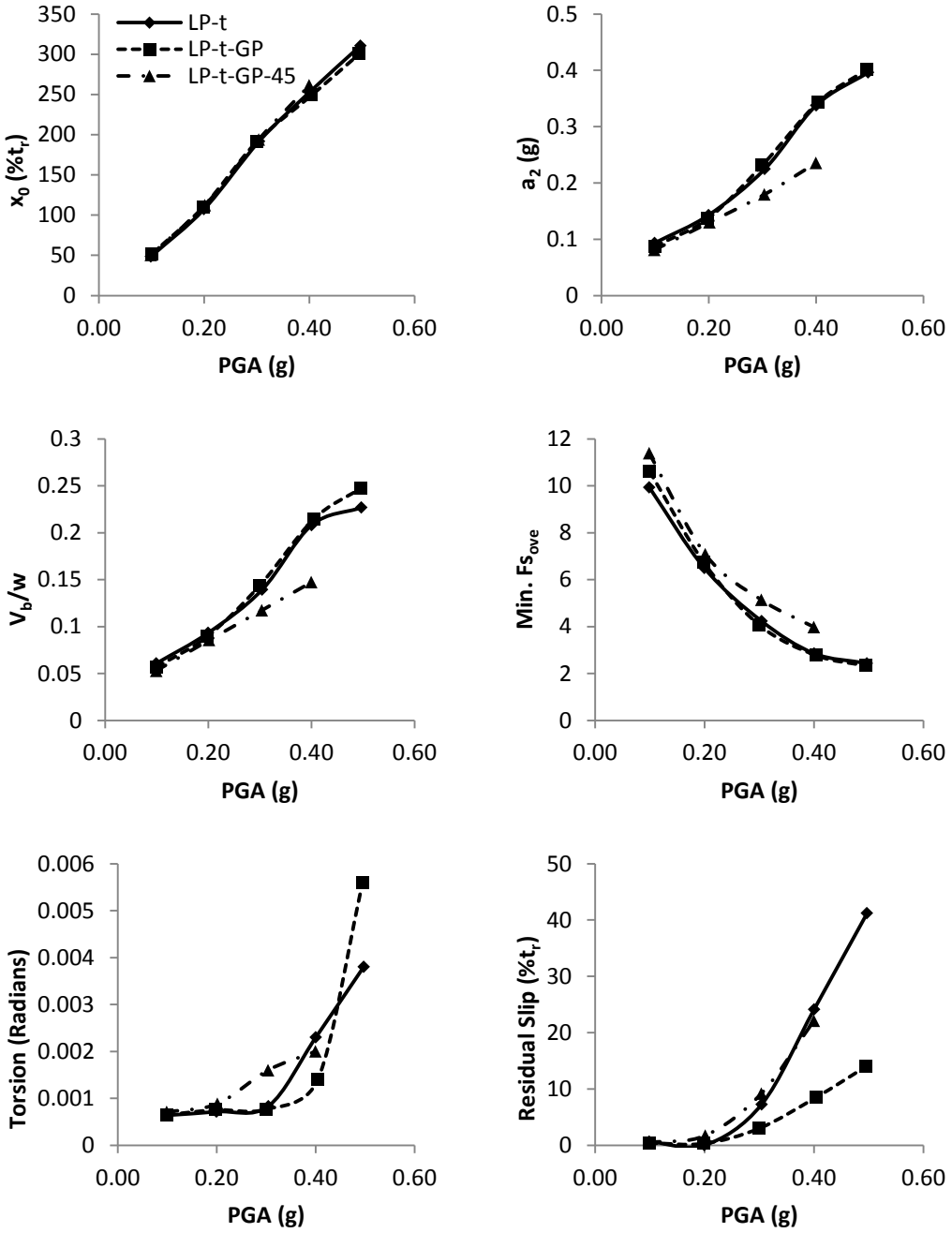

Figure 5.36 Peak response parameters with respect to intensity (PGA) for the three LomaPrieta-t tests. (Note: LP-t = Loma Prieta-t, LP-t-GP = Loma Prieta-t with grit paper and LP-t-GP-45 = Loma Prieta-t with grit paper with 45° orientation).

Figure 5.37 Photograph of delamination of bearing B1-12.

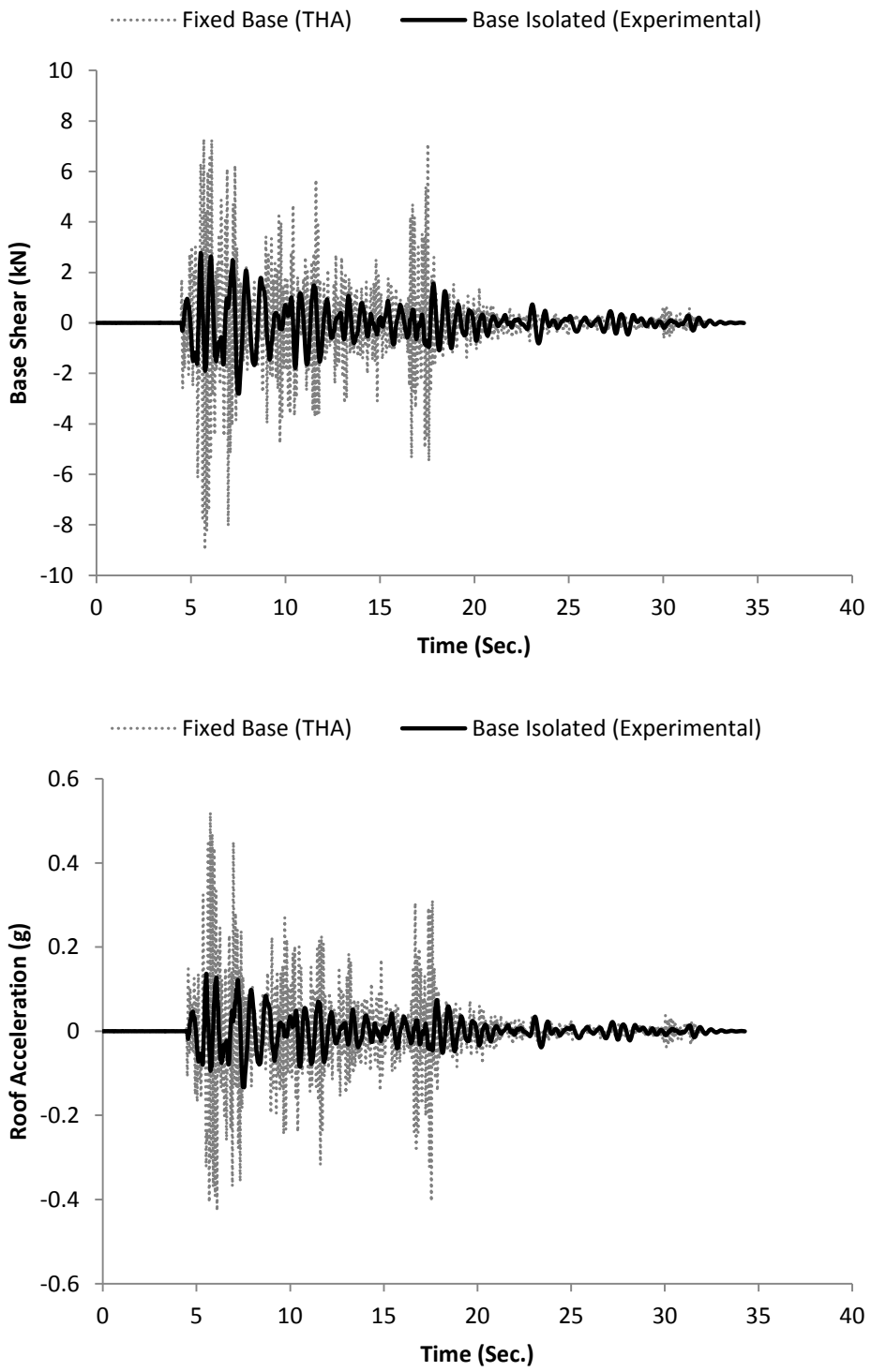

Figure 5.38 Time history response of the BI-structure and the 5% damped linear FB-structure subjected to the 0.3PGA El Centro-t input earthquake. (Top: Base shear, Bottom: Roof acceleration).

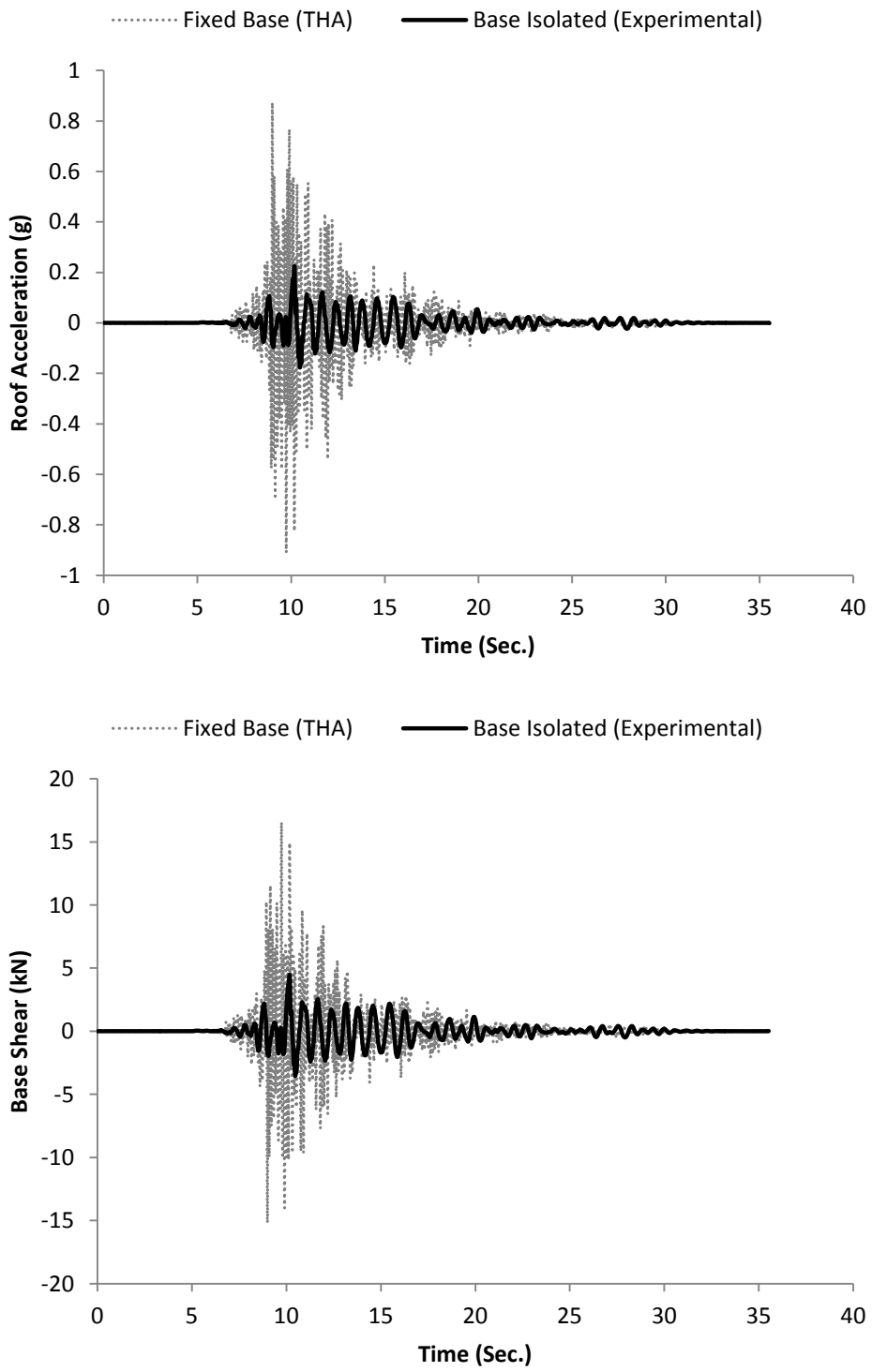

Figure 5.39 Time history response of the BI-structure and the 5% damped linear FB-structure subjected to the 0.3PGA Loma Prieta-t input earthquake. (Top: Base shear, Bottom: Roof acceleration).

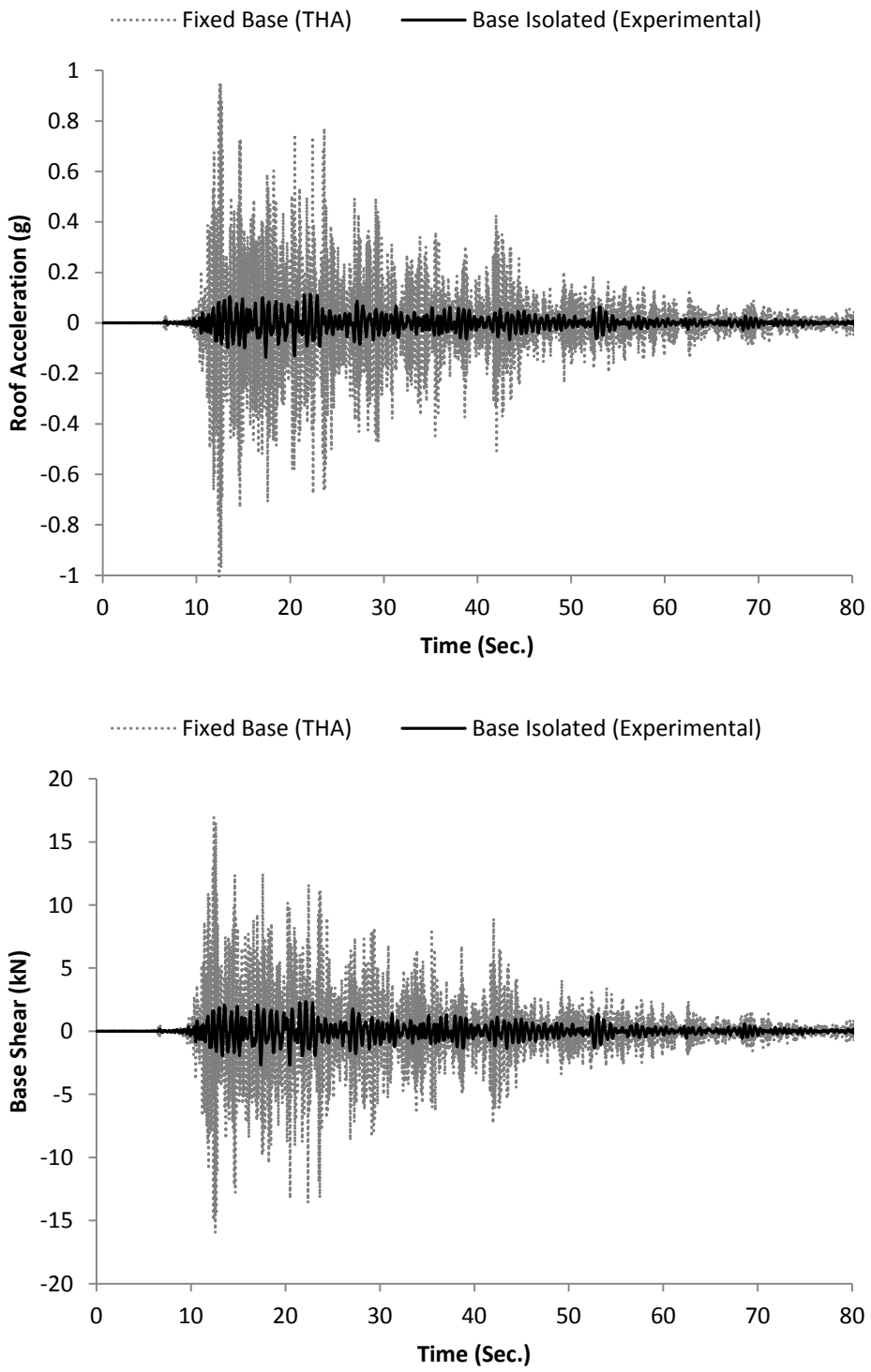

Figure 5.40 Time history response of the BI-structure and the 5% damped linear FB-structure subjected to the 0.3PGA Chile-t input earthquake. (Top: Base shear, Bottom: Roof acceleration).

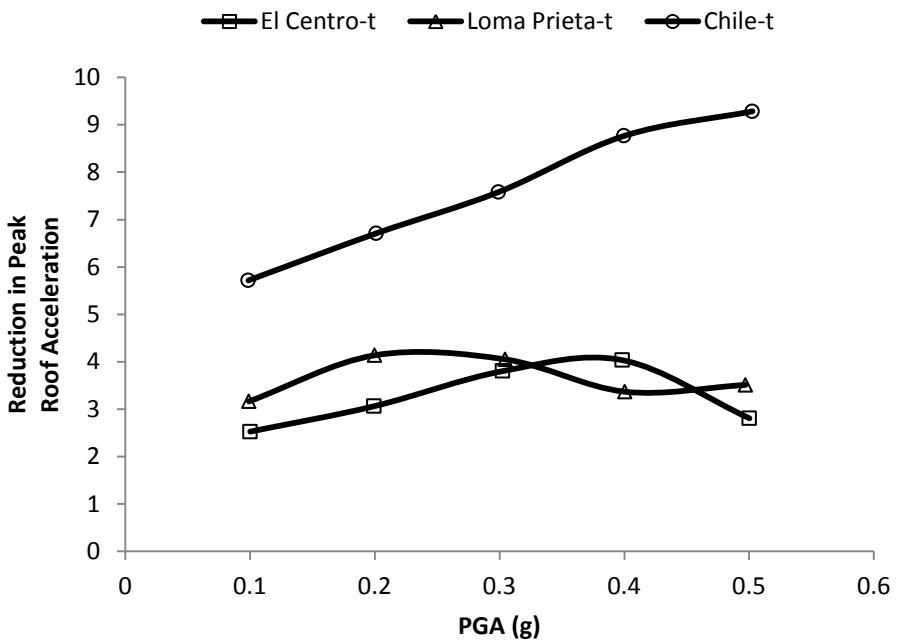

Figure 5.41 Reduction of peak roof acceleration response (FB/BI).

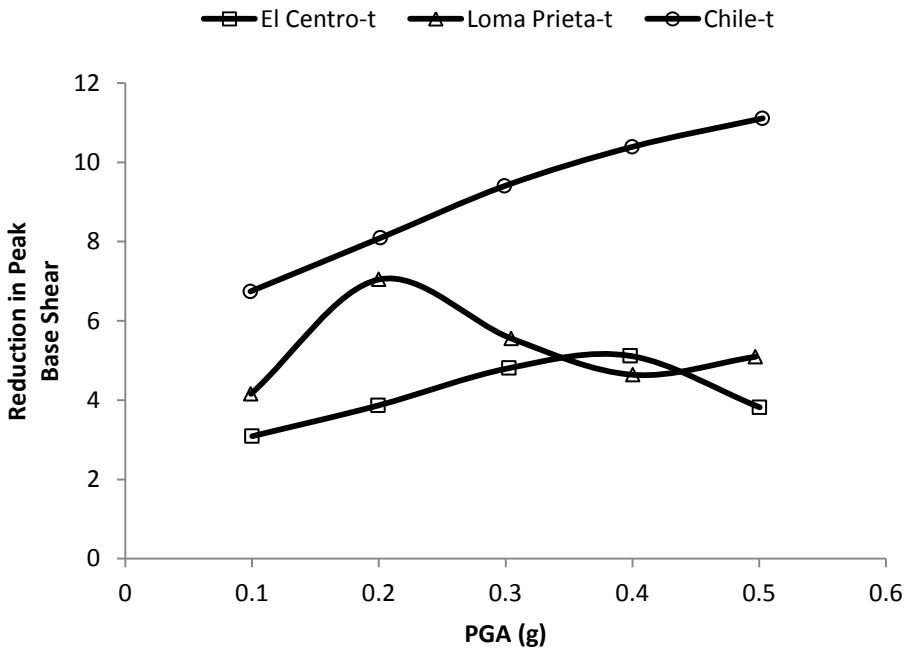

Figure 5.42 Reduction of peak base shear ratio response (FB/BI).

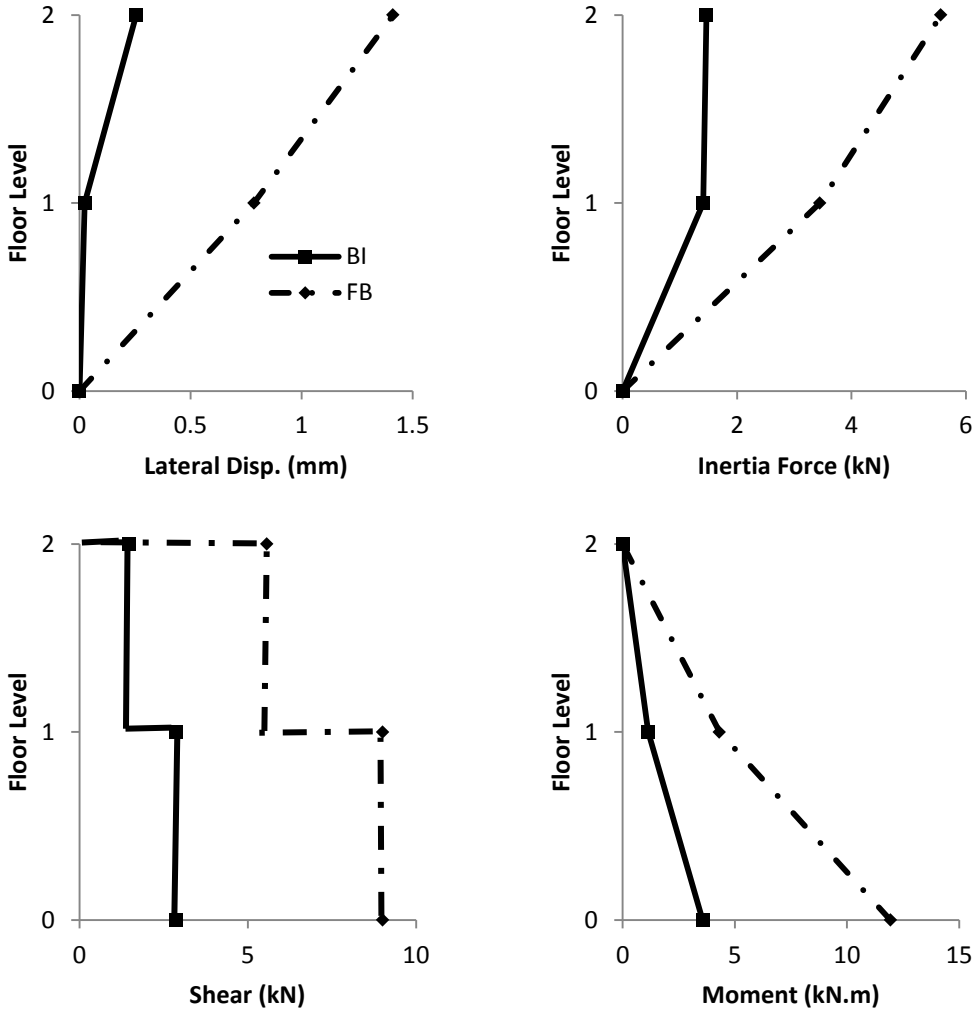

Figure 5.43 Response profiles of the BI-structure and the corresponding 5% damped linear FB-structure (0.3g PGA El Centro-t input earthquake).

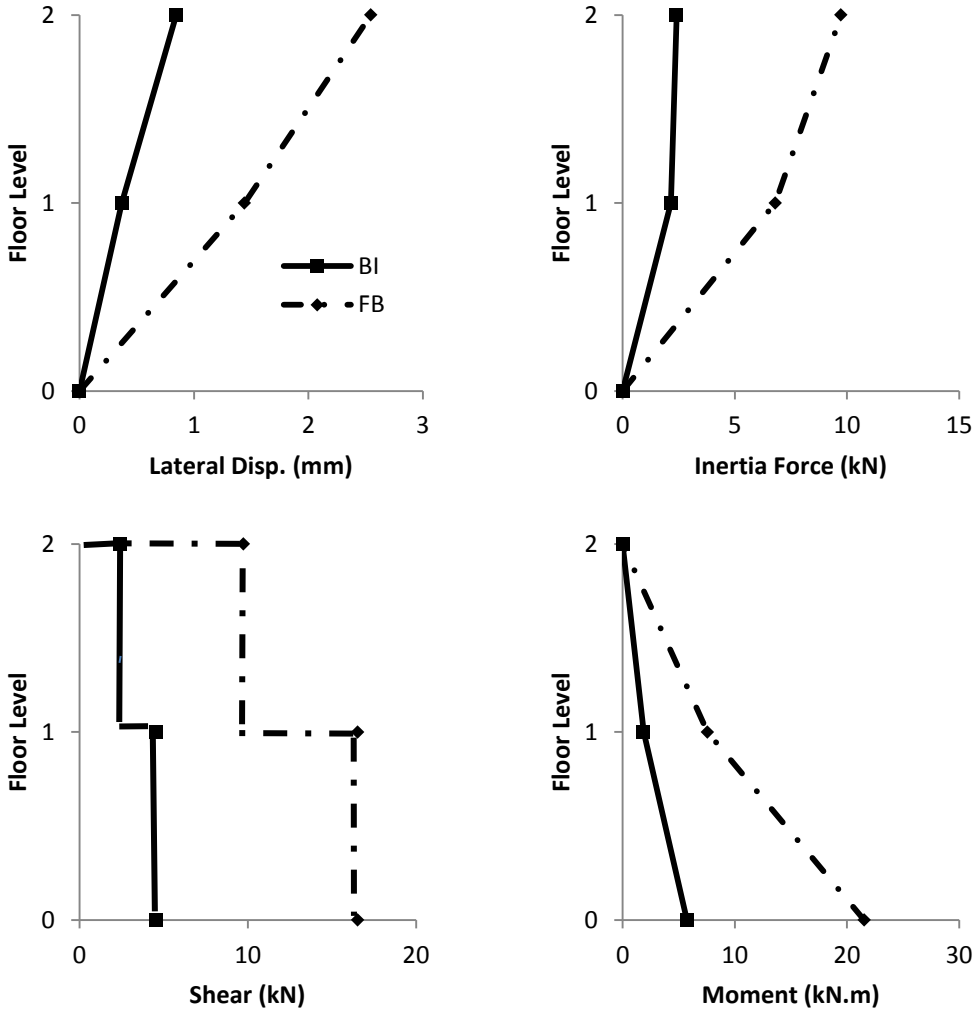

Figure 5.44 Response profiles of the BI-structure and the corresponding 5% damped linear FB-structure (0.3g PGA Loma Prieta-t input earthquake).

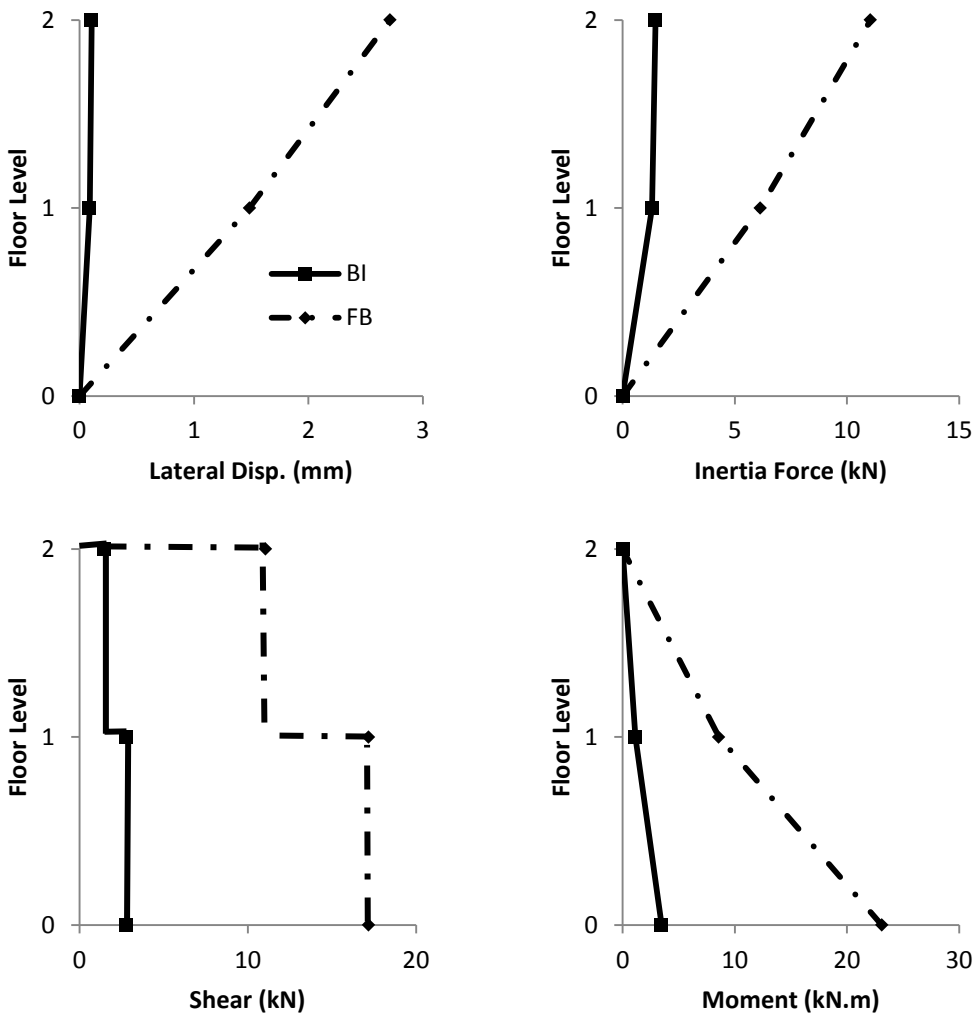

Figure 5.45 Response profiles of the BI-structure and the corresponding 5% damped linear FB-structure (0.3g PGA Chile-t input earthquake).

Chapter 6. Modelling of a SU-FREI Base Isolated (BI) Structure

6.1 Introduction

Two analytical models are presented and evaluated in this chapter. The analytical models are used to simulate the response behaviour of the SU-FREI base isolated structure that was experimentally investigated in Chapter 5. The bilinear model (BLM) and backbone curve model (BCM), which were presented in Chapter 4, are used to simulate the nonlinear lateral load-displacement behaviour of the SU-FREI base isolation system.

A three degree of freedom (3-DOF) model is used to represent the SU-FREI base isolated structure. An iterative time history analysis is conducted to select suitable model parameters that sufficiently represent the bearing behaviour corresponding to the peak bearing lateral displacement experienced by the bearings (Toopchi-Nezhad 2008). Model results are subsequently compared to measured results obtained from shake table tests of a SU-FREI base isolated structure (Chapter 5) to evaluate the analytical models.

6.2 Base Isolated Structural Model Description

6.2.1 Governing Equations

A 3-DOF system consisting of masses, springs and dashpots, shown in Figure 6.1, is used to model the response of the base isolated structure

investigated in Chapter 5. It is noted that the analysis in this study is strictly one-dimensional and neglects any out of plane components of motion, including the vertical component. Naiem and Kelly (1999) express the governing equation of the idealized system as

$$\boldsymbol{M}^*\ddot{\boldsymbol{V}}^* + \boldsymbol{C}^*\dot{\boldsymbol{V}}^* + \boldsymbol{K}^*\boldsymbol{V}^* = -\boldsymbol{M}^*\boldsymbol{r}^*\ddot{u}_g \qquad 6.1$$

where **M***, **C*** and **K*** are, respectively, the mass, damping and stiffness matrices of the base isolated structure, defined by Equation 6.2 – Equation 6.4.

$$\boldsymbol{M}^* = \begin{bmatrix} m + m_b & \boldsymbol{r}^T\boldsymbol{M} \\ \boldsymbol{M}\boldsymbol{r} & \boldsymbol{M} \end{bmatrix} \qquad 6.2$$

$$\boldsymbol{C}^* = \begin{bmatrix} c_b & \boldsymbol{0} \\ \boldsymbol{0} & \boldsymbol{C} \end{bmatrix} \qquad 6.3$$

$$\boldsymbol{K}^* = \begin{bmatrix} k_b & \boldsymbol{0} \\ \boldsymbol{0} & \boldsymbol{K} \end{bmatrix} \qquad 6.4$$

The mass matrix, $\boldsymbol{M}$**,** damping matrix, $\boldsymbol{C}$, and stiffness matrix, $\boldsymbol{K}$, represent the two-storey superstructure, m represents the total mass of the structure excluding the base floor ($m = m_1 + m_2$), m_b defines the mass of the base floor and c_b and k_b are the base isolation systems damping and stiffness values, which are determined experimentally (see Chapter 4). The remaining variables introduced in Equation 6.2 to Equation 6.4 are defined as follows (Equation 6.5 to Equation 6.8),

$$\boldsymbol{r} = \begin{Bmatrix} 1 \\ 1 \end{Bmatrix} \tag{6.5}$$

$$\boldsymbol{r}^* = \begin{Bmatrix} 1 \\ 0 \end{Bmatrix} \tag{6.6}$$

$$\boldsymbol{V}^* = \begin{Bmatrix} v_b \\ \boldsymbol{v} \end{Bmatrix} \tag{6.7}$$

$$\boldsymbol{v} = \begin{Bmatrix} v_1 \\ v_2 \end{Bmatrix} \tag{6.8}$$

6.2.2 Superstructure Model

Figure 6.2 represents a model of the superstructure, which has a total of 8 degrees of freedom (DOF). Using this model, the stiffness matrix, $\boldsymbol{K}$, of the superstructure can be formulated. Employing static condensation, as outlined by Chopra (2007), the matrix can be simplified by removing the rotational DOF from the dynamic analysis. Equation 6.9 shows the condensed form of $\boldsymbol{K}$ used in Equation 6.4.

$$\boldsymbol{K} = \boldsymbol{k}_{tt} - \boldsymbol{k}_{\theta t}^{T} \boldsymbol{k}_{\theta\theta}^{-1} \boldsymbol{k}_{\boldsymbol{\theta} t} \tag{6.9}$$

The matrices in Equation 6.9 are defined below in Equation 6.10 to Equation 6.12 and are based on the member properties of the two-storey superstructure.

$$\boldsymbol{k}_{tt} = 2\left(\frac{24EI_c}{L_c^3}\right)\begin{bmatrix} 2 & -1 \\ -1 & 1 \end{bmatrix} \tag{6.10}$$

$$\boldsymbol{k}_{\theta t}^T = 2\left(\frac{6EI_c}{L_c^2}\right)\begin{bmatrix} 1 & 1 & 0 & 0 & -1 & -1 \\ 0 & 0 & 1 & 1 & 1 & 1 \end{bmatrix} \tag{6.11}$$

$$\boldsymbol{k}_{\theta\theta} = 2(2E)\begin{bmatrix} \frac{2I_c}{L_c}+\frac{2I_b}{L_b} & \frac{I_b}{L_b} & \frac{I_c}{L_c} & 0 & 0 & 0 \\ & \frac{2I_c}{L_c}+\frac{2I_b}{L_b} & 0 & \frac{I_c}{L_c} & 0 & 0 \\ & & \frac{4I_c}{L_c}+\frac{2I_b}{L_b} & \frac{I_b}{L_b} & \frac{I_c}{L_c} & 0 \\ & & & \frac{4I_c}{L_c}+\frac{2I_b}{L_b} & 0 & \frac{I_c}{L_c} \\ & Sym. & & & \frac{2I_c}{L_c}+\frac{2I_b}{L_b} & \frac{I_b}{L_b} \\ & & & & & \frac{2I_c}{L_c}+\frac{2I_b}{L_b} \end{bmatrix} \tag{6.12}$$

The coefficient of 2 in front of each stiffness term accounts for the two parallel planar frames in the structure. Using a lumped mass idealization, the mass matrix of the superstructure is defined as

$$\boldsymbol{M} = \begin{bmatrix} m_1 & 0 \\ 0 & m_2 \end{bmatrix} \tag{6.13}$$

The damping matrix is derived assuming Rayleigh damping (Equation 6.14) (Chopra 2007).

$$\boldsymbol{C} = \alpha\boldsymbol{M} + \beta\boldsymbol{K} \tag{6.14}$$

Coefficients α and β are calculated using Equation 6.15 and Equation 6.16, respectively, which are a function of the damping ratio (ζ) and natural frequencies (ω_1 and ω_2) of the superstructure.

$$\alpha = \frac{2\zeta\omega_1\omega_2}{\omega_1 + \omega_2} \tag{6.15}$$

$$\beta = \frac{2\zeta}{\omega_1 + \omega_2} \tag{6.16}$$

The natural frequencies and damping ratio of the fixed base structure, defined from free vibration tests, are listed in Table 5-2.

6.2.3 Modelling of SU-FREI Bearings

Two previously introduced mathematical models, the bilinear model and backbone curve model, are used in the time history analysis (THA) of the isolated structure to model the behaviour of the isolation system. The models simulate the lateral force, $f_b(t)$, in the isolation system corresponding to a lateral displacement amplitude, v_b and displacement rate, $\dot{v}_b$, (Equation 6.17),

$$f_b(t) = k_b(t)v_b(t) + c_b(t)\dot{v}_b(t) \tag{6.17}$$

where $k_b(t)$ and $c_b(t)$ are the effective lateral stiffness and damping coefficient of the isolation system. Assuming n identical bearings, the stiffness and damping of the isolation system are expressed as

$$k_b = \sum_{i=1}^{n} k_{bi} \ and \ c_b = \sum_{i=1}^{n} c_{bi} \qquad 6.18$$

where the subscript i denotes an individual bearing. Both models use an iterative procedure that updates the isolation system properties based on the peak lateral displacement achieved in the previous simulation (Toopchi-Nezhad et al. 2009b). The procedures are shown below and were repeated until convergence was achieved within an error tolerance of 1% or less between successive runs. Convergence was achieved within three to seven iterations, on average, depending on amplitude and record.

6.2.3.1 Bilinear Model (BLM)

i. Parameters k_1, k_2 and q at 250%t_r lateral displacement are initial values used in the analysis

ii. $v_{b,max}$ is calculated based on the time history of the base isolated structure.

iii. New values of k_1, k_2 and q are calculated by linear interpolation between the bounding displacement amplitudes of $v_{b,max}$.

iv. $v_{b,max}$ is recalculated based on the time history analysis of the base isolated structure.

v. Steps ii-iv are repeated until $v_{b,max}$ converges to an acceptable error tolerance.

Table 4-1 contains the parameter k_1, k_2 and q used for the analysis at the respected displacement amplitude levels.

6.2.3.2 Backbone Curve Model (BCM)

i. Secant stiffness curve coefficient values for 250%t_r are used as initial values.

ii. $v_{b,max}$ is calculated based on the time history analysis of the base isolated structure.

iii. New secant stiffness coefficient values are calculated based on linear interpolation between the bounding stiffness coefficients obtained by the curve fits of the displacement amplitudes of cyclic testing.

iv. $v_{b,max}$ is again calculated based on the time history analysis of the base isolated structure.

v. Steps ii-iv are repeated until $v_{b,max}$ converges to an acceptable error tolerance.

Table 4-2 gives the coefficient values at the respected displacement amplitudes used for modelling purposes.

6.2.4 Bilinear Model Results

The normalized peak response results of the bilinear model are summarized in Table 6-1, Table 6-2 and Table 6-3, respectively, for the El Centro-t, Loma Prieta-t and Chile-t input earthquakes. The values are presented as

a ratio of the experimental data obtained from shake table testing performed in Chapter 5. The tabulated results show that the bilinear model was able to predict results within 23% for bearing lateral load, 21% for bearing lateral displacement and 28% for the base shear of the structure. The largest error for bearing lateral load corresponds to the Loma Prieta-t 0.4g PGA record. In fact, the PGA amplitudes that produced full vertical facial contact produced the largest errors, indicating that full facial contact diminishes the models ability to capture bearing forces (and subsequently base shears). The highest level of error for bearing lateral displacement corresponded to the 0.4g PGA El Centro-t record. Table 6-4 gives a summary of the average and standard deviation of errors for respected parameters and tests.

The time history response of bearing lateral displacement and lateral roof acceleration is shown in Figure 6.3 and Figure 6.4, respectively, for the 0.3g PGA Loma Prieta-t input earthquake. The figures show that the bilinear model is in good agreement with the measured response, particularly in the higher amplitude response regions of the time history.

The hysteresis loops acquired from the time history analyses are shown in Figure 6.5, Figure 6.6 and Figure 6.7 for 0.3g PGA El Centro-t, Loma Prieta-t and Chile-t, respectively. The figures also contain measured lateral load-displacement hysteresis loops for comparison. The figures show that the general shape and slope of the simulated hysteresis loops are similar to the simulated hysteresis

loops. In addition, simulated hysteresis loops show the stable rollover behaviour of the SU-FREI bearing.

6.2.5 Backbone Curve Model Results

The peak response values obtained from the backbone curve model are presented in Table 6-1, Table 6-2 and Table 6-3. The highest errors for bearing lateral load, lateral displacement and structure base shear are approximately 278%, 45% and 314%, respectively; correspond to earthquake records that produced displacement amplitudes in excess of 250%t_r. It is expected that the results of the backbone curve model with displacement amplitudes in excess of 250%t_r are not reflective of bearing properties, as the values are determined from extrapolation. Neglecting records that produce displacement amplitudes in excess of 250%t_r, the maximum errors are 26%, 35% and 27% for the bearing lateral load, lateral displacement and base shear, respectively.

The time history response of bearing displacement and roof acceleration are shown in Figure 6.8 and Figure 6.9, respectively, for 0.3g PGA Loma Prieta-t. The figures show that, like the bilinear model, the backbone curve model better estimates the measured response parameters in the higher response amplitude regions.

The hysteresis loops simulated by the backbone curve model are plotted in Figure 6.5, Figure 6.6 and Figure 6.7 for 0.3g PGA El Centro-t, Loma Prieta-t and Chile-t, respectively. The general shape and slope of the simulated hysteresis loops are similar to the measured hysteresis loops.

The average error and standard deviation of the errors for both models are provided in Table 6-4. Records producing displacement amplitudes beyond $250\%t_r$ are omitted, as the analysis does not accurately reflect bearing performance and subsequently the model should not be used beyond the limits of interpolation. The increased accuracy of the bilinear model is shown in Figure 6.10, which displays a three-dimensional bar chart of the error of predicted bearing lateral displacement with respect to the PGA amplitudes of input records. The figure shows that the errors in lateral displacement are not amplitude dependent as Chile-t and Loma Prieta-t have low errors at higher amplitudes. This implies that the errors are, to some extent, dependent on the input excitation.

6.3 Summary and Conclusion

In summary, thirty time history analyses were performed using the bilinear and backbone curve SU-FREI bearing models discussed in Chapter 4. The models selected are adequate in predicting the general temporal response of the bearing and structure. The bilinear model matched experimental results more accurately than the backbone curve model. This is shown by the average error and standard deviation of the two models in Table 6-4 and again in the error of bearing lateral displacements shown in Figure 6.10.

The simulated hysteresis loops show that both models are able to provide good estimates in term of general shape and slope compared to the measured hysteresis loops.

It was found in the study that the backbone curve model produced large errors of peak value response parameters compared to the measured data as displacement amplitudes exceeded 250%t_r. The large errors were a result of the model extrapolating bearing properties based on the 5th order polynomial. The backbone curve model is suggested only to be used within the range of the measured data.

Overall, the bi-linear model provided more precise and accurate prediction of response parameter values for all considered events. Given the simplified nature of the models and their ability to provide satisfactory results, the models could be used in preliminary analysis and design of low-rise base isolated structures.

Table 6-1 Experimental and normalized THA response parameters for El Centro-t earthquake records.

PGA (g)	Response	Bearing Lateral Load	Bearing Lateral Displacement	Base Shear
0.1	Experimental	0.56kN	6.49mm	1.51kN
	BLM/Exp.	0.97	1.05	0.99
	BCM/Exp.	0.74	0.92	0.73
0.2	Experimental	0.86kN	12.76mm	2.37kN
	BLM/Exp.	0.92	0.95	0.92
	BCM/Exp.	0.84	1.12	0.83
0.3	Experimental	1.05kN	18.60mm	2.81kN
	BLM/Exp.	0.97	1.10	1.05
	BCM/Exp.	0.94	1.31	0.96
0.4	Experimental	1.26kN	27.66mm	3.40kN
	BLM/Exp.	1.02	1.21	1.03
	BCM/Exp.	0.98	1.22	0.99
0.5	Experimental	1.87kN	39.14mm	5.41kN
	BLM/Exp.	0.91	1.19	0.88
	BCM/Exp.	2.47	1.45	2.39

Table 6-2 Experimental and normalized THA response parameters for Loma Prieta-t earthquake records.

PGA (g)	Response	Bearing Lateral Load	Bearing Lateral Displacement	Base Shear
0.1	Experimental	0.72kN	9.26mm	1.95kN
	BLM/Exp.	1.01	1.11	1.05
	BCM/Exp.	0.99	1.28	1.00
0.2	Experimental	1.10kN	20.45mm	3.00kN
	BLM/Exp.	0.99	1.11	1.02
	BCM/Exp.	0.91	1.10	0.90
0.3	Experimental	1.59kN	36.52mm	4.47kN
	BLM/Exp.	0.85	0.99	0.83
	BCM/Exp.	0.83	1.01	0.82
0.4	Experimental	2.30kN	48.16mm	6.68kN
	BLM/Exp.	0.77	0.99	0.72
	BCM/Exp.	1.00	1.04	0.98
0.5	Experimental	2.71kN	59.16mm	7.28kN
	BLM/Exp.	0.80	1.01	0.80
	BCM/Exp.	3.79	1.14	4.14

Table 6-3 Experimental and normalized THA response parameters for Chile-t earthquake records.

PGA (g)	Response	Bearing Lateral Load	Bearing Lateral Displacement	Base Shear
0.1	Experimental	0.45kN	5.01mm	1.22kN
	BLM/Exp.	0.99	1.04	1.04
	BCM/Exp.	0.96	1.25	0.95
0.2	Experimental	0.74kN	10.23mm	2.08kN
	BLM/Exp.	1.07	1.18	1.11
	BCM/Exp.	0.93	1.12	0.91
0.3	Experimental	0.97kN	16.03mm	2.70kN
	BLM/Exp.	0.97	1.03	0.96
	BCM/Exp.	0.96	1.35	0.92
0.4	Experimental	1.21kN	25.07mm	3.31kN
	BLM/Exp.	0.98	1.09	1.00
	BCM/Exp.	0.85	1.15	0.86
0.5	Experimental	1.42kN	33.31mm	3.92kN
	BLM/Exp.	0.92	1.01	0.96
	BCM/Exp.	0.90	1.04	0.94

Table 6-4 Statistics of the THA error for the BLM and BCM Models.

Parameter	Statistic	Model	El Centro-t	Loma Prieta-t	Chile-t
Bearing Lateral Load	Average Error (%)	BLM	4.0	11.5	1.4
		BCM	12.5	9.0	8.1
	Standard Deviation of Error (%)	BLM	3.8	10.1	5.0
		BCM	9.2	6.3	4.2
Bearing Lateral Displacement	Average Error (%)	BLM	-10.0	-4.3	-7.1
		BCM	-14.0	-13.1	-18.3
	Standard Deviation of Error (%)	BLM	9.6	5.4	6.1
		BCM	14.6	11.3	11.0
Base Shear	Average Error (%)	BLM	2.7	11.5	-1.2
		BCM	12.5	9.2	8.6
	Standard Deviation of Error (%)	BLM	6.4	12.9	5.7
		BCM	10.2	7.3	3.2

Note: The El Centro-t 0.5g and Loma Prieta 0.4 and 0.5g PGA records are not included in the averages or standard deviations.

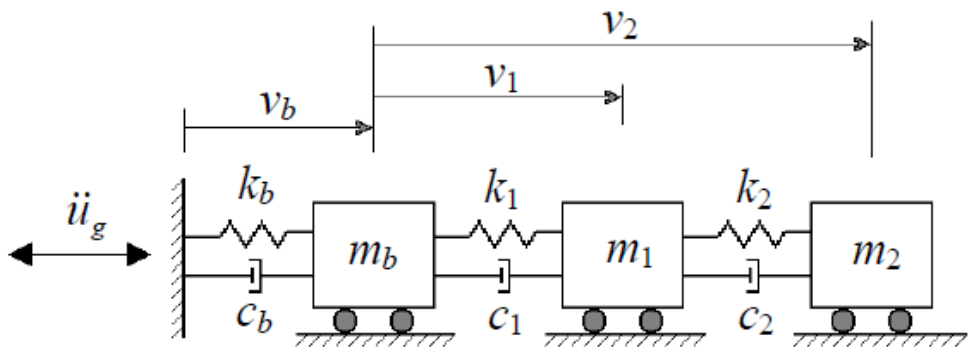

Figure 6.1 Mass-spring-dashpot idealization of the base isolated structure (Toopchi-Nezhad et al. 2009b).

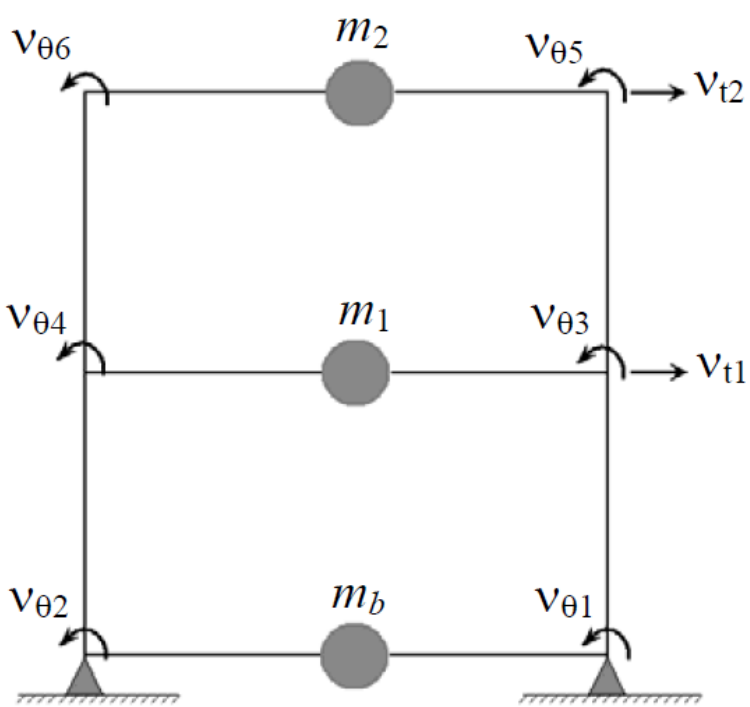

Figure 6.2 Stick model of an idealized lumped mass structure displaying the translational (dynamic) and rotational (static) degrees of freedom of the structure (Toopchi-Nezhad et al. 2009b).

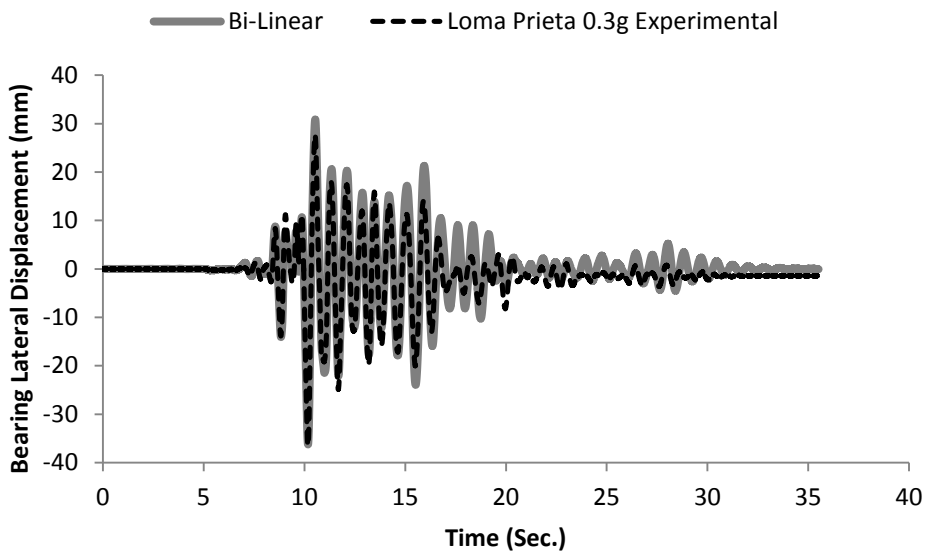

Figure 6.3 Measured versus predicted (bilinear model) bearing lateral displacement for 0.3g PGA Loma Prieta-t.

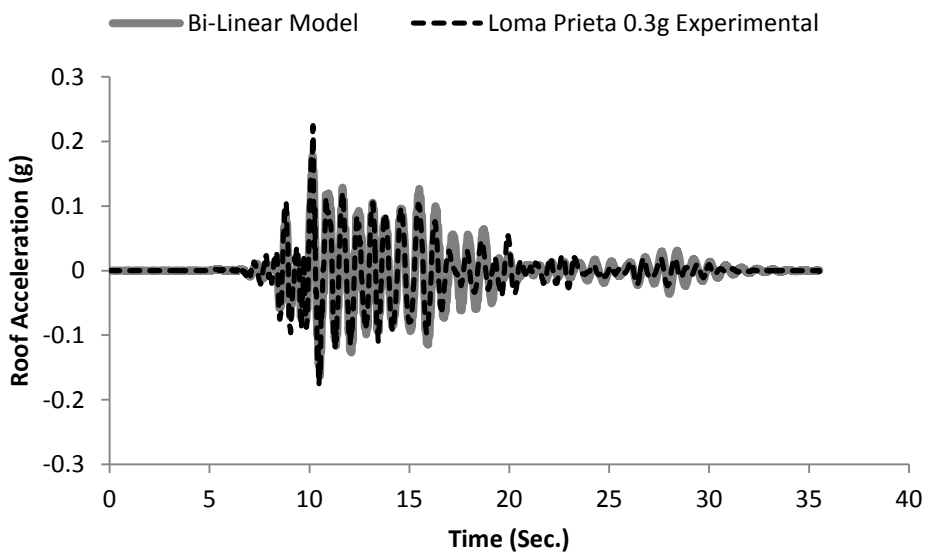

Figure 6.4 Measured versus predicted (bilinear model) roof acceleration for 0.3g PGA Loma Prieta-t.

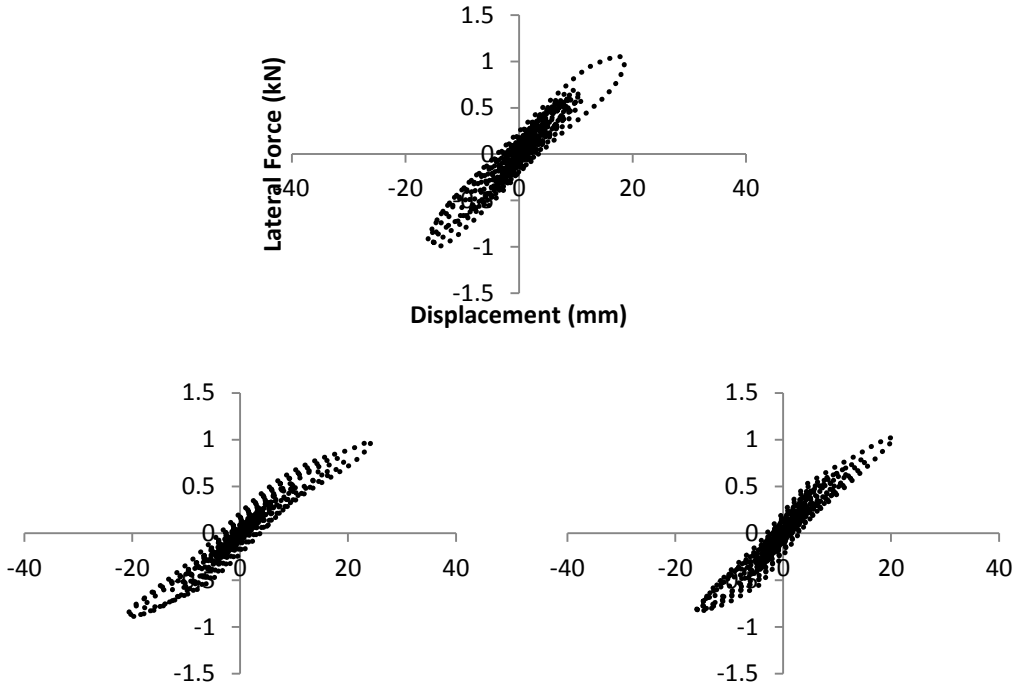

Figure 6.5 Measured (Top) 0.3g PGA El Centro-t hysteresis loops compared with predicted (left) backbone curve model, (right) bilinear model hysteresis loops.

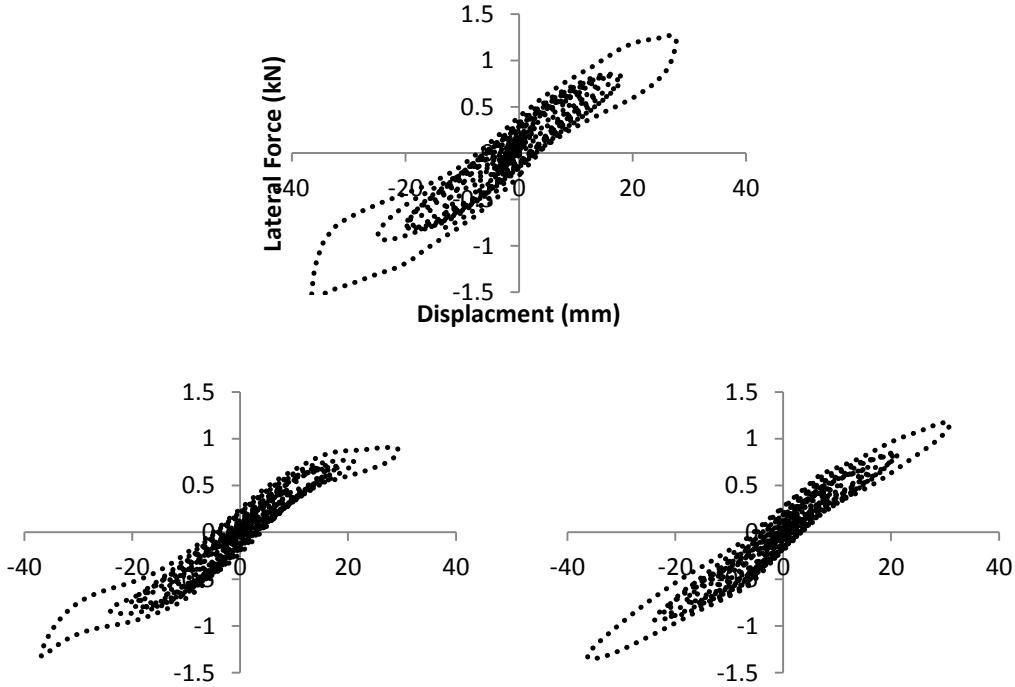

Figure 6.6 Measured (Top) 0.3g PGA Loma Prieta-t experimental hysteresis loops compared with predicted (left) backbone curve, (right) bilinear models hysteresis loops.

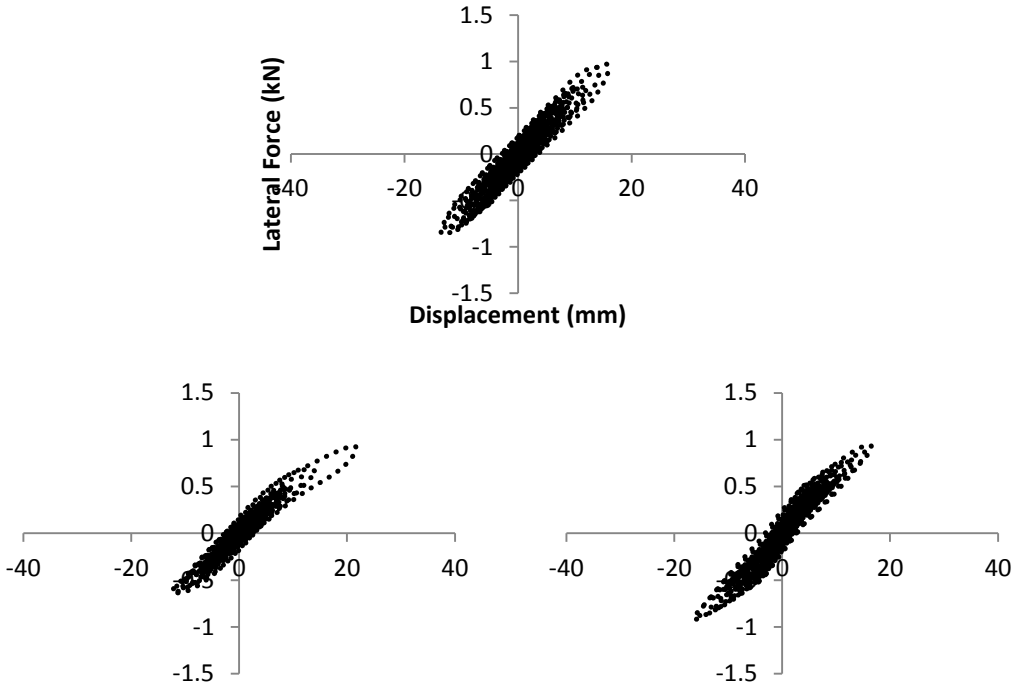

Figure 6.7 Measured (Top) 0.3g PGA Chile-t hysteresis loops compared with predicted (left) backbone curve model (right) bilinear models hysteresis loops.

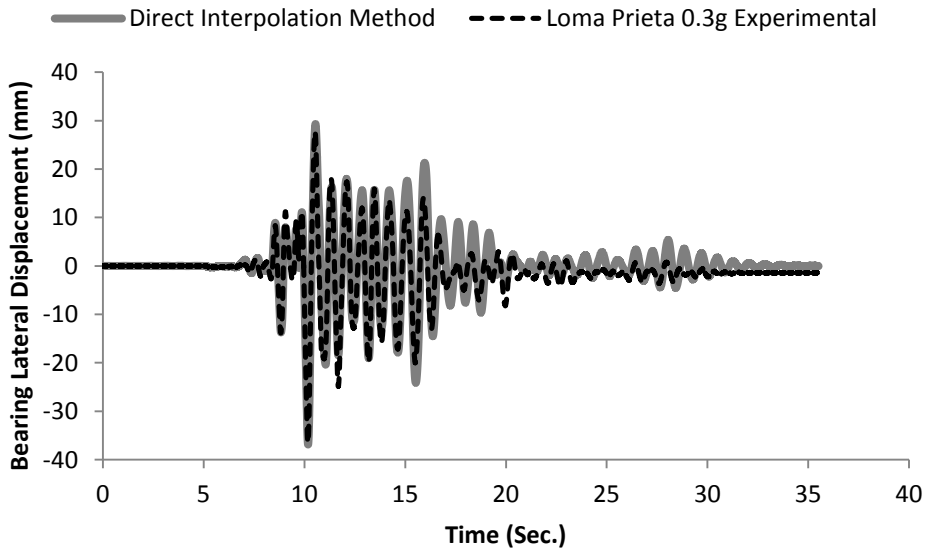

Figure 6.8 Measured versus predicted (backbone curve model) bearing lateral displacement for 0.3g PGA Loma Prieta-t

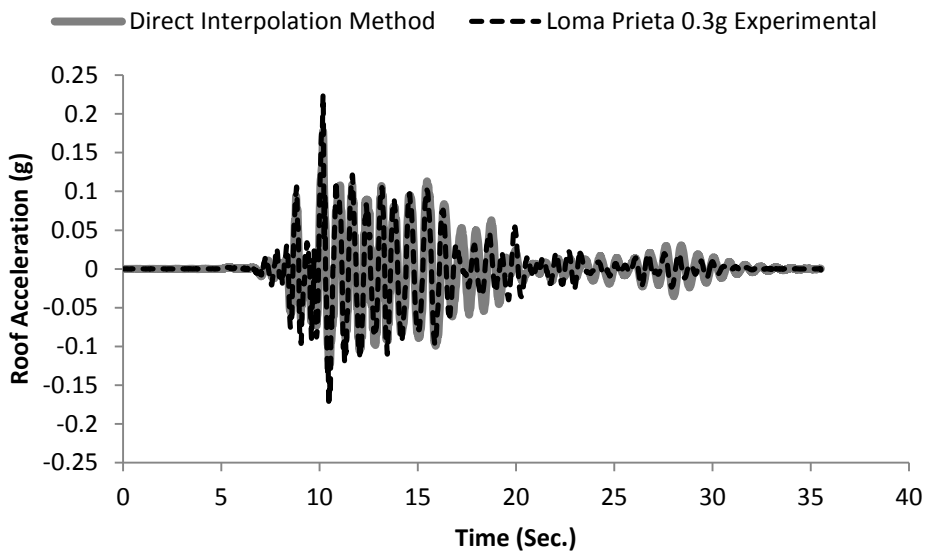

Figure 6.9 Measured versus predicted (backbone curve model) roof acceleration for 0.3g PGA Loma Prieta-t

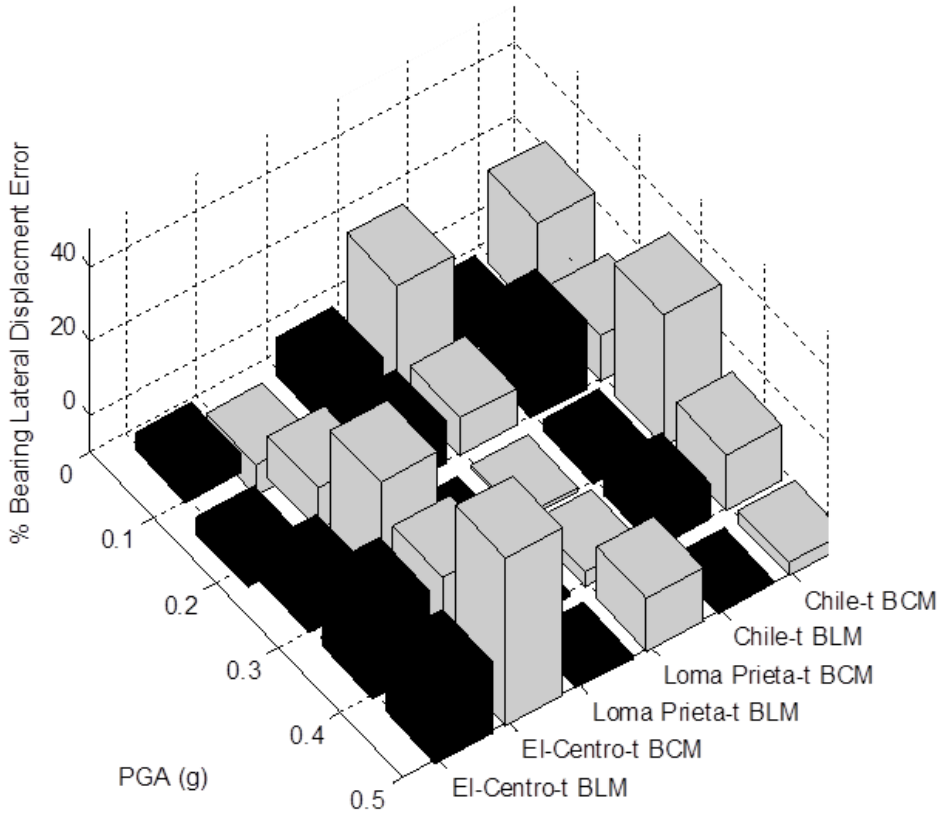

Figure 6.10 3D bar chart displaying the lateral displacement percent error of each THA with respect to each PGA level.

Chapter 7. Design Spectrum and Time History Analysis Predictions

7.1 Introduction

The purpose of a stable unbonded fibre reinforced elastomeric isolator (SU-FREI) base isolation system is to provide an efficient and economical means of protecting the structure from the effects of seismic excitation. A SU-FREI bearing uses carbon fibre fabric reinforcement instead of steel shims. As a result, the mechanics of the isolator become more complex due to the rollover effect caused by the unbonded contact surface and the lack of flexural rigidity of the fibre. For SU-FREI base isolation systems to become viable, a simple and effective analysis method is required to predict the isolated structural response. Chapter 6 illustrated the use of a time history analysis (THA) procedure to predict structural response. However, this may not be a practical preliminary analysis technique, as a time history analysis can be both time consuming and computationally demanding. Therefore, an alternative method for preliminary analysis of a SU-FREI base isolation system is necessary. Building codes typically employ a design spectrum approach for the seismic design of structures. It has been shown that a design spectrum method can also be applied to SU-FREI isolation systems (Tait et al. 2011). Using this method, a design spectrum from current building codes may be used for preliminary analysis.

7.2 Design Spectrum Procedure

In order for the analysis of the two-storey base isolated structure (shown in Figure 7.1(a) to be completed using a design spectrum approach, it must first be modeled as a single degree of freedom (1-DOF) system. This can be accomplished by idealizing the structure as a solid mass, M, connected to the ground by a spring, K_b, and dashpot, C_b. The properties of the idealized spring and dashpot are obtained from effective stiffness and damping values of the SU-FREI bearings comprising the isolation system. A visual representation of the two-storey base isolated structure is shown in Figure 7.1b, where $\ddot{u}_g$ is the ground acceleration, v_b is the lateral displacement of the SU-FREI isolation system, k_b and c_b are the stiffness and damping coefficient of the isolation system, respectively, and m_b, m_1, m_2 are the floor masses. This single degree of freedom idealization is a valid assumption as a result of the rigid body motion experienced by the base isolated structure, as discussed in Chapter 5.

A design spectrum analysis is straightforward and efficient to use, as design spectra can be rapidly developed for a particular location using code specified spectral acceleration ordinates. Design spectra are typically given in accordance to a 5% damped structure; however, it has been shown that SU-FREI bearings provide damping in excess of 5%. Therefore, a method to compensate for the idealized damping is needed. Numerous reduction factors to account for increased damping have been suggested and evaluated (Cardone et al. 2009). For

the procedure presented in this study a damping modification factor developed by Newmark and Hall (1973) is applied as follows,

$$S_a(T,\zeta) = \eta S_a(T, 5\%) \qquad 7.1$$

where $S_a(T,\zeta)$ is the adjusted design spectrum, $S_a(T, 5\%)$ is the 5% damped code specified design response spectrum, T is the period, ζ is the damping ratio and η is the damping modification factor expressed as

$$\eta = 1.4 - 0.248\ln(\zeta) \qquad 7.2$$

Due to the nonlinear stiffness behaviour exhibited by SU-FREI bearings, the period of the isolation system is a function of the displacement amplitude experienced by the bearings. To account for the nonlinearity of the system an iterative approach is employed. The step-by-step analysis procedure is as follows (Tait et al. 2011):

i. Assume an initial lateral displacement value of the isolation system, x.

ii. Evaluate the lateral force, F_s, in the isolation system corresponding to the displacement, x, using the force envelop, shown in Figure 7.2.

$$F_s = (c_4x^5 + c_3x^4 + c_2x^3 + c_1x^2 + c_0x)n \qquad 7.3$$

where n is the number of bearings.

iii. Calculate the lateral secant stiffness

$$K_{s,eff} = (c_4x^4 + c_3x^3 + c_2x^2 + c_1x + c_0)n \qquad 7.4$$

iv. Calculate the effective period (T).

$$T = 2\pi\sqrt{\frac{M}{K_{s,eff}}} \qquad 7.5$$

v. Evaluate the effective damping ratio, ζ, of the isolation system from the damping ratio envelop, shown in Figure 7.3.

$$\zeta = a_2x^2 + a_1x + a_0 \qquad 7.6$$

vi. Determine the code specified spectral acceleration, $S_a(T, 5\%)$.

vii. Compute the damping correction factor, η and apply to $S_a(T, 5\%)$ (Equation 7.2 and Equation 7.1).

viii. Update the bearing lateral displacement, x.

$$x = s_a\left(\frac{T}{2\pi}\right)^2 \qquad 7.7$$

ix. Repeat steps ii to viii until the lateral force F_s, converges to a unique value with an acceptable error tolerance.

The c parameters in Equation 7.4 are the coefficients of a 5th order polynomial fit to the unscragged force displacement curve shown in Figure 7.2, where the force values correspond to the values at maximum displacement. It should be noted that this curve is not the backbone curve presented in Chapter 4. The a parameters in Equation 7.6 are obtained from a second order fit to the average damping values of the three cycles, both scragged and unscragged, at each displacement amplitude (shown in Figure 7.3).

7.3 Case Study

In order to demonstrate the use of the design spectrum analysis procedure, the analysis is performed on the two-storey structure, studied in Chapter 5 and Chapter 6, in four different seismic regions of Canada. The site locations selected are Vancouver, Victoria, Montreal and Ottawa. Design spectrum analysis is performed on both the base isolated structure and fixed base structure to evaluate the efficiency of the SU-FREI isolation system. The results of the design spectrum analysis for the base isolated structure will also be compared with time history analysis results to evaluate the adequacy of the design spectrum method. The input earthquake records for the time history analysis will be design spectrum matched acceleration time histories of El Centro and Loma Prieta for the 2% in 50-year (2475 year return period) level maximum earthquake motion. This level is referred to as the design ground motion (DGM) by the NBCC (2010) and the maximum considered earthquake (MCE) by ASCE 7 (2005). Note, the results of the analyses in this study are presented in full scale.

7.3.1 Design Response Spectra and Earthquake Response Spectra

The design response spectra used for the analysis were created from the spectral acceleration values given in NBCC (2010). The spectral acceleration ordinates were adjusted to a site class D (stiff soil) ground condition. The site class adjusted spectral values taken from the code were then used in accordance

with the ASCE 7 (2005) method to develop a design spectrum given by Equations 7.8 to Equation 7.10 for the respected period ranges,

$$S_a = S_{DS}\left(0.4 + 0.6\frac{T}{T_0}\right), \qquad T < T_0 \tag{7.8}$$

$$S_a = S_{DS}, \qquad T_0 \leq T \leq T_S \tag{7.9}$$

$$S_a = \frac{S_{D1}}{T}, \qquad T > T_S \tag{7.10}$$

where S_a, is the design spectral response acceleration, S_{DS} is the spectral response acceleration parameter at short periods, S_{D1} is the spectral response acceleration parameter at 1 second and T is the fundamental period of the structure. The design spectral acceleration parameters are given by Equation 7.11 and Equation 7.12,

$$S_{DS} = \frac{2}{3}S_{MS} \tag{7.11}$$

$$S_{D1} = \frac{2}{3}S_{M1} \tag{7.12}$$

where S_{MS} is the MCE site class adjusted spectral response acceleration at short periods and S_{M1} is the MCE site class adjusted spectral response acceleration at a period of 1 second. The parameters T_0 and T_S are defined by Equation 7.13 and Equation 7.14.

$$T_0 = 0.2\,\frac{S_{D1}}{S_{DS}} \qquad 7.13$$

$$T_S = \frac{S_{D1}}{S_{DS}} \qquad 7.14$$

It should be noted that the spectral accelerations produced from Equation 7.8 to Equation 7.10 correspond to the ASCE 7 (2005) design basis earthquake (DBE) and must be multiplied by 1.5 to obtain the 2% in 50-year MCE spectrum. The ASCE 7 (2005) procedure to develop design response spectra was used as a substitute to the NBCC method for purposes of convergence when matching earthquake response spectra to design response spectra using the commercially available software package SeismoMatch (Seismosoft 2011). Figure 7.4 to Figure 7.7 compare the NBCC (2010) and ASCE 7 (2005) design spectra for the locations considered in this study. It can be observed that in the fixed base and base isolated range of interest, the design response spectra are in good agreement. The earthquake records matched to the design spectra were the original El Centro and Loma Prieta records introduced in Chapter 5. Figure 7.8 to Figure 7.11 show a graphical representation of both the ASCE 7 (2005) design response spectra and the matched response spectra of El Centro and Loma Preita, respectively, for Vancouver, Victoria, Montreal and Ottawa.

7.3.2 Results of Design Spectrum Analysis

The design spectrum analysis was completed for both the full-scale base isolated structure and two-storey fixed base structure. Response parameters were

calculated for both the DBE and MCE. The results of the analyses are presented in Table 7-1 and Table 7-2, respectively, for the base isolated and fixed base structures. The ratios of base isolated and fixed base period, T, spectral acceleration, S_a, and base shear, V_b, are given in Table 7-3. The results presented in the tables show that the isolation system significantly reduced the seismic demand for all of the locations considered in the study. The lowest level of reduction found was for that of Vancouver with a 66% reduction in the base shear at the MCE. The highest reduction in base shear was 79% for the Montreal MCE. The reduction in spectral acceleration and base shear was larger for the DBE than the MCE in Vancouver and Victoria. This is due to the displacement amplitudes of the bearings exceeding 201%t_r for MCE records, resulting in full vertical facial contact.

7.3.3 Time History Analysis (THA)

The normalized results of the time history analysis with respect to the design spectrum analysis are shown in Table 7-4. The time history analyses were completed using the procedures discussed in Chapter 6. The bearing model used for the analyses in this study was the bilinear model as it was found to produce more accurate estimates of response.

The data in Table 7-4 shows that the design spectrum method gives a maximum error of 20% with respect to base shear results of the time history analysis. Reasonable estimates of bearing displacement were achieved for Vancouver and Victoria using the design spectrum method. The displacement

amplitude results of the design spectrum method showed maximum overestimates of 6% for Victoria and 13% for Vancouver compared to time history analysis values. The results for Vancouver and Victoria were conservative estimates as the response spectrum approach overestimated both the displacements and base shear.

For the case of Montreal and Ottawa, the results of base shear were higher for the time history analysis compared to the spectrum method. The highest discrepancy of base shear was 8% corresponding to the El Centro record matched to the design spectrum for Montreal. The displacements obtained from the response spectrum procedure were also found to be conservative for Montreal and Ottawa. The design spectrum procedure produced a displacement ratio that was 36% higher than the time history analysis for the Loma Prieta record matched to the design response spectrum for Ottawa.

7.4 Summary and Conclusion

In summary, a simplified design spectrum analysis for the design of base isolated structures is presented and evaluated for four Canadian cities. The results for the base isolated structures were compared to results for a fixed base structure using the design spectrum analysis. The comparison allowed the seismic response ratio of the SU-FREI isolation system to be evaluated. The SU-FREI isolation system increased the structural period of the fixed base structure by a maximum factor of 8.6 and a minimum of 6.6. The large increases in period lead to a spectral acceleration reduction of 86% for Montreal subjected to a MCE, the

largest reduction achieved for any city considered. The largest base shear reduction was 79% (Ottawa) and the lowest reduction was 66% (Vancouver). The values show the SU-FREI isolation system is capable of mitigating seismic demand caused by strong ground motions.

Design spectrum analysis results were also compared to values obtained from time history analysis using the bilinear model introduced in Chapter 4. The input earthquake records used for the time history analysis had their acceleration spectra matched to those of the design spectrum for each city. The results of the time history analyses were found to be in reasonable agreement with those of the design spectrum analysis. The design spectrum analysis showed overestimates for both displacements and base shear for the west coast cities (Vancouver and Victoria); whereas the eastern cities produced conservative displacements but slightly non-conservative base shear estimates.

In conclusion, the analyses in this chapter show that a SU-FREI isolation system is effective in reducing seismic demand on a structure and that the design spectrum analysis procedure outlined in this chapter can be applied to SU-FREI isolated structures. The application of the analysis method is suggested for preliminary analysis of SU-FREI base isolated structures.

Table 7-1 Summary of BI-structures response parameters from design spectrum analysis.

Parameter	Vancouver		Victoria		Montreal		Ottawa	
	Design	Maximum	Design	Maximum	Design	Maximum	Design	Maximum
T(s)	1.87	1.78	1.87	1.76	1.44	1.59	1.43	1.61
S_a(g)	0.132	0.217	0.136	0.230	0.077	0.101	0.076	0.103
V_b(kN)	67.7	111.3	69.7	118.1	39.8	51.9	39.0	52.8
x/t_r	1.50	2.23	1.55	2.33	0.52	0.83	0.51	0.86
ζ(%)	8.03	7.47	7.98	7.40	8.91	8.61	8.93	8.58

Table 7-2 Summary of FB-structures response parameters from design spectrum analysis.

Parameter	Vancouver		Victoria		Montreal		Ottawa	
	Design	Maximum	Design	Maximum	Design	Maximum	Design	Maximum
T(s)	0.217	0.217	0.217	0.217	0.217	0.217	0.217	0.217
S_a(g)	0.645	0.968	0.880	1.320	0.488	0.732	0.488	0.732
V_b(kN)	221.0	331.4	301.3	452.0	167.1	250.7	167.1	250.7

Table 7-3 Seismic response ratio values.

Parameter	Vancouver		Victoria		Montreal		Ottawa	
	Design	Maximum	Design	Maximum	Design	Maximum	Design	Maximum
T_{BI}/T_{FB}	8.62	8.20	8.62	8.11	6.64	7.33	6.59	7.42
S_{aBI}/S_{aFB}	0.20	0.22	0.15	0.17	0.16	0.14	0.16	0.14
V_{bBI}/V_{bBI}	0.31	0.34	0.23	0.26	0.24	0.21	0.23	0.21

Table 7-4 Comparison of the bilinear model THA response to the design spectrum analysis results.

Parameter		T(s)	V_b(kN)	x/t_r
Vancouver	El Centro/Spectrum	1.06	0.80	0.87
	Loma/Spectrum	1.07	0.89	0.96
Victoria	El Centro/Spectrum	1.08	0.83	0.94
	Loma/Spectrum	1.08	0.86	0.95
Montreal	El Centro/Spectrum	0.90	1.08	0.80
	Loma/Spectrum	0.86	1.06	0.67
Ottawa	El Centro/Spectrum	0.88	1.06	0.77
	Loma/Spectrum	0.85	1.05	0.64

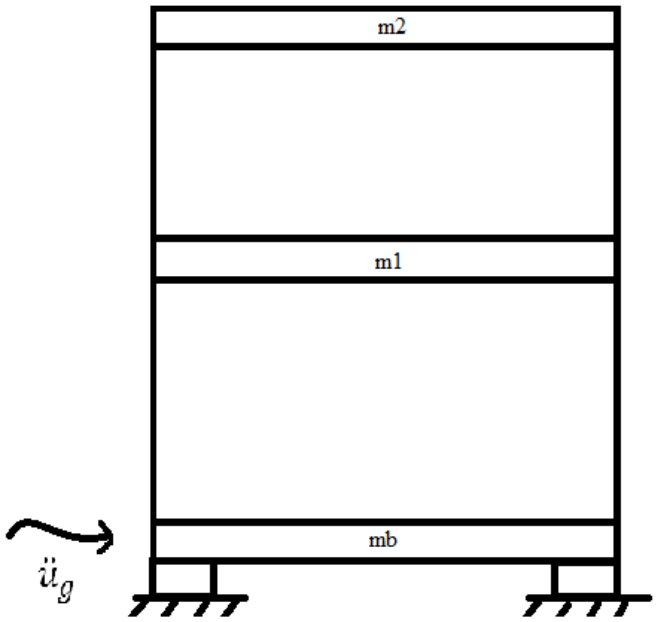

(a)

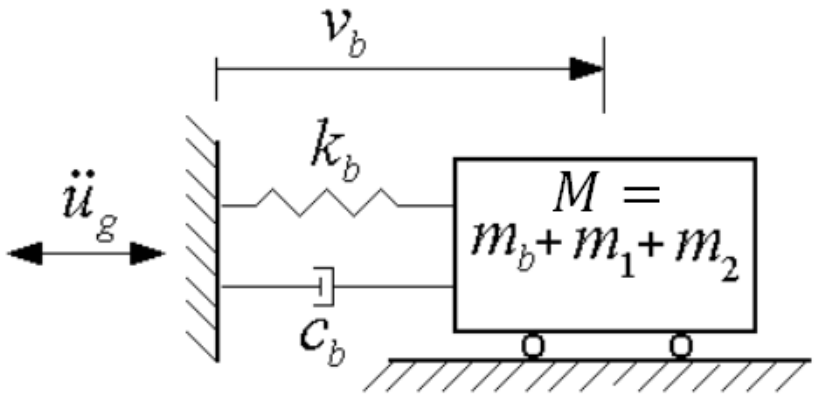

(b)

Figure 7.1 (a) Base isolated structure and (b) single degree of freedom (1 DOF) mass-spring-dashpot idealization (Tait et al. 2011).

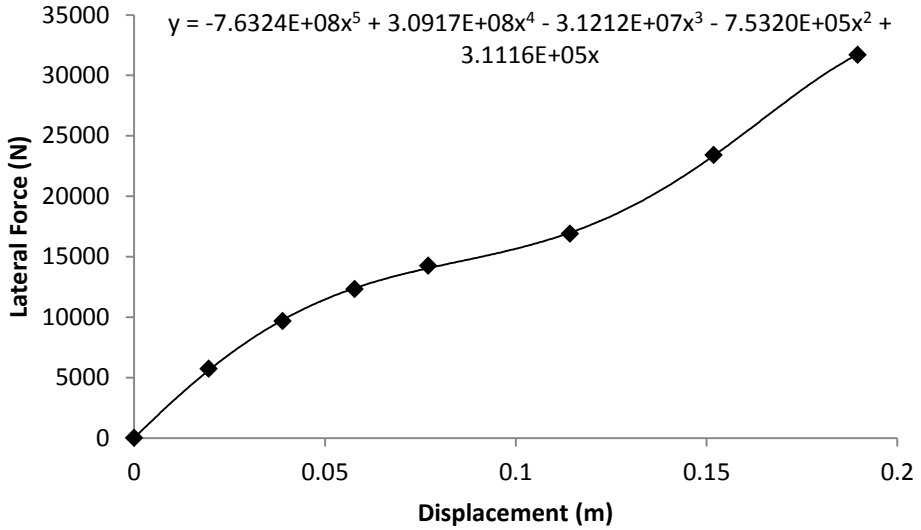

Figure 7.2 Force envelop used to evaluate the lateral force and stiffness of the system for the design spectrum analysis.

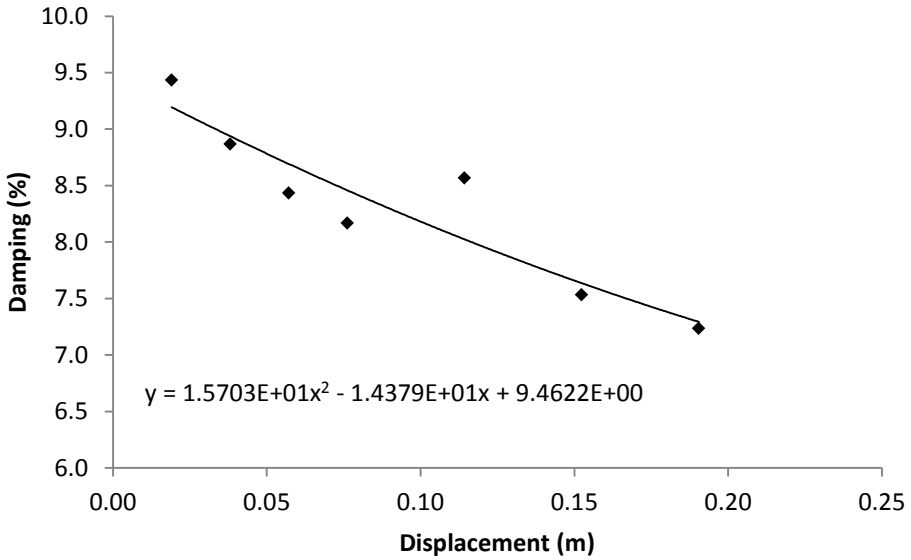

Figure 7.3 Damping envelop used for the evaluation of the system's damping in the design spectrum analysis.

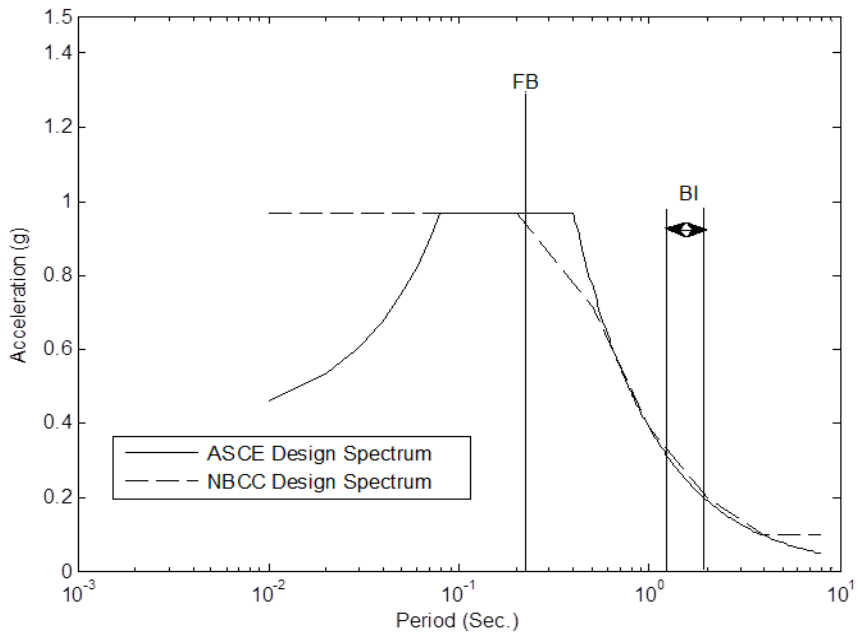

Figure 7.4 ASCE MCE and NBCC DGM design response spectrum for Vancouver, Canada, site class D.

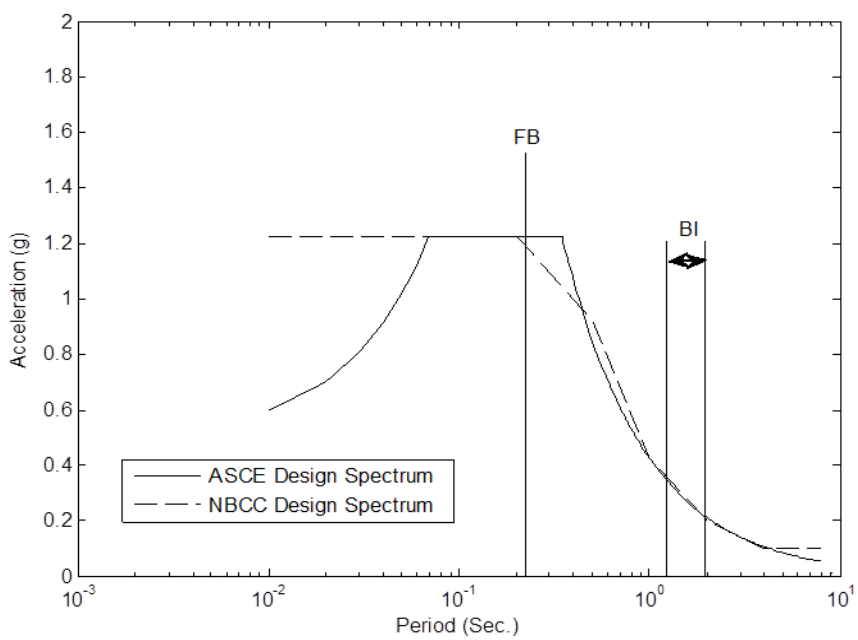

Figure 7.5 ASCE MCE and NBCC DGM design response spectrum for Victoria, Canada, site class D.

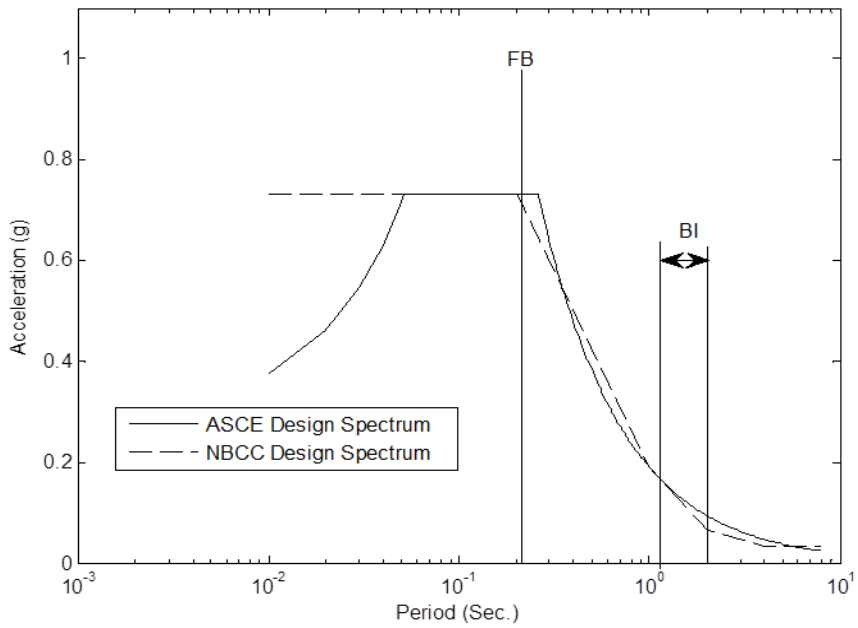

Figure 7.6 ASCE MCE and NBCC DGM design response spectrum for Montreal, Canada, site class D.

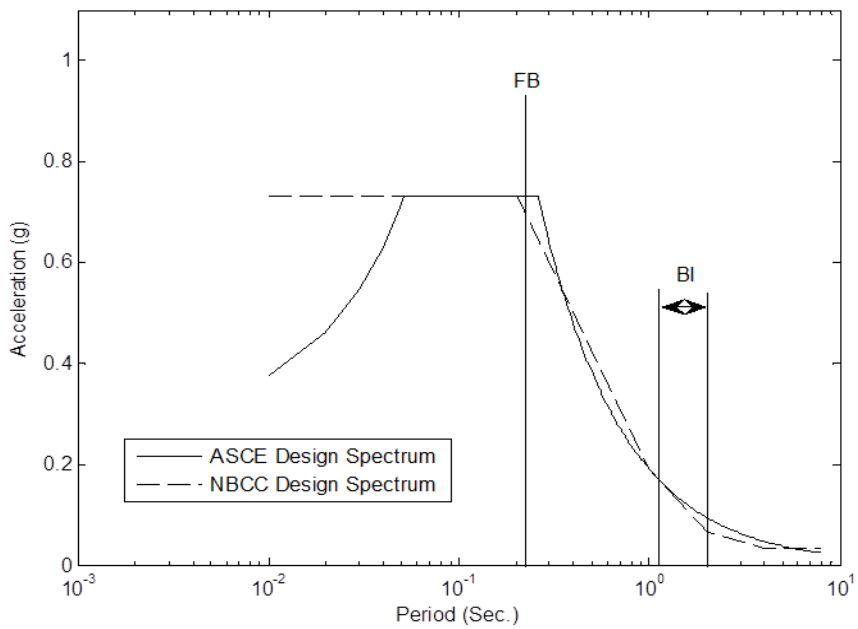

Figure 7.7 ASCE MCE and NBCC DGM design response spectrum for Ottawa, Canada, site class D.

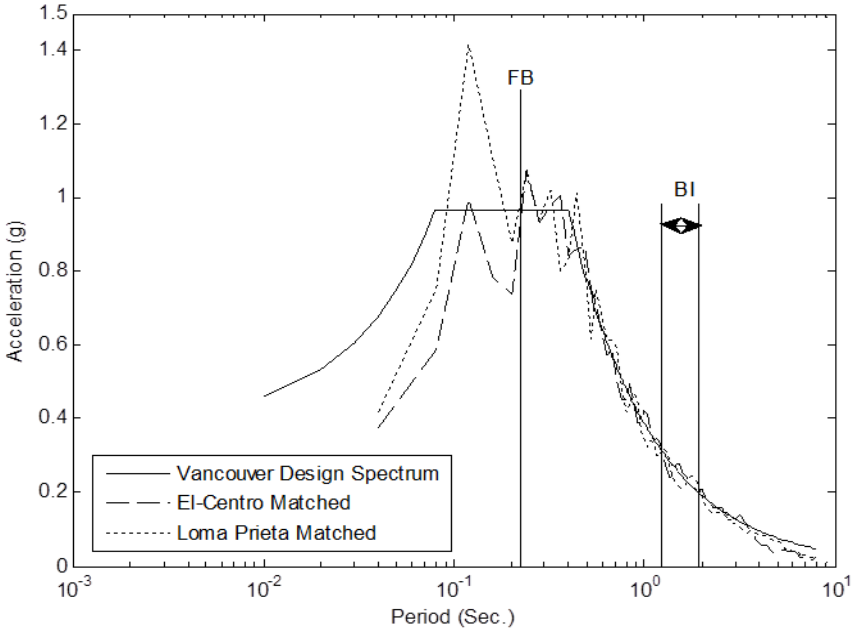

Figure 7.8 MCE design response spectrum for Vancouver with matched El Centro and Loma Prieta records.

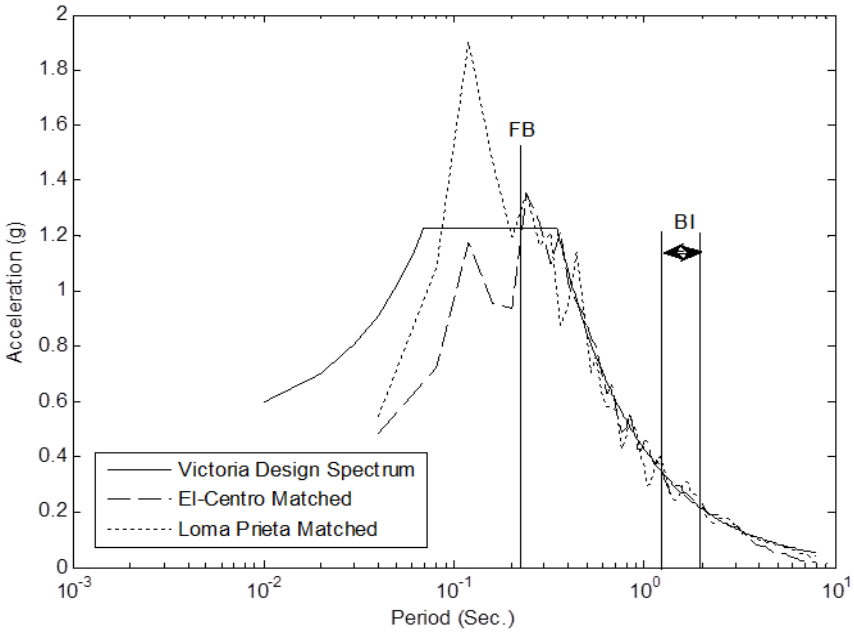

Figure 7.9 MCE design response spectrum for Victoria with matched El Centro and Loma Prieta records.

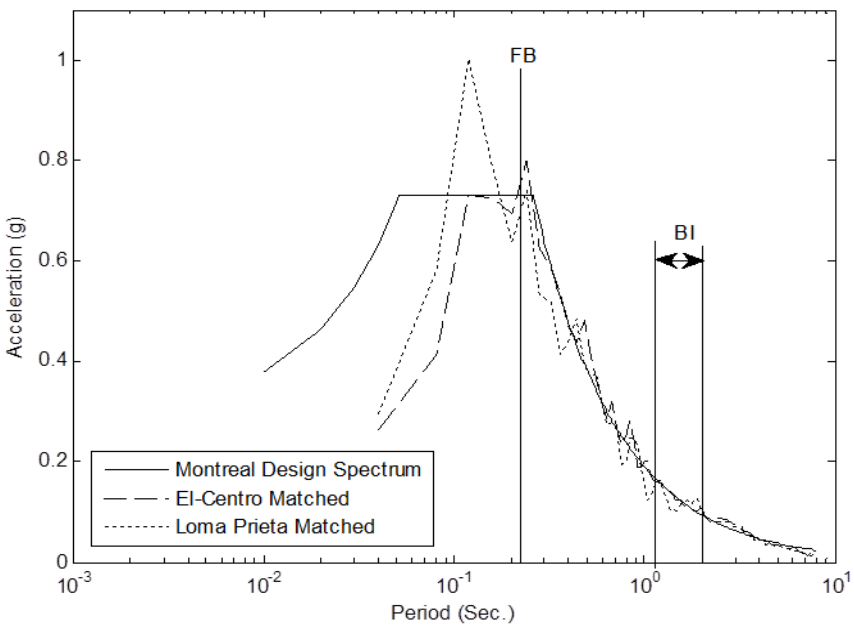

Figure 7.10 MCE design response spectrum for Montreal with matched El Centro and Loma Prieta records.

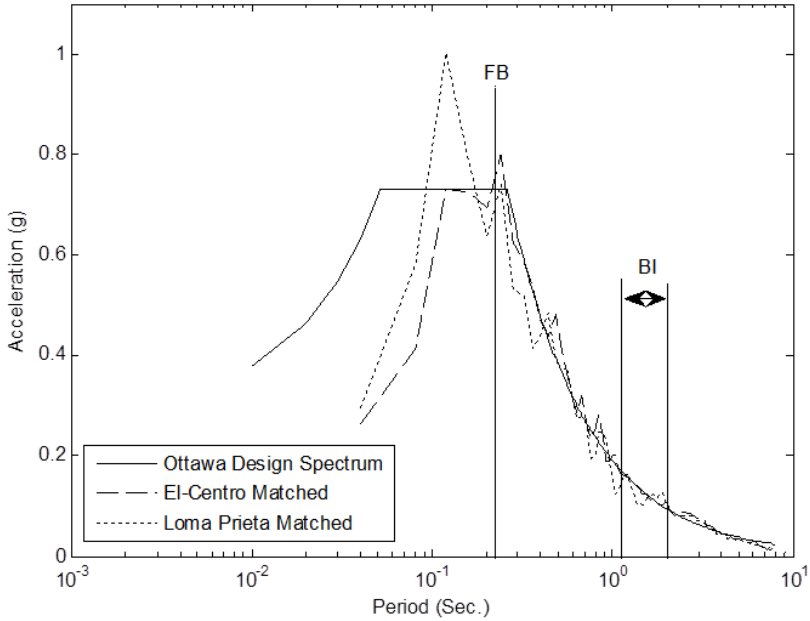

Figure 7.11 MCE design response spectrum for Montreal with matched El Centro and Loma Prieta records.

Chapter 8. Conclusions and Recommendations

The research objective of this thesis was to investigate stable unbonded fibre reinforced elastomeric isolator (SU-FREI) bearings for application in low-rise structures. Experimental testing of individual bearings, as well as shake table testing of an isolated structure was presented. Additionally, two mathematical models were used to simulate the bearing properties in a time history analysis (THA). Finally, a simplified design spectrum approach was presented and used to predict the response of a two-storey structure.

8.1 Bearing Testing

Extensive testing on individual bearings yielded valuable information on their dynamic properties and behaviour over a range of loading cases. The information and trends observed are summarized below.

8.1.1 Vertical Testing

Results obtained from the vertical testing showed that vertical stiffness of the bearings ranged between 14kN/mm and 18kN/mm under a design load of 8kN. An analytical method was used to estimate the vertical stiffness. Good agreement between the two measured and predicted values was found at the design vertical load. Increased discrepancy between the measured and predicted value was found to occur at higher loads.

8.1.2 Lateral Testing

A total of seven bearings were subjected to lateral cyclic testing at the design load of 8kN. Test results showed that the bearings had an effective stiffness that ranged between 85.2N/mm at the lowest amplitude displacement of 25%t_r and 33N/mm at a lateral displacement of 150t_r.

The effective damping was found to be the highest at low amplitudes, reaching a maximum of 11.4%, and lowest at the highest amplitudes, reaching a minimum value of 6.9%. Four of the bearings were cycled up to 250%t_r exceeding the full facial contact value. Full vertical facial contact was observed to have occurred at a displacement of approximately 200%t_r, which is in good agreement with the analytically obtained value of 201%t_r. Upon full vertical facial contact, the effective lateral stiffness of the bearings was found to increase, however the contact phenomenon was found to have little influence on the effective damping value.

An additional three bearings were cycled up to a lateral displacement amplitude of 200%t_r. These three bearings were subsequently tested at a 90° orientation under vertical loads of 2, 4 and 12kN. Test results showed that the vertical load has an effect on lateral stiffness and damping properties. As the vertical load was increased the effective stiffness was found to decrease while the effective damping was found to increase.

The bearings exhibited excellent durability characteristics as only a single bearing specimen experienced any visual damage. The observed damage was a

small delamination between the rubber and fibre, which occurred at 250%t_r lateral displacement amplitude.

8.1.3 Rollout Testing

Three bearings were selected for the rollout testing. All three bearings tested showed visible signs of damage (delamination) at the 400%t_r lateral displacement amplitude tests. Despite the observed damage to the bearings, test results showed that the bearings maintained adequate stability under design load conditions.

8.1.4 Serviceability

The bearings were tested under NBCC wind loading conditions at the corresponding natural frequency of the base isolated structure. The tests were completed under load control to simulate actual wind loading conditions. The test results showed that most of the reduction in both effective lateral stiffness and damping occurred within the first cycle due to the scragging of the elastomer. In all tests, the stiffness of the bearings had reached steady state by the 20th cycle. The damping followed the same trend. It was observed that the lateral stiffness and damping losses were dependent on the amplitude of displacement. The higher lateral displacement amplitude tests performed on the bearings had greater decreases of both stiffness and damping. Overall, the bearings maintained adequate stiffness and damping levels with a reduction of less than 20% of their initial stiffness over the duration of the test.

8.1.5 Fatigue Testing

Fatigue testing was completed on two bearings. The bearings were cycled at 150%t_r for a total 10 cycles. The bearings were cycled under displacement control at a rate of 1.03Hz corresponding to the natural frequency of the base isolated structure. Results showed that the bearings maintained adequate lateral stiffness and damping levels over the duration of testing. As the testing yielded no visible damage to either bearing, it was concluded that the bearings have sufficient durability within the optimal working range of the isolator.

8.2 Bearing Modelling

Two mathematical models were selected to simulate the dynamic response behaviour of the bearings. The first model was a bilinear idealization that is commonly used for the analysis of steel reinforced elastomeric isolators (SREI). The second model was a fifth order polynomial fit of the hysteresis data, known as the backbone curve model. To evaluate the models, each model was subjected to the input motion of the 100%t_r sinusoidal displacement time history. Based on the results of the predicted hysteresis loop both models gave fair predictions with the backbone curve having better agreement to experimentally measured hysteresis loops.

8.3 Shake Table Testing

Shake table testing was completed to observe the dynamics response of the base isolated structure. Free vibration testing revealed that the fixed base structure had a period of approximately 0.102 seconds, while the base isolated period at low displacements was approximately 0.45 seconds. Upon completion of the free vibration testing the three input earthquakes were conducted.

Test results showed that the SU-FREI isolation system was effectively able to reduce the lateral accelerations along the height of the structure mitigating any amplification effects. The constant lateral acceleration along the height of the structure indicated that the structure behaved as a rigid body.

Vertical acceleration data collected from the tests showed that extreme lateral displacements producing full vertical facial contact can have the negative effect of producing larger than expected vertical accelerations. These high vertical accelerations reduce loading on the bearings allowing residual slip to occur more easily. Testing with increased levels of friction between the bearings contact surfaces showed that residual slip can be significantly reduced with little effect on the displacements and forces experienced by the isolated structure.

Comparisons between shake table test results with those of a 5% damped fixed based time history analysis showed that the isolation system was able to mitigate the seismic peak response forces within the structure. For the measurements of in plane lateral roof accelerations and base shear normalized to the weight of the structure, the lowest level of efficiency was 60% while the

highest was 91%. The efficiency of the system increased with increasing amplitude of PGA until the records produced displacement causing full vertical facial contact of the bearings.

8.4 Modelling of a SU-FREI base isolated structure

Using the bilinear and backbone curve mathematical models coupled with a model of the structure and using a time history analysis (THA) the response of the base isolated structure was produced from the earthquake records used in the shake table study.

Both the bilinear and the backbone curve models' ability to predict the dynamic behaviour of the base isolated structure throughout the entire time history of the event was reviewed. The results were also statistically analyzed and it was found that the bilinear model gave more accurate response results. Neither model showed any advantage in terms of processing time as each model took a similar number of iterations to converge to a solution (between 4 and 7). The number of iterations varied and was dependent on the record as well as the amplitude. Overall, the models showed good prediction capabilities and may be used in the preliminary analysis of a SU-FREI base isolated structure.

8.5 Design Spectrum Analysis

A method of analysis that can be used with a code specified design spectrum analysis was presented. Results obtained for the base isolated structure

were compared to the fixed base structure to evaluate the effectiveness of the isolation system. In addition, results from design spectrum analysis were compared to a time history analysis using earthquake records that were matched to the design spectra.

Results of the base isolated to fixed base structure comparison showed that the bearings were highly effective at reducing the response of the structure. The lowest level of efficiency obtained from the results of the data was a 66% reduction for base shear. The highest level of efficiency was in Montreal, where an 86% reduction for spectral acceleration was achieved.

Comparing the results of the design spectrum analysis to those of the time history analysis, the two methods were found to be in good agreement. For the cities of Vancouver and Victoria both the shear force and bearing lateral displacement were slightly overestimated using the design spectrum analysis, implying that the method is conservative. For the cities of Montreal and Ottawa, the displacements were again conservative, but the base shears were lower than the time history analyses predicted values.

8.6 Recommendations for Further Research

The following are areas of suggested future research studies.

- Long-term durability of the bearings under sustained vertical loading and subjected to environmental condition such as extreme temperatures and moisture.

- Bi-directional properties of the bearings studied through bi or three-dimensional shake table testing as well as looking at torsional properties of the bearings.
- Bearing geometry. Testing has been completed on square bearings with different end conditions but further research is required as well as testing of circular and rectangular strip isolators.
- Advanced modelling of the bearings properties, i.e. using additional models such as the Bouc-Wen model.
- An analytical model based on the geometric and material properties of the bearing that can predict the lateral stiffness and damping of the bearing as well as the vertical stiffness.
- Investigation of the response of the bearings in bridge applications under both normal dynamic loading and earthquake loading.

Chapter 9. Bibliography

ASCE. (2005). Minimum Design Loads for Buildings and other Structures. *ASCE/SEI 7-05*. New York: American Society of Civil Engineers.

Cardone, D., Dolce, M., & Rivelli, M. (2009). Evaluation of Reduction Factors for High-Damping Design Response Spectra. *Bulletin ofl Earthquake Engineering*, 273-291.

Chen, W.-F., & Scawthorn, C. (2003). *Earthquake Engineering Handbook.* CRC Press LLC.

Chopra, A. K. (2007). *Dynamics of Structures: Theory and Application to Earthquake Engineering 3rd ed.* New Jersey: Prentice Hall.

de Raaf, M. (2009). Experimental Study of Unbonded Fiber Reinforced Elastomeric Bearings. (Masters Thesis, McMaster University, 2009).

Dorfmann, A., & Ogden, R. (2004). A Constitutive Model for The Mullins Effect with Permanent Set in Particle-Reinforced Rubber. *International Journal of Solids and Structures*, 1855-1878.

Gemme, M.-C. (2009). *Seismic Retrofitting of Deficient Canadian Buildings.* Massachusetts Institute of Technology.

Harris, H. G., & Sabnis, G. M. (1999). *Structural Modeling and Experimental Techniques.* CRC Press.

Hwang, J. S., Wu, J. D., Pan, T. C., & Yang, G. (2002). A Mathematical Hysteretic Model for Elastomeric Isolation Bearings. *Earthquake Engineering and Structural Dynamics, 31*(4), 771-789.

ICC. (2009). International Building Code. International Code Council.

ISO. (2005). Elastomeric seismic-protection isolators. *ISO 22762*. Geneva: International Organization for Standardization.

Kang, B.-S., Kang, G.-J., & Moon, B.-Y. (2003). Hole and Lead Plug Effect on Fiber Reinforced Elastomeric Isolator for Seismic Isolation. *Journal of Materials Processing Technology*, 592-597.

Kelly, J. M. (1997). *Earthquake-Resistant Design with Rubber, 2nd ed.* London: Springer-Verlag Limited.

Kelly, J. M. (1999). Analysis of Fiber-Reinforced Elastomeric Isolators. *Journal of Seismology and Earthquake Engineering, 2*(1), 19-34.

Kelly, J. M., & Konstantinidis, D. (2007). Low-Cost Seismic Isolators for Housing in Highly-Seismic Developing Countries. *10th World Conference on Seismic Isolation, Energy Dissipation and Active Vibrations Control of Structures.* Istanbul, Turkey.

Kelly, J. M., & Takhirov, S. M. (2002). *Analytical and Experimental Study of Fiber-Reinforced Elastomeric Isolators.* PEER Report 2001/11, University of California Berkely.

Koh, C. G., & Kelly, J. M. (1988). A Simple Mechanical Model for Elastomeric Bearings used in Base Isolation. *International Journal of Mechanical Sciences, 30*(12), 933-943.

Love, J. S., Tait, M. J., & Toopchi-Nezhad, H. (2011). A Hybrid Structural Control System Using a Tuned Liquid Damper to Reduce the Wind Induced Motion of a Base Isolated Structure. *Engineering Structures, 33*, 738-746.

Mayes, R. L., & Naeim, F. (2001). Design of Structures with Seismic Isolation, Volume 1. In F. Naeim, *The Seismic Design Handbook* (pp. 723-756). Norwell Massachusetts: Springer.

Moon, B.-M., Kang, G.-J., Kang, B.-S., & Kelly, J. M. (2002). Design and Manufacturing of Fiber Reinforced Elastomeric Isolator for Seismic Isolation. *Journal of Material Processing Technology, 130-131*, 145-150.

Mordini, A., & Strauss, A. (2008). An Innovative Earthquake Isolation System Using Fibre Reinforced Rubber Bearings. *Engineering Structures*, 2739-2751.

Myslimaj, B., Midorikawa, M., Iiba, M., & Ikenaga, M. (2002). Seismic Behavior of a Newly Developed Base Isolation System for Houses. *Journal of Asian Architecture and Building Engineering*, 17-24.

Naderzadeh, A. (2009). Application of Seisimic Base Isolation Technology in Iran. *Menshin*(63), 40-47.

Naiem, F., & Kelly, J. M. (1999). *Design of Seismic Isolated Structures: From Theory to Practice.* New York: John Wiley & Sons, Inc.

NBCC. (2005). National Building Code of Canada. Ottawa: National Research Council of Canada.

NBCC. (2010). National Building Code of Canada. Ottawa: National Research Council of Canada.

Newmark, N. M., & Hall, W. J. (1973). *Seismic Design Criteria for Nuclear Reactor Facilities.* US Department of Commerce. National Bureau of Standards.

Paulay, T., & Priestley, N. M. (1992). *Seismic Design of Reinforced Concrete and Masonry Buildings.* John Wiley & Sons, Inc.

Robert, A. D. (1988). *Natural Rubber Science and Technology.* Oxford: Oxford University Press.

Seismosoft. (2011). SeismoMatch - A Computer Program for Spectrum Matching of Earthquake Records. www.seismosoft.com.

Skinner, I. R., Robinson, W. H., & McVerry, H. G. (1993). *An Introduction to Seismic Isolation.* Chichester, UK: Wiley.

Symans, M. D., Cofer, W. F., & Fridley, K. J. (2002). Base Isolation and Supplemental Damping Systems for Seismic Protection of Wood Structures: Literature Review. *Earthquake Spectra, 18*(3), 549-572.

Tait, M. J., Drysdale, R. G., Toopchi-Nezhad, H., Foster, B. A., & de Raaf, M. G. (2011). *Seismic Isolation of Residential Wood Frame and Low-Rise Masonry Buildings.* Ottawa: Canadian Mortgage and Housing Corporation.

Taylor, A. W., & Igusa, T. (2004). *Primer on Seismic Isolation.* ASCE Publications.

Toopchi-Nezhad, H. (2008). Stable Unbonded Fiber Reinforced Elastomeric Isolators. (Doctoral Thesis, McMaster University, 2008).

Toopchi-Nezhad, H., Drysdale, R. G., & Tait, M. J. (2009c). Parametric Study on the Response of Stable Unbonded-Fiber Reinforced Elastomeric Isolators (SU-FREIs). *Journal of Composite Materials*, 1569-1587.

Toopchi-Nezhad, H., Tait, M. J., & Drysdale, R. G. (2008a). Testing and Modeling of Square Carbon Fiber-Reinforced Elastomeric Seismic Isolators. *Structural Control and Health Monitoring, 15*, 876-900.

Toopchi-Nezhad, H., Tait, M. J., & Drysdale, R. G. (2008b). Lateral Response Evaluation of Fiber-Reinforced Neoprene Seismic Isolators Utilized in an Unbonded Application. *Journal of Structural Engineering, 134*(10), 1627-1637.

Toopchi-Nezhad, H., Tait, M. J., & Drysdale, R. G. (2008c). A Novel Elastomeric Base Isolation System for Seismic Mitigation of Low-Rise Buildings. *The 14th World Conference on Earthquake Engineering.* Beijing, China.

Toopchi-Nezhad, H., Tait, M. J., & Drysdale, R. G. (2009a). Shake Table Study on an Ordinary Low-Rise Building Seismically Isolated with SU-FREIs (Stable Unbonded-Fiber Reinforced Elastomeric Isolators). *Earthquake Engineering and Structural Dynamics*, 1335-1357.

Toopchi-Nezhad, H., Tait, M. J., & Drysdale, R. G. (2009b). Simplified Analysis of a Low-Rise Building Seismically Isolated with Stable Unbonded Fiber Reinforced Elastomeric Isolators. *Canadian Journal of Civil Engineering*, 1182-1194.

Toopchi-Nezhad, H., Tait, M., & Drysdale, R. G. (2007b). Experimental study on carbon fiber-reinforced square seismic isolators. *Ninth Canadian Conference on Earthquake Engineering*, (pp. 26-29). Ottawa, Ontario, Canada.

Tsai, H.-C. (2004). Compression Stiffness of Infinite-Strip Bearings of Laminated Elastic Material Interleaving with Flexible Reinforcements. *International Journal of Solids and Structures*, 6647-6660.

Tsai, H.-C., & Kelly, J. M. (2002). Stiffness Analysis of Fiber-Reinforced Rectangular Seismic Isolators. *Journal of Engineering Mechanics, 128*(4), 462-470.

Tsai, H.-C., & Kelly, J. M. (2004). Buckling Load of Seismic Isolators Affected by Flexibility of Reinforcement. *International Journal of Solids and Structures*, 255-269.